

Accessing Long-lived Nuclear Spin States in Chemically Equivalent Spin Systems:
Theory, Simulation, Experiment and Implication for Hyperpolarization

by

Yesu Feng

Department of Chemistry
Duke University

Date: _____

Approved:

Warren S. Warren, Supervisor

Qiu Wang

Weitao Yang

Michael J. Therien

Dissertation submitted in partial fulfillment of
the requirements for the degree of Doctor
of Philosophy in the Department of
Chemistry in the Graduate School
of Duke University

2014

ABSTRACT

Accessing Long-lived Nuclear Spin States in Chemically Equivalent Spin Systems:

Theory, Simulation, Experiment and Implication for Hyperpolarization

by

Yesu Feng

Department of Chemistry
Duke University

Date: _____

Approved:

Warren S. Warren, Supervisor

Michael J. Therien

Qiu Wang

Weitao Yang

An abstract of a dissertation submitted in partial
fulfillment of the requirements for the degree
of Doctor of Philosophy in the Department of
Chemistry in the Graduate School of
Duke University

2014

Copyright by
Yesu Feng
2014

Abstract

Recent work has shown that hyperpolarized magnetic resonance spectroscopy (HP-MRS) can trace in vivo metabolism of biomolecules and is therefore extremely promising for diagnostic imaging. The most severe challenge this technique faces is the short signal lifetime for hyperpolarization, which is dictated by the spin-lattice (T_1) relaxation. In this thesis we show with theory, simulation and experiment that the long-lived nuclear spin states in chemically equivalent or near equivalent spin systems offer a solution to this problem. Spin polarization that has lifetime much longer than T_1 (up to 70-fold) has been demonstrated with pulse sequence techniques that are compatible with clinical imaging settings. Multiple classes of molecules have been demonstrated to sustain such long-lived hyperpolarization.

Dedication

This thesis is dedicated to my wife and my parents, for their unconditional love and support.

Contents

Abstract	iv
List of Tables	ix
List of Figures	x
Acknowledgements	xv
1. Hyperpolarization and Magnetic Resonance Spectroscopy (MRS)	1
1.1 Dissolution dynamic nuclear hyperpolarization	2
1.2 Hyperpolarized magnetic resonance spectroscopy	7
1.3 Para-hydrogen induced polarization and optical pumping	11
2. Nuclear singlet state and its key properties	17
2.1 Singlet and triplet states	17
2.2 Relaxation properties of the singlet state	19
2.2.1 Bloch-Redfield-Wangsness (BRW) relaxation theory	21
2.2.2 Relaxation property of the singlet and other long-lived states	31
3. Accessing long-lived nuclear spin states	34
3.1 Accessing the long-lived singlet state between inequivalent spins	35
3.2 Accessing the long-lived singlet state between chemically equivalent spins	37
3.3 Accessing the long-lived singlet state between near equivalent spins	39
3.4 Accessing the long-lived states in large symmetric spin system	45
3.4.1 Accessing the long-lived states in an AA'XX' 4-spin system with the MSM sequence	45

3.4.2 Accessing the long-lived states in AA'X _n X _n ' spin systems (n ≥ 2) with the MSM sequence.....	50
3.5 SLIC: An alternative sequence to access the long-lived states.....	56
3.5.1 Using SLIC to access the singlet state between near-equivalent spins.....	56
3.5.2 Using SLIC to access the long-lived states in chemically equivalent spin systems.....	60
3.5.3 Composite and adiabatic SLIC sequence to compensate for field inhomogeneities.....	63
3.6 Polarization transfer from X(¹ H) spins to the long-lived states.....	67
4. Spin dynamics simulation with SPINACH.....	74
4.1 Relaxation lifetime prediction with SPINACH.....	74
4.2 Numerical optimization of adiabatic SLIC pulse using SPINACH.....	79
4.2.1 Resonance conditions of proton-only M2S and SLIC sequences for mDPA.....	79
4.2.2 Optimization of adiabatic shape for SLIC sequence with SPINACH.....	82
5. Experimental demonstration of long-lived nuclear spin states.....	86
5.1 ¹³ C ₂ -diethyl oxalate (DEO).....	86
5.2 ¹³ C ₂ -diphenyl acetylene (DPA).....	92
5.3 ¹³ C ₂ -meta methyl diphenyl acetylene (mDPA).....	95
5.4 ¹⁵ N ₂ -dichloro pyridazine (DCP).....	98
5.5 ¹⁵ N ₂ -azobenzene.....	100
5.6 Molecular tag and structure motif that can be generalized.....	103
6. Conclusion and future direction.....	105
Appendix.....	107

References	108
Biography	118

List of Tables

Table 1 (From Ref ^[12]) Molecules that have been polarized by DNP as well as polarization level achieved at 3.35 T and what biological process(es) that can be probed with each substrate	6
Table 2. Irreducible spherical tensors for spin dipole-dipole interaction (DD) and chemical shielding anisotropy (CSA).....	30
Table 3. 2-level systems in $^{13}\text{C}^{13}\text{C}'^1\text{H}_2^1\text{H}_2'$ 6-spin system of DPA.	55
Table 4. 2-level systems in the AA'QQ' 4-spin system	56
Table 5. SNR comparison between "proton-only" and "carbon-only" pulse sequences assuming thermal polarization and coil-dominated noise	71
Table 6. SNR comparison between "proton-only" and "carbon-only" pulse sequences assuming constant fractional hyperpolarization and body-dominated noise	71
Table 7. Comparison of simulated T_1 relaxation rate and the incoherent relaxation rate for the singlet state across either two ^{13}C or two ^{15}N spins in rigid structures.....	76
Table 8. Summary of measured and simulated T_1 and singlet relaxation time (T_s) at varied field strengths for DPA and mDPA.	79

List of Figures

Figure 1. (From Ref ¹¹) Schematic drawing of the DNP polarizer and its parts. 1, DNP polarizer; 2, vacuum pump; 3, VTI; 4, microwave source; 5, pressure transducer; 6, sample port; 7, microwave container; 8, sample holder; 9, sample container; 10, dissolution wand..... 5

Figure 2. from Ref^[11] (A) ¹³C spectrum of natural abundance (1% ¹³C) urea hyperpolarized by the DNP-NMR method. The concentration of urea was 59.6 mM and the polarization was 20%. (B) Thermal equilibrium ¹³C spectrum of the same sample at the same field strength (9.4T). This spectrum was acquired under Ernst-Angle condition with full ¹H-decoupling. The signal was averaged during 65 h (232,128 scans)..... 6

Figure 3. (From Ref ¹⁴) (Left) Flux of [1-¹³C]pyruvate to [1-¹³C]lactate is catalyzed by lactate dehydrogenase (LDH). Dynamic ¹³C spectra are acquired from a patient with biopsy-proven prostate tumor. Lactate ¹³C peak is significant in the cancer tissue but almost undetectable in normal tissue. (Middle) Axial T₂-weighted image shows a unilateral region of reduced signal intensity (red arrows). (Right) ¹³C Chemical shift image overlaid on the same T₂-weighted image, showing voxels with elevated levels of hyperpolarized [1-¹³C]lactate/[1-¹³C]pyruvate (highlighted in pink) on both left and right side of the prostate. The location of the colored region has a [1-¹³C]lactate/[1-¹³C]pyruvate ratio greater than or equal to 0.6. 9

Figure 4. (From Ref ¹⁷) Population models for a 2-spin system of AB character. (a) Standard NMR system (b) PASADENA (c) ALTADENA 13

Figure 5. Energy levels for coupled two spin system. (a) Zeeman basis for the coupled two spin system, which is a good approximation to eigenstates of the spin system Hamiltonian when the two spins are weakly-coupled. (b) Singlet-Triplet basis for the coupled two spin system with $S = (\alpha\beta + \beta\alpha) / \sqrt{2}$, $T_{+1} = \alpha\alpha$, $T_0 = (\alpha\beta + \beta\alpha) / \sqrt{2}$, $T_{-1} = \beta\beta$, is the eigenbasis set for the system Hamiltonian when the two spins are magnetically *equivalent*..... 19

Figure 6. Per-deuterated 2,3-¹³C₂-diacetyl. The dehydrated form (left) is stable in acetone and is symmetric but the two ¹³C spins are coupled differently ($J_{CD} \neq J_{CD'}$) to the same deuterium, therefore they are *chemically equivalent* but not *magnetically equivalent*. The hydrated form (right) is asymmetric and therefore the two ¹³C spins are *inequivalent*..... 38

Figure 7. The M2S-S2M sequence. M2S (“magnetization to singlet”) converts bulk magnetization into the singlet state population. The sequence is composed of two blocks of precisely-spaced multiple echo pulse train and two 90° pulses (one as the excitation pulse the other separates the two blocks of 180° s). Phase of the pulses are specified as subscripts. The first multiple echo sequence contains n 180° s, n is given by equation (41) and the second contains $n/2$ 180° s. Between M2S and S2M is the waiting time for relaxation (τ_r). For experiments conducted at thermal equilibrium, filters are necessary to suppress residual thermal signals that relax on time scale of T_1 . For example, a z-gradient is implemented immediately after the M2S to suppress spurious coherences⁵⁷. Repetitions of 90° -Gz are also desirable to remove the fast-decaying component of the final signal. n_f denotes the number of repetitions. Then S2M (“singlet to magnetization”) converts the singlet state population back to bulk magnetization for detection. S2M is the exact chronological reverse of M2S. 39

Figure 8. Analogy between (a) population inversion in a single spin $\frac{1}{2}$ two-level system and (b) population inversion in the S- T_0 two-level system. (a) Irradiation of single spin $\frac{1}{2}$ by a continuous square wave pulse with constant field strength B_1 , which is much smaller than the main field B_0 , shows that an arbitrarily small B_1 field can flip spins if the field is modulated. As discussed in text, conversion between the S and T_0 states works in exactly this same way, with the “square wave” replaced by a broadband pi pulses on both spins (b) Population interconversion between S (black) and T_0 (red) states in a near equivalent 2-spin system. The following parameters were assumed: $J = 181.8\text{Hz}$ and $\Delta\omega = 18.1\text{Hz}$. An inter pulse delay of 2.74 ms is calculated according to (40). 43

Figure 9. The SLIC sequence. A hard 90° pulse with y-phase, followed by continuous wave (CW) irradiation with x-phase and specified amplitude of ω_1 to match the in-pair J-coupling creating population of the singlet state. For a constant amplitude CW irradiation as introduced in Ref[67], an irradiation period of $\tau_{SL} = 1/(\sqrt{2}\Delta\gamma)$ creates the maximum singlet state population. The population is then readout after a storage time, τ_r , by another period (τ_{SL}) of CW irradiation with the appropriate amplitude. The phase of the second CW-pulse is not critical but has been implemented with the same phase for simplicity. For singlet state lifetime measurement at thermal equilibrium, we implemented gradient- 90° x combinations as filter to suppress residual thermal signal decaying by T_1 , which was not used in the original paper (ref[65]). n_f (up to 15) denotes the number of 90° x-Gz repetition unit it requires to completely destroy the thermal contribution..... 57

Figure 10. Spin systems discussed in chapters 3 and 4. (a) 2,3-¹³C₂-diacetylene (DIAC) contains a CC’HH’ 4-spin system ($D_{\infty h}$ point group). (b) 3,6-dichloro-¹⁵N₂-pyridazine

(DCP) contains a $^{15}\text{N}^{15}\text{N}'\text{H}\text{H}'$ 4-spin system (C_{2v} point group). (c) $^{13}\text{C}_2$ -diphenyl acetylene (DPA) contains a $^{13}\text{C}^{13}\text{C}'\text{H}_2\text{H}_2'$ 6-spin system (D_{2h} pointgroup), the remaining protons are not considered for they have minimum couplings to the central $^{13}\text{C}_2$ spin pair. (d) $^{13}\text{C}_2$ -meta methyl diphenyl acetylene (mDPA) also has a $^{13}\text{C}^{13}\text{C}'\text{H}_2\text{H}_2'$ 6-spin system, however, a significant chemical shift difference between the two ^{13}C spins ($\Delta\omega = 0.56$ ppm) breaks the symmetry of the spin system. 62

Figure 11. (left) Simulated singlet state population after the first cw irradiation in SLIC with varied duration (τ_{SL}). $^{13}\text{C}_2$ -singlet state population in DPA (6-spin, $J_{\text{CC}} = 181.8$ Hz and $\Delta\text{JCH} = 5.82$ Hz), in a pseudo 4-spin and a pseudo 8-spin system with the same J-couplings are simulated. The singlet state population in the 4-spin system has a single-frequency sinusoidal dependence on τ_{SL} while both 6-spin and 8-spin systems have multi-frequency sinusoidal dependence on τ_{SL} , indicated by the “flattened” profile. (right) Experimental evaluation of SLIC signal measured with DPA. The first τ_{SL} varies but the second is fixed. The first period of oscillation has flattened profile that agrees with the simulation. Field inhomogeneities and T_2 relaxation quickly damp out the oscillation in experiment while these factors are not included in the simulation. 63

Figure 12. From Ref. [59], simulations of several SLIC pulse shapes examining their B_1 amplitude sensitivity and frequency offset sensitivity. (Top row a-c) shows the behavior for the simple spin-lock with 5Hz bandwidth in the B_1 amplitude and 62 Hz bandwidth in the RF-offset. The traditional composite pulse (second row d-f) completely fails to produce the singlet state whereas singlet composite pulse (third row g-i) improves both the B_1 -amplitude resonance condition bandwidth (10Hz) as well as the RF-offset resonance bandwidth (84Hz),. Further improvement is provided by the singlet adiabatic pulse (bottom row j-l), yielding a B_1 -resonance bandwidth of 30Hz and RF-offset bandwidth of 140Hz (For details of the simulations see next chapter). 67

Figure 13. (a) Population difference between the $^{13}\text{C}_2$ -S and T_0 states in mDPA after the M2S(^1H) sequence with various number (N) of 180° pulses and inter-pulse delay (τ). The vertical axis is the number (N/2) of 180° pulses in the second multiple echo sequence block in M2S. (b) Population difference between the $^{13}\text{C}_2$ -S and T_0 states in mDPA after the first half of the SLIC(^1H) sequence with different irradiation power (in units of Hz) and duration (τ). 82

Figure 14. Adiabatic waveforms for the SLIC sequence with mDPA. (a) Shapes of the adiabatic pulses. The initial shape (dashed blue) is the adiabatic pulse designed for DPA (section 3.5.3) but with shortened duration (70ms). The optimized shape (red) has the same duration but high frequency modulations based on the initial shape. (b)

Performance of the two shapes against RF off-resonance effect; moderate improvement is provided by the shape generated from the GRAPE algorithm. 84

Figure 15. Molecules discussed in chapter 5 that can sustain a long-lived nuclear spin state. (a) $^{13}\text{C}_2$ -diethyl oxalate (DEO). (b) $^{13}\text{C}_2$ -3-(4-(phenylethynyl)phenyl)propanoic acid. (c) $^{15}\text{N}_2$ -azobenzene (trans) (d) $^{15}\text{N}_2$ -azobenzene (cis). (e) $^{15}\text{N}_2$ -photo-methione. (f) $^{13}\text{C}_2$ -D₂-fumarate. 87

Figure 16. Single scan ^{13}C spectra of DEO from experiments (a,c) and simulations (b,d) after the CPMG part of the M2S sequence. (a-b) perturbation in ^{13}C spectra after the CPMG sequence with the same inter pulse delay 4.92 ms and various number of echo pulses (n1); maximum conversion in the singlet-triplet subspace occurs after 45 echo pulses, middle row of (b), which is the spectrum after a perfect conversion from carbon triplet to singlet. (c-d) perturbation in ^{13}C spectra after the CPMG sequence with 45 echo pulses and various inter pulse delays ($\tau = 2, 4.92$ or 16 ms). Minimum perturbation can be observed with 2 or 16 ms inter pulse delay..... 90

Figure 17. (a) DEO ^{13}C -singlet state signals from the MSM sequence at thermal condition (b) natural logarithm of DNP-hyperpolarized DEO ^{13}C signal from the MSM sequence, all decay as a function of the waiting time τ_r between M2S and S2M sequence. Signal intensity is normalized against the full thermal polarized magnetization in both cases and all estimations include a 95% confidence interval. In (a), T_1 of ^{13}C in DEO is measured to be 22.2 ± 0.6 s in a Bruker 360 MHz magnet dissolved with DMSO-d₆. The singlet signal decays with a lifetime T_s of 50.6 ± 2.1 s. (b) Hyperpolarized singlet signal is acquired in a 7T (300MHz) Bruker MRI scanner and plotted on a semi-log scale. A T_s of 41.4 ± 3.2 s is obtained compared with a T_1 of 23 ± 0.6 s..... 91

Figure 18. $^{13}\text{C}_2$ -singlet state relaxation lifetime (T_s) measured at 8.45 T (a) and 16.44 T (b-c). (a) A T_s of 288.4 ± 3.7 s is observed (black). This is compared to a singlet state relaxation measurement where the M2S part of the MSM sequence has been applied at the ^1H resonance frequency instead of the ^{13}C resonance frequency (red) resulting in an enhancement of the acquired signal close to 4. For the singlet state relaxation using the ^1H polarization a T_s of 282.7 ± 3.8 s is observed. The small discrepancy in the relaxation times is likely due to subtle differences in the contributions of thermal signal in the two measurements. (b) M2S applied on the ^{13}C channel and S2M applied on the ^1H channel. A T_s of 223 ± 9 s is observed. (c) M2S and S2M applied on the ^1H channel such that the ^{13}C channel remains entirely unused. A T_s of 261 ± 7 s is observed. 94

Figure 19. Experimental evaluation of SLIC signal strength against B_1 field inhomogeneity. B_1 has been varied from 140 to 220 Hz. The composite pulse provides a

54% signal enhancement compared with simple cw irradiation whereas the adiabatic pulse gives a signal enhancement of 163% (The solid lines simply connect the points for better visualization). 95

Figure 20. (a) The singlet state lifetime (T_s) measurements from a MSM (^{13}C only, black, $T_s = 146.8 \pm 3.0$ s) and a M2S(^1H)-S2M(^{13}C) (polarization transfer from proton, red, $T_s = 145.5 \pm 2.2$ s), in both measurements, the maximum signal is normalized against a ^{13}C 90° -acquire. (b) The singlet state lifetime (T_s) measurements from a complete SLIC sequence (^{13}C only, black, $T_s = 130.9 \pm 2.4$ s), a complete SLIC (^1H to ^{13}C , polarization transfer from proton, red, $T_s = 128.2 \pm 1.2$ s) and a SLIC sequence with adiabatic proton pulse for polarization transfer (magenta, $T_s = 126.3 \pm 1.7$ s). In all measurements, the maximum signal is normalized against a ^{13}C 90° -acquire. (c) The singlet state lifetime measurement on proton through a proton-only adiabatic SLIC sequence. $T_s = 108.1 \pm 4.0$ s. 98

Figure 21. The singlet state relaxation (T_s) measurements on DCP through the MSM sequence. To obtain this data the MSM sequence is run with variable delay τ_r between M2S and S2M giving the Time-axis. The fitted T_s values are obtained from the MSM (^1H to ^{15}N , red curve) sequence. Relaxation decays from MSM (^{15}N only) sequences are shown but measurement of T_s is not taken due to large uncertainties of the fitting. (a) The MSM sequence accesses the SS- T_0T_0 2-level system using an inter-pulse delay τ of 33.3 ms, $T_s = 36.7 \pm 1.8$ s while T_1 is measured to be 15.2 s. (b) The MSM sequence accesses the ST $_0$ - T_0S 2-level system with an inter-pulse delay τ of 15.1 ms, $T_s = 37.9 \pm 1.1$ s. 100

Figure 22. Long-lived signal of $^{15}\text{N}_2$ -azobenzene (trans) measured with the SLIC sequence. Both measurements are taken at 8.45 T. (a) SLIC (^{15}N -only, black) and (^1H preparation ^{15}N detection, red). The measured relaxation lifetimes are $T_s = 54 \pm 2$ s (^{15}N -only) and $T_s = 61 \pm 1$ s (^1H preparation ^{15}N detection). T_1 of ^{15}N is 6 s at the same field strength. Proton polarization transfer results in an 8-fold signal enhancement. (b) SLIC (^1H -only), the measured lifetime $T_s = 58 \pm 2$ s and T_1 of proton is 3 s. 102

Acknowledgements

I would like to first thank my advisor and mentor, Dr Warren Warren for his guidance, encouragement and scientific intuition, which make my Ph.D career thrilling and fruitful. I am also fully indebted to people in the Warren Lab for their help and collaboration. Specifically, I would like to acknowledge the tremendous contributions to this project from Dr Thomas Theis, Kevin Claytor, Ryan Davis and Tung-Lin Wu. I am also obliged to people who brought me up to speed: Prof. Rosa Tamara Branca, Dr Morris Chen, Dr Elizabeth Jenista, Dr Ashley Stokes and Rachel Simmons. I would like to also extend my gratitude to Duke NMR center, Dr Anthony Ribeiro, Don Mika and Dr Ron Venters for their generous help and support on the hardware. This interdisciplinary project cannot advance without fruitful collaborations. I would like to thank Dr Xiaofei Liang and Dr David Gooden from Duke small molecule synthesis facility and Prof. Qiu Wang and Gerardo Ortiz from department of chemistry here at Duke. It is my sincere hope that this project will turn out to be very rewarding for all these people.

1. Hyperpolarization and Magnetic Resonance Spectroscopy (MRS)

Since its first implementation as a medical imaging tool in the 1970s, magnetic resonance imaging has become one of the most prominent imaging modalities for diagnosis and treatment; it also has a wide range of applications in biological and materials science. MR has a unique advantage over other molecular imaging modalities, in that it produces a “molecular fingerprint”, so MR has the potential to produce not only information about spatial distribution of tracer molecules but also information of their metabolic products.

Yet, even today, virtually all routine clinical MR scanners mostly image water. The reason is sensitivity: the energy generated by interactions between even very large magnetic fields and nuclei spins is trivial compared with thermal energy of spins, so the Boltzmann distribution implies the fractional magnetization is small¹⁻⁴. Water, with its significant *in vivo* concentration and the large gyro-magnetic ratio (γ) of the proton spin, is thus often the only accessible target. As a result, MRI provides mostly structural information, especially for soft-tissue imaging (where water is abundant) while its functional imaging capability is limited. This stands in contrast to methods such as Positron Emission Tomography (PET), where radioactive tracers can be tracked *in vivo* at extremely low concentrations⁵.

The key to unlock this potential is to significantly enhance signal intensity. Traditional efforts to address this challenge include increasing the field strength or number of accumulated scans. Translation of these approaches to clinical imaging is difficult. Recently, “hyperpolarization” techniques have been developed which can dramatically boost MR signal by more than four orders of magnitude. Here, we provide brief introduction to hyperpolarization methods with a focus on dynamic nuclear hyperpolarization (DNP), which is the most versatile technique to increase MR signal of small molecules. It is followed by a brief review of recent metabolic MR studies using hyperpolarized ^{13}C contrast agents, especially hyperpolarized ^{13}C -pyruvate for human prostate cancer detection.

1.1 Dissolution dynamic nuclear hyperpolarization

Dynamic nuclear polarization (DNP) refers to a class of techniques that transfer much higher polarization from an unpaired electron (usually in a different molecule) to the nuclei of interest. The motivation is that the large gyromagnetic ratio of the electron (about 660 times higher than ^1H) implies a proportionally larger fractional magnetization; in addition, electron spins relax back to equilibrium more rapidly than nuclear spins do, so it is often possible to polarize many nuclei with one electron. DNP was first demonstrated for nuclei in metals⁶⁻⁷ and was soon applied also to diamagnetic solids and paramagnetic molecules in solution⁸. Traditionally the dominant effect that drives this polarization transfer especially in solid-state, is called “solid effect”, although other

mechanisms also contribute such as thermal mixing and cross-effect⁹ (check ref⁹ for a thorough review on microscopic mechanisms). Operationally, this method can be described as following: a diamagnetic insulator that contains a small concentration of paramagnetic impurities (e.g., organic free radicals) is irradiated by continuous microwave source around the magnetic resonance frequency of electron (ESR frequency, ω_e), more specifically, at the frequency difference or sum ($\omega_e \pm \omega_n$, $\omega_e \gg \omega_n$) between the electron and the target nuclei (ω_n). This leads to dramatically enhanced nuclear polarization, orders of magnitude larger than its thermal polarization and can be comparable to electron polarization. Critical conditions for this technique to succeed often include high magnetic field (e.g., ~ 3 T), which allow for close to unity electron polarization, extremely short electron relaxation time (e.g., \sim ms) and very long nuclear relaxation time (e.g., $\sim 10^3$ s). Accordingly, polarization transfer can occur efficiently without significant loss due to spin-lattice (T_1) relaxation on the nuclei. Since its discovery, DNP had been successfully applied to improve the sensitivity of solid-state NMR¹⁰ to more than 100 fold, yet the spectral resolution of solid-state NMR is much lower than that of liquid-state NMR.

A major breakthrough occurred in 2003, when for the first time the so-called dissolution DNP was demonstrated¹¹. A schematic drawing¹¹ of the first dissolution DNP polarizer and its parts are shown in (Figure 1). Major components of the DNP system are the narrow-bore high field magnet which is charged to 3.35 T and the

cryostat. The variable temperature insert (VTI, part 3 in Figure 1) cools the temperature down to ~ 1.2 K by controlling the flow of helium from the liquid-helium dewar and it is in thermal contact with the outer liquid-nitrogen dewar. The DNP insert is placed in the cold bore of the magnet. It is composed of a fiberglass tube that can guide the sample when it is inserted to the center of the magnet and ends in a cylindrical metal container (38 mm diameter, 50 mm height), which is used to confine the microwaves. Inside the container, there is a pair of saddle coils to monitor the nuclei polarization build-up. Remaining parts include a pump that is connected to the VTI and can sustain a vapor pressure of ~ 0.8 mbar, which is used as a measure of temperature, a microwave generator, a sample holder made of Teflon tube, a sample container and the dissolution wand through which boiling water is injected into the sample container and the dissolved sample is displaced to a receiving container.

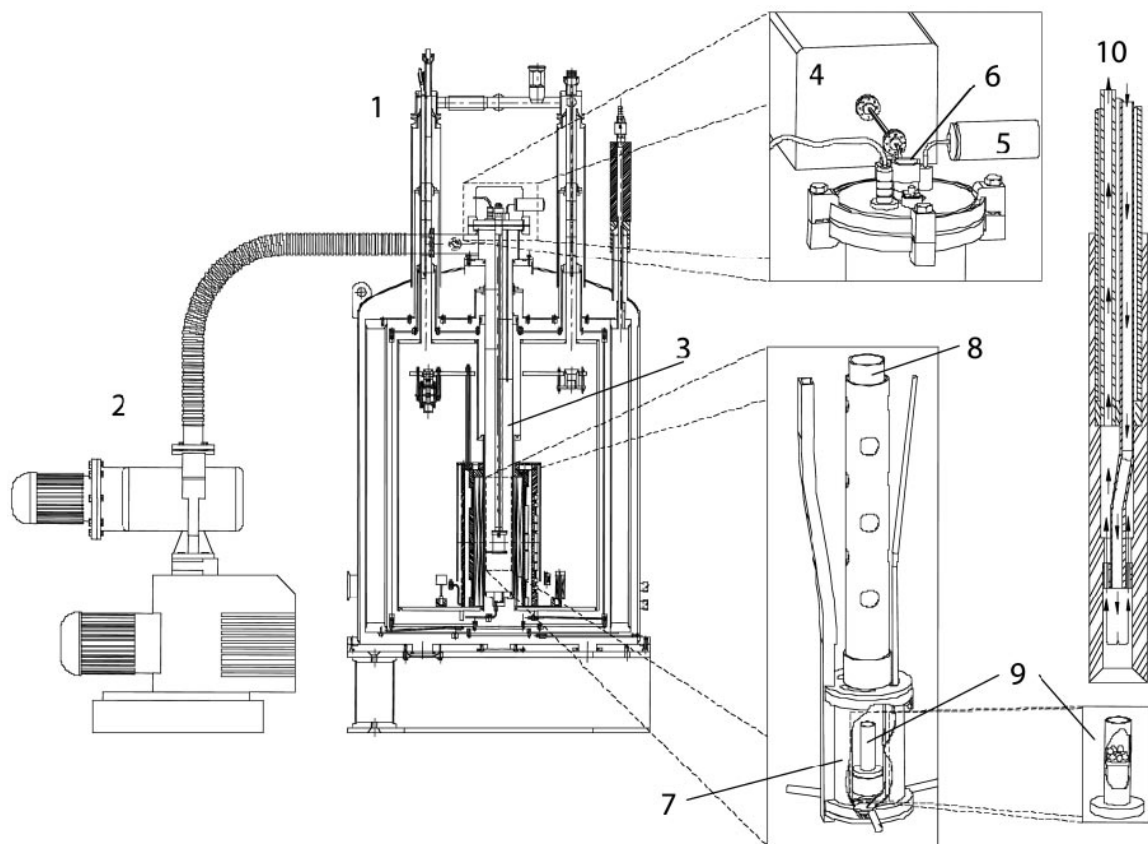


Figure 1. (From Ref ¹¹) Schematic drawing of the DNP polarizer and its parts. 1, DNP polarizer; 2, vacuum pump; 3, VTI; 4, microwave source; 5, pressure transducer; 6, sample port; 7, microwave container; 8, sample holder; 9, sample container; 10, dissolution wand.

By rapid dissolution into boiling water, molecules that are hyperpolarized as frozen solid can be brought into aqueous phase at room temperature within seconds after the hyperpolarization process. The initial demonstration was with aqueous solution of urea at a concentration of 59.6 mM. A single scan ¹³C 90°-acquire spectrum of the hyperpolarized sample has an SNR of 4592 while the same sample at thermal equilibrium requires 65 h of average to obtain an SNR of 7 (Figure 2).

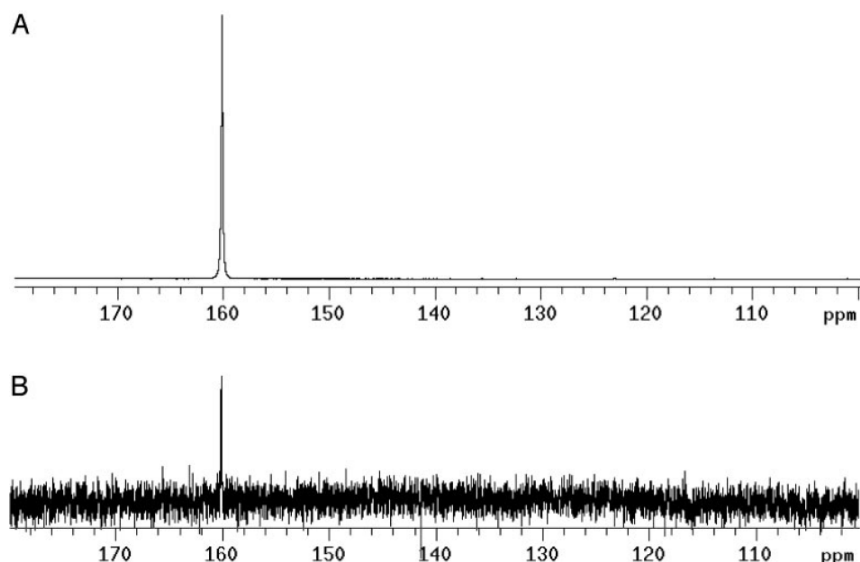


Figure 2. from Ref^[1] (A) ¹³C spectrum of natural abundance (1% ¹³C) urea hyperpolarized by the DNP-NMR method. The concentration of urea was 59.6 mM and the polarization was 20%. (B) Thermal equilibrium ¹³C spectrum of the same sample at the same field strength (9.4T). This spectrum was acquired under Ernst-Angle condition with full ¹H-decoupling. The signal was averaged during 65 h (232,128 scans).

Since then, multiple compounds have been hyperpolarized (Table 1) and the typical formulation contains concentrated sample compound of a few grams (neat if possible, otherwise mix the compound with glass-forming solvent such as glycerol and DMSO in a ratio of e.g., 1:1), 10~100 mg of radicals and the final concentration of the compound should reach at least a few molar.

Table 1 (From Ref^[12])Molecules that have been polarized by DNP as well as polarization level achieved at 3.35 T and what biological process(es) that can be probed with each substrate

Molecule	Reported polarization level	What it can probe
[1- ¹³ C]Pyruvate	Up to 40% at 3.35 T (Up to	LDH; NADH/NAD ⁺ ; Glycolysis

	64% at 4.64 T)	Treatment response; PDH; intracellular pH; ALT
[1- ¹³ C]Ethyl pyruvate	28-35%	LDH; Brain metabolism
[1- ¹³ C]Lactate	7%	LDH
¹³ C-Bicarbonate	15%	pH; Carbonic anhydrase activity
[1,4- ¹³ C ₂]Fumarate	26-35%	Fumarase; Necrosis
[2- ¹³ C]Fructose	12%	GLUT5; Hexokinase; Glycolysis; PPP
[1- ¹³ C]Ketoisocaproate	32% (2-fold higher at 4.64 T)	BCAT; Glutamate
[5- ¹³ C]Glutamine	5%	Glutaminase
[1- ¹³ C]Glutamate	28%	ALT; α -Ketoglutarate
[1- ¹³ C]Urea	37%	Perfusion

1.2 Hyperpolarized magnetic resonance spectroscopy

The most exciting application of dissolution DNP is to acquire *in vivo* metabolic imaging or so-called hyperpolarized magnetic resonance spectroscopy (HP-MRS). Multiple biological-relevant (Table 1, mostly endogenous, e.g., molecules in the tricarboxylic acid cycle (TCA)) molecules have been hyperpolarized and many have been injected into preclinical mouse model as well as human patients to study metabolic

phenotype of different diseases¹²⁻¹⁴. Most of these contrast agents are ¹³C-enriched due to the fact that carbon is ubiquitous in biomolecules but endogenous ¹³C is scarce (1% natural abundance). Therefore, a “hotspot” ¹³C image can be generated with minimum background. Moreover, ¹³C chemical shift changes induced by metabolic transformation can also be encoded into the image (known as chemical shift imaging, CSI) and thus inform on the metabolism of these contrast agents. The fact that spatial resolution of these hyperpolarized ¹³C images is very low can be compensated for by overlaying it with a proton image that provides detailed structural information; similar to the idea of PET/CT combination except this is accomplished with a single imaging modality and real-time *in vivo* metabolic transformations can be tracked which is unattainable so far by any other modalities including PET/CT imaging.

An excellent example of *in vivo* HP-MRS is to detect human prostate cancer with hyperpolarized [1-¹³C]-pyruvate¹⁴. Intravenously injected [1-¹³C]-Pyruvate is primarily metabolized into [1-¹³C]-alanine, [1-¹³C]-lactate and ¹³CO₂ in human body. Among these metabolites, [1-¹³C]-lactate that results from the reaction catalyzed by the enzyme lactate dehydrogenase (LDH) is of particular diagnostic interest. Due to the Warburg effect¹⁵, also known as aerobic glycolysis¹⁶ in tumor cells, the transformation from pyruvate to lactate is highly up-regulated, leading to significantly higher concentration of [1-¹³C]-lactate in the tumor region compared with normal tissue after [1-¹³C]-pyruvate injection (Figure 3). Because [1-¹³C]-pyruvate and [1-¹³C]-lactate have distinct chemical shifts, they

can be differentiated in the CSI image and their relative amounts as well as their transformation dynamics can also be quantified. This single metabolic pathway has become the most widely explored HP-MRS method so far. A particularly successful application is in studying prostate cancer due to the fact that ^{18}F FDG-PET does not give positive signals in many tumors such as prostate tumor that consume alternative substrates other than glucose to support their growth and survival. One example image from a patient with biopsy-proven bilateral prostate tumors is shown in Figure 3. Conventional MRI such as T₂-weighted showed a unilateral region (left side of the prostate) of reduced signal intensity but showed no abnormality on the right side of the prostate. However, ^{13}C metabolic image showed regions of significantly elevated [1- ^{13}C]-lactate level ($[\text{1-}^{13}\text{C}]\text{-lactate}/[\text{1-}^{13}\text{C}]\text{-pyruvate} \geq 0.6$) on both sides of the prostate.

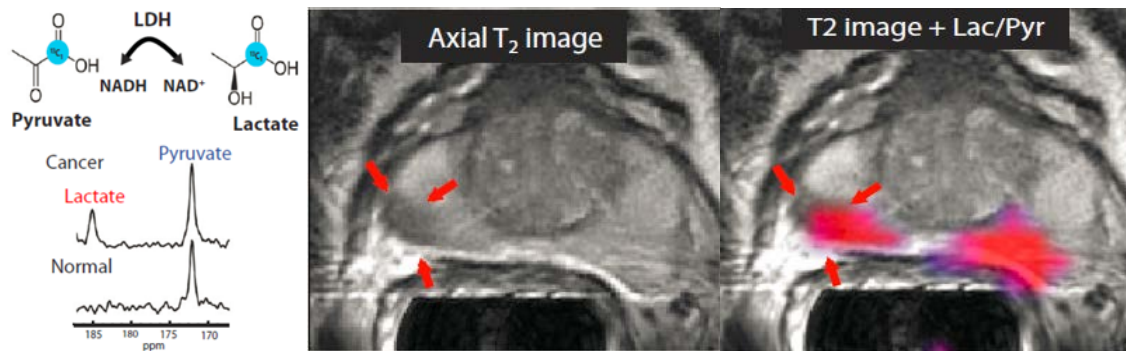


Figure 3. (From Ref ¹⁴) (Left) Flux of [1- ^{13}C]pyruvate to [1- ^{13}C]lactate is catalyzed by lactate dehydrogenase (LDH). Dynamic ^{13}C spectra are acquired from a patient with biopsy-proven prostate tumor. Lactate ^{13}C peak is significant in the cancer tissue but almost undetectable in normal tissue. (Middle) Axial T₂-weighted image shows a unilateral region of reduced signal intensity (red arrows). (Right) ^{13}C Chemical shift image overlaid on the same T₂-weighted image, showing voxels with elevated levels of hyperpolarized [1- ^{13}C]lactate/[1- ^{13}C]pyruvate (highlighted in pink) on both left and right

side of the prostate. The location of the colored region has a $[1-^{13}\text{C}]\text{lactate}/[1-^{13}\text{C}]\text{pyruvate}$ ratio greater than or equal to 0.6.

To date, hyperpolarized $[1-^{13}\text{C}]\text{-pyruvate}$ has been applied to monitor tumor response to chemotherapy treatment as well as anticancer drugs that target oncogenic signaling; it has also been applied to assess prostate cancer progression. Moreover, hyperpolarized $[1-^{13}\text{C}]\text{-pyruvate}$ has been shown useful in studying other human diseases such as diabetes and ischaemic heart disease; the other metabolites from $[1-^{13}\text{C}]\text{-pyruvate}$, i.e., $[1-^{13}\text{C}]\text{-alanine}$ and $^{13}\text{CO}_2$ are important especially for the last example¹³. Published hyperpolarized molecules and their application are summarized in Table 1.

Unfortunately, metabolic processes that can be probed by these hyperpolarized agents are still largely confined to only a few. For instance, it's very difficult to use $[1-^{13}\text{C}]\text{-pyruvate}$ to probe any abnormal metabolism associated with brain diseases that do not cause disrupted blood-brain barrier (BBB) such as infiltrating gliomas, Alzheimer disease or non-enhancing multiple sclerosis¹³. The challenge is that the lifetime of polarization is too short (tens of seconds up to one minute) to allow the molecule to penetrate through the BBB; consequently the hyperpolarized signal decays away before any metabolism inside the brain can be detected. This is the most fundamental limitation of hyperpolarization techniques: relaxation process (dictated by T_1 of the nuclei, e.g., up to a minute for ^{13}C and seconds for ^1H) take hyperpolarized signal back to the thermal polarization level and renders it undetectable *in vivo*. This is dramatically different from conventional MRI where multiple averages can be used. This is also the reason why HP-

MRS on ^1H looks futile. To mitigate this effect, one has no option but to either enhance polarization level or to increase injection dosage, which can significantly perturb *in vivo* physiology and raises safety concerns.

Without solving this challenge, HP-MRS can only use a few molecules that contain a comparatively long-lived ^{13}C (most likely carbonyl carbon) and even with these molecules, it can only detect limited metabolic pathways. The main topic of this thesis is to tackle this challenge; it may look formidable since relaxation is driven by irreversible mechanisms that operate at multiples of nuclear spin Larmor frequency (hundreds of MHz) whereas modern MR pulse sequence technique can only intervene with interactions that operate on time scales that's longer than the RF pulse length (μs to ms). It turns out the solution lies in the so-called "symmetry-protected" spin states that naturally exist. The remaining question is how to use them, but before diving into this main topic, I will first review the most well-known example of "symmetry-protected" spin state in NMR, namely parahydrogen and briefly discuss its application as an alternative source for hyperpolarization. A third hyperpolarization method, i.e., optical pumping will also be briefly covered at the end of the next section.

1.3 Para-hydrogen induced polarization and optical pumping

Para-hydrogen and ortho-hydrogen are the two isomers of hydrogen. They are different in nuclear spin configuration and as a result of overall symmetry requirement, also different in their rotation states¹⁷. The two protons in para-hydrogen form a

“singlet”, meaning their total nuclear spin is zero whereas the two protons in ortho-hydrogen form a “triplet”, meaning their total nuclear spin is one. Unlike ortho-hydrogen, which splits into three spin energy levels in magnetic fields, parahydrogen has no splitting in magnetic fields. The key feature of this “singlet” hydrogen is that its nuclear spin state (singlet state) is antisymmetric with respect to spin-exchange (or known as parity operator) whereas the “triplet” hydrogen (ortho-hydrogen) spin states are symmetric with respect to spin-exchange. This symmetry property forbids dipole moment that connects the singlet state to any other states and therefore makes it “invisible” to pulse sequence manipulation. Therefore, para-hydrogen is known as “NMR silent”. It is known that the ratio of the two isomers (ortho/para-hydrogen) at room temperature is close to 3:1. And it drops significantly with temperature; for instance, it can reach 1:1 at liquid nitrogen temperature¹⁸. Therefore, para-hydrogen can be enriched at low temperature. In 1986, Bowers and Weitekamp predicted a new means to enhance MR signal of target molecules with such enriched para-hydrogen¹⁹, namely, through a catalyzed hydrogenation reaction. Due to the symmetry property of para-hydrogen, when it is added to a target molecule, only those nuclear spin states in the product molecule get populated that have corresponding symmetry properties¹⁷. This population distribution must deviate drastically from the populations at thermal equilibrium and therefore, a large polarization is generated. Traditionally, there are two distinct procedures to accomplish PHIP. Bowers and Weitekamp named the first effect

PASADENA¹⁹ (Para-hydrogen And Synthesis Allow Dramatically Enhanced Nuclear Alignment), i.e., a hydrogenation reaction with para-hydrogen inside the magnetic field. Pravica and Weitekamp²⁰ later reported the other effect when a hydrogenation reaction with para-hydrogen happens outside the magnetic field and is followed by an adiabatic transfer of the sample into the magnet field. They named this effect ALTADENA (Adiabatic Longitudinal Transport After Dissociation Engenders Nuclear Alignment). Generally speaking, the hydrogenation reaction renders the two para-hydrogen-derived protons inequivalent, i.e., they have distinct chemical shifts (the two protons form an AB spin system in contrast to an A₂ system such as the two magnetically *equivalent* protons in para-hydrogen). Spin states in an AB system are expressed in Zeeman product states. Population distribution after PHIP and the symbolic spectra are shown in Figure 4.

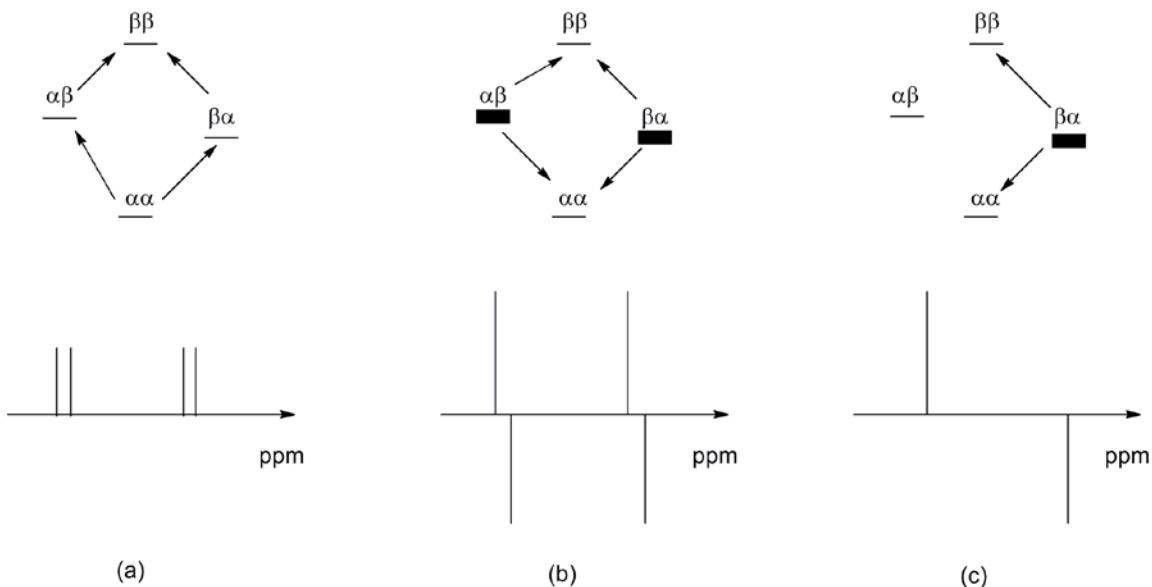


Figure 4. (From Ref ¹⁷) Population models for a 2-spin system of AB character. (a) Standard NMR system (b) PASADENA (c) ALTADENA

Although polarization enhancement from conventional PHIP may not be as high as that from DNP, it is a far more affordable approach. However, its real drawback is that hydrogenation reaction is always required. This limits the scope of molecules that can be used as a precursor; i.e., they must have unsaturated bonds. Remarkably, Duckett et al²¹⁻²² in 2009 demonstrated a new method to circumvent this constraint. They showed that a temporary association between a substrate and para-hydrogen via a transitional metal center at low magnetic fields can facilitate polarization transfer from para-hydrogen to the substrate. They named this effect NMR-SABRE (NMR-Signal Amplification By Reversible Exchange). Because the association is reversible, no formal “hydrogen receptor” is necessary. This dramatically enhances the practicality of PHIP. The reader is referred to recent literature²³⁻²⁴ for the latest advancements of SABRE and PHIP. Detailed discussion is beyond the scope of this thesis.

Despite the renewed excitement stimulated by SABRE over para-hydrogen, PHIP in general still suffers from serious limitations especially for *in vivo* imaging application, the most notable one being the challenge of efficient conversion from para-hydrogen to hyperpolarization *in vivo*. It's difficult to envision such a process, reversible (SABRE) or irreversible (PASADENA and ALTADENA), can be well-controlled *in vivo*. On the other hand, if the conversion is accomplished before *in vivo* injection, PHIP will face the same fundamental challenge as dissolution DNP, namely, the short lifetime for the hyperpolarization.

A third hyperpolarization method is optical pumping, which can only be applied to hyperpolarize stable noble-gas isotopes with nuclear spin $\frac{1}{2}$, specifically, ^3He and ^{129}Xe . It was first demonstrated²⁵⁻²⁶ in the 1960s, much earlier than PHIP and DNP. Optical pumping requires transfer of angular momentum from circularly polarized light to noble gas nucleus. This can be achieved by either of the two basic methods, namely, spin-exchange optical pumping (SEOP)²⁵ and metastability exchange optical pumping (MEOP)²⁶. The angular momentum of the laser light at certain frequency is first absorbed by either an alkali-metal vapor (SEOP) or excited metastable ^3He plasma. Subsequently, polarization is transferred from the electron spins to the noble-gas nucleus spin. T_1 relaxation time of such hyperpolarized noble gas has been thoroughly studied²⁷ and under appropriate condition, typical T_1 of hyperpolarized ^3He and ^{129}Xe can be many tens of hours²⁸, allowing convenient storage and transport. Nevertheless, *in vivo* T_1 of both ^3He and ^{129}Xe after administration is significantly shorter than one minute due to strong relaxation caused by paramagnetic species such as oxygen. Both hyperpolarized ^3He and ^{129}Xe have been administrated as inhalative “contrast agent” for lung ventilation imaging²⁷⁻²⁸. Moreover, ^{129}Xe is also used for perfusion studies in brain and blood stream due to its much larger solubility in water and tissue compared with ^3He . Resonance frequency of ^{129}Xe is also very sensitive to its chemical environment (e.g., gas phase versus dissolved phase, its binding to hemoglobin) and therefore can be used for specific molecular target recognition. Major drawback of ^{129}Xe compared with ^3He is its lower

gyromagnetic ratio which gives rise to inferior SNR and spatial resolution for imaging under otherwise identical condition. The fundamental obstacle for hyperpolarized ^3He on the other hand, is that ^3He can only be obtained from tritium decay and is formidably expensive. The reader is referred to literature²⁷⁻³⁰ for detailed reports on the most recent progress in hyperpolarized noble-gas imaging.

2. Nuclear singlet state and its key properties

2.1 Singlet and triplet states

The energy eigenstates of an isolated spin-1/2 are conventionally labeled as $|\alpha\rangle$ and $|\beta\rangle$, based on projection of their angular momentum along the z-axis (conventionally defined as the direction of the main magnetic field, B_0). The energy eigenstates for two coupled spin-1/2 are determined by the nuclear spin Hamiltonian. In general, the Hamiltonian for such 2-spin system is:

$$H_0 = H_{CS} + H_J = \omega_1 I_{z1} + \omega_2 I_{z2} + 2\pi J(I_1 \cdot I_2) \quad (2-1)$$

where ω_1 and ω_2 are the Larmor frequencies (in rad/s) for spin 1 and 2 and J is the mutual scalar coupling (in Hz). It can be rewritten in terms of the sum and difference of these frequencies:

$$H_0 = \frac{1}{2}\Sigma\omega(I_{1z} + I_{2z}) + \frac{1}{2}\Delta\omega(I_{1z} - I_{2z}) + 2\pi J(I_1 \cdot I_2) \quad (2-2).$$

The most commonly used basis set for such spin system is the Zeeman basis (Figure 5(a)), which is derived from product of the basis for two isolated spin-1/2. The Hamiltonian in such basis can be written as³¹⁻³³:

$$\begin{pmatrix} \frac{1}{2}\Sigma\omega + \frac{1}{4}\Delta\omega\tan(\theta) & 0 & 0 & 0 \\ 0 & -\frac{1}{2}\Delta\omega - \frac{1}{4}\Delta\omega\tan(\theta) & \frac{1}{2}\Delta\omega\tan(\theta) & 0 \\ 0 & \frac{1}{2}\Delta\omega\tan(\theta) & -\frac{1}{2}\Delta\omega - \frac{1}{4}\Delta\omega\tan(\theta) & 0 \\ 0 & 0 & 0 & -\frac{1}{2}\Sigma\omega + \frac{1}{4}\Delta\omega\tan(\theta) \end{pmatrix}$$

$$\text{where } \tan(\theta) = 2\pi J / \Delta\omega \quad (1-3)$$

Upon diagonalisation, the general form of the eigenbasis for the Hamiltonian is:

$$\alpha\alpha; \cos\left(\frac{\theta}{2}\right)\alpha\beta + \sin\left(\frac{\theta}{2}\right)\beta\alpha; \sin\left(\frac{\theta}{2}\right)\alpha\beta - \cos\left(\frac{\theta}{2}\right)\beta\alpha; \beta\beta \quad (2-4)$$

When the two spins are “weakly coupled”³⁴, meaning $\Delta\omega \gg 2\pi J$; $\theta \rightarrow 0$ in (2-3), the off-diagonal terms ($\frac{1}{2}\Delta\omega \tan(\theta)$) in the Hamiltonian matrix are small and frequently disregarded according to the secular approximation^{4, 8, 34}. In contrast, when the “weakly coupled” condition is violated, for example, if the two spins are magnetically *equivalent* (in the case of an isolated 2-spin system, it is equivalent to say $\Delta\omega = 0$; $\theta \rightarrow \frac{\pi}{2}$ in (2-3)), the eigenbasis for the system Hamiltonian is the so-called “Singlet-Triplet (ST)” basis (Figure 5(b)). The singlet state $|S\rangle = (\alpha\beta - \beta\alpha) / \sqrt{2}$ has zero total angular momentum and is therefore NMR silent. In contrast, the triplet states have total angular momentum equals one. Consequently, projection (m_z) of the angular momentum along B_0 can be either +1, 0 or -1, corresponding to three different energy levels ($|T_{+1}\rangle = \alpha\alpha$, $|T_0\rangle = (\alpha\beta + \beta\alpha) / \sqrt{2}$ and $|T_{-1}\rangle = \beta\beta$). One key difference between singlet state and triplet states pertains to the symmetry. The singlet state is antisymmetric with respect to exchange of the two spins whereas the triplet states are symmetric. As discussed above, this symmetry difference forbids any dipole moment that connects the singlet to the triplet states. Further implication of the anti-symmetric parity of the singlet state will be revealed in the relaxation processes discussed in the next section.

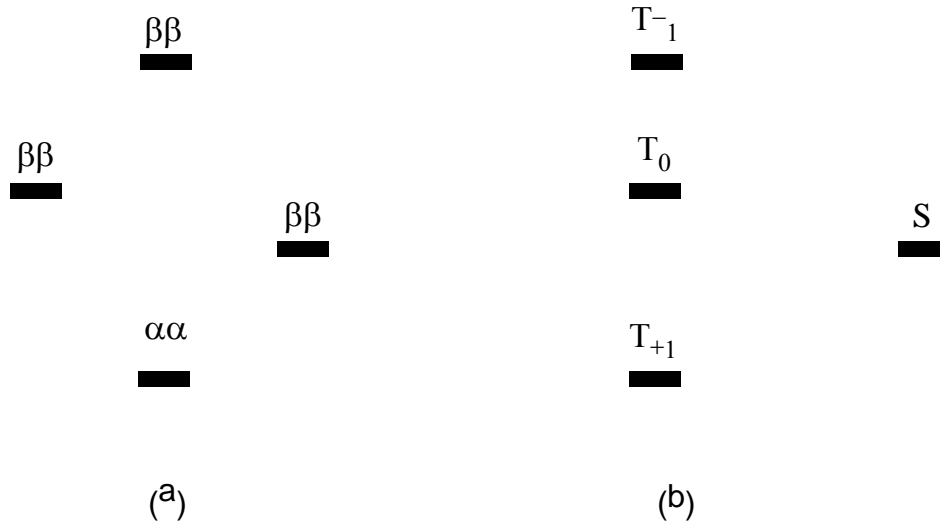


Figure 5. Energy levels for coupled two spin system. (a) Zeeman basis for the coupled two spin system, which is a good approximation to eigenstates of the spin system Hamiltonian when the two spins are weakly-coupled. (b) Singlet-Triplet basis for the coupled two spin system with $S = (\alpha\beta + \beta\alpha) / \sqrt{2}$, $T_{+1} = \alpha\alpha$, $T_0 = (\alpha\beta + \beta\alpha) / \sqrt{2}$, $T_{-1} = \beta\beta$, is the eigenbasis set for the system Hamiltonian when the two spins are magnetically *equivalent*.

The regime where $\Delta\omega \neq 0$ but $\Delta\omega \ll 2\pi J$ is referred to as “near *equivalent*”³⁵⁻³⁶, it occurs in extreme low fields (e.g., \sim mT)³⁵ or with two spins that have very small chemical shift differences. As θ approaches $\pi / 2$ in (3), the ST basis approaches the true eigenbasis for the system Hamiltonian. Nevertheless, so long as $\theta \neq 0$, there is a mixing effect between the singlet and triplet (T_0) state and the mixing rate is proportional to $\tan^2(\theta)$ ³¹⁻³² according to the second-order perturbation theory.

2.2 Relaxation properties of the singlet state

Nuclear magnetization relaxation theory was first introduced by Bloembergen et al in 1948³⁷. The most applicable formulation of relaxation theory so far has been the

Wangsness, Bloch and Redfield (WBR) theory or the Redfield theory³⁸. Readers are referred to the literatures for a formal and thorough treatment of relaxation theory^{2-4, 39-40}, including recent progress and applications in liquid state NMR⁴¹. Here only a brief introduction to the key results is provided, closely following the notation used in ref [40-42]. It is worth noting that in these classic relaxation studies, the 2-spin singlet state has been always neglected for it is unobservable in NMR and therefore has been viewed as of little practical significance. In fact, most of these treatments were conducted with the eigenbasis of the system Hamiltonian, usually the Zeeman basis. Nevertheless, the practicality of using singlet state has been realized since the development of hyperpolarization, especially dissolution DNP. The extremely slow relaxation of the singlet state was first revealed by Levitt et al³⁵⁻³⁶ in 2004 when they showed the coherent mixing between the singlet and triplet states can be suppressed by well-known NMR procedures. Since then, pioneered by Levitt et al^{31-32, 43-46}, detailed studies of the singlet state relaxation property have been conducted with modified Redfield theory using the ST basis. A compact summary of their results constitutes the second part of this section. In principle, such long-lived states also can exist in multi-spin system with peculiar symmetry properties⁴⁷⁻⁴⁹, although access to such states might be difficult. This will be covered at the end of this section.

2.2.1 Bloch-Redfield-Wangsness (BRW) relaxation theory

Redfield theory is also known as the semi-classical relaxation theory, which means the spin system is treated quantum mechanically while the “lattice” is treated classically. In essence, Redfield theory is a second-order perturbative spin relaxation theory. The fundamental challenge of describing relaxation process is that the time scale of relaxation is ultrafast (femtoseconds to picoseconds) compared with multi-second NMR dynamics, making it impossible if we aim to resolve the explicit time dependence of such process. Instead, Redfield theory relies on the energy spectrum (known as spectral density) of these fluctuations and the corresponding statistical properties to estimate the overall relaxation process. Started from Liouville-von Neumann equation we have:

$$\frac{d\sigma}{dt} = -i[H, \sigma] \text{ and } H = H_0 + H_1(t) \quad (2-5)$$

Where H_0 denotes the time-independent part of the spin Hamiltonian, such as Zeeman interactions while $H_1(t)$ denotes the time-dependent part of the Hamiltonian which averages to zero, such as time-modulated molecular motions, any non-zero average can be moved into H_0 . To separate out the time-dependent part of Hamiltonian, (5) is transformed into the interaction representation:

$$\frac{d\tilde{\sigma}}{dt} = -i[\tilde{H}_1(t), \tilde{\sigma}] \quad (2-6)$$

Where tilde denotes the interaction representation with respect to H_0 , for instance, $\tilde{H}_1(t) = e^{iH_0 t} H_1(t) e^{-iH_0 t}$. Integration of (2-6) generates:

$$\tilde{\sigma}(t) = \tilde{\sigma}(0) - i \int_0^t [\tilde{H}_1(t'), \tilde{\sigma}(t')] dt' \quad (2-7)$$

insert the resulted $\tilde{\sigma}(t)$ back to the right side of (2-6), we have:

$$\frac{d\tilde{\sigma}(t)}{dt} = -i[\tilde{H}_1(t), \tilde{\sigma}(0)] - \int_0^t [\tilde{H}_1(t), [\tilde{H}_1(t'), \tilde{\sigma}(t')]] dt' \quad (2-8)$$

The derivation so far is rigorous, if now we perform ensemble averaging over all spins assuming they started from the same initial density matrix $\tilde{\sigma}(0)$, then:

$$\langle [\tilde{H}_1(t), \tilde{\sigma}(0)] \rangle = 0, \text{ therefore (7) becomes:}$$

$$\frac{\partial \langle \tilde{\sigma}(t) \rangle}{\partial t} = - \int_0^t \langle [\tilde{H}_1(t), [\tilde{H}_1(t'), \tilde{\sigma}(t')]] \rangle dt' \quad (2-9)$$

Now it's desirable to transform from the Hilbert space to the superoperator space (also known as Liouville space) to keep derivations compact and also for the purpose of practical simulation⁵⁰⁻⁵¹. Detailed discussion of Liouville space is beyond the scope of this thesis, again readers are referred to literatures for its applications in nuclear spin dynamics^{2, 4, 42, 50-51}. Liouville space is a space of operators instead of state functions and superoperator achieves transformation between operators. The most relevant superoperator for the relaxation theory is the commutation superoperator. For instance, the superoperator for $[H_1, \cdot]$ is denoted as \hat{H}_1 , which can be calculated by:

$$\hat{H}_1 = [H_1,] = E \otimes H_1 - H_1 \otimes E \quad (2-10)$$

Where \otimes denotes the Kronecker product and E is the identity operator. Then the exponential of a commutation superoperator which generates evolution is:

$$e^{-i\hat{H}\Delta t} \sigma(t) = e^{-iH\Delta t} \sigma(t) e^{iH\Delta t} \quad (2-11)$$

Accordingly, (2-9) can be rewritten with (2-10) as:

$$\frac{\partial \langle \tilde{\sigma}(t) \rangle}{\partial t} = - \int_0^t \langle \hat{H}_1(t) \hat{H}_1(t') \tilde{\sigma}(t') \rangle dt' \quad (2-12)$$

Where tilde is retained to denote the rotating frame with respect to H_0 , namely:

$$\hat{H}_1(t) = e^{i\hat{H}_0 t} \hat{H}_1(t) e^{-i\hat{H}_0 t} \quad (2-13)$$

Although H_1 is time-dependent, it can be decomposed into linear combinations of time-independent operators \hat{Q} with time-dependent complex coefficients $q(t)$:

$$\hat{H}_1(t) = \sum_k q_k(t) \hat{Q}_k = \sum_m q_m^*(t) \hat{Q}_m^+ \quad (2-14)$$

Note in order to facilitate subsequent treatment, one copy of $\hat{H}_1(t)$ can be written in the conjugate form. With (2-14), (2-12) can be rewritten as:

$$\frac{\partial \langle \tilde{\sigma}(t) \rangle}{\partial t} = - \sum_{km} \int_0^t \langle q_k(t) q_m^*(t') \hat{Q}_k(t) \hat{Q}_m^+(t') \tilde{\sigma}(t') \rangle dt', \quad \hat{Q}(t) = e^{i\hat{H}_0 t} \hat{Q} e^{-i\hat{H}_0 t} \quad (2-15)$$

From here, three key assumptions are made. First, we assume the spin system dynamics is uncorrelated with the stochastic noise in $H_1(t)$ since the norm of H_1 is much smaller than that of H_0 . Consequently, ensemble average can be applied separately to the

density matrix and to the perturbative H_1 . Also, $\hat{\hat{Q}}(t)$ can be taken out from the average since its time-dependence is deterministic which comes from transformation to the interactive representation. Second, we assume the stochastic noise in $H_1(t)$ is stationary, namely, $\langle q_k(t)q_m^*(t') \rangle$, defined as the correlation function for $q(t)$, only depends on the time separation between t and t' . If we change variable t' to $\tau = t - t'$, then

$$g_{km}(\tau) = \langle q_k(t)q_m^*(t') \rangle = \langle q_k(t)q_m^*(t-\tau) \rangle. \quad (2-16)$$

The last assumption is the correlation function $g(\tau)$ decays so fast that within that time the spin system barely evolves, therefore, $\langle \tilde{\sigma}(t) \rangle$ can be taken out from the integration in (14). Moreover, the upper limit for the integration in (14) can be extended to infinity due to the fact $g(\tau)$ quickly decays to zero. Accordingly, (14) becomes:

$$\frac{\partial \tilde{\sigma}(t)}{\partial t} = - \left[\sum_{km} \int_0^\infty g_{km}(\tau) \hat{\hat{Q}}_k(t) \hat{\hat{Q}}_m^+(t-\tau) d\tau \right] \tilde{\sigma}(t) \quad (2-17)$$

Note we have also dropped the ensemble notation (angular brackets) for the density matrix for convenience. Return to lab-frame representation, we have:

$$\frac{\partial \sigma(t)}{\partial t} = -i\hat{H}_0 \sigma(t) - \left[\sum_{km} \int_0^\infty g_{km}(\tau) \hat{Q}_k e^{-i\hat{H}_0\tau} \hat{Q}_m^+ e^{i\hat{H}_0\tau} d\tau \right] \sigma(t) \quad (2-18)$$

This gives the general form of the relaxation superoperator, $\hat{\hat{R}}$:

$$\hat{\hat{R}} = - \sum_{km} \int_0^\infty g_{km}(\tau) \hat{Q}_k e^{-i\hat{H}_0\tau} \hat{Q}_m^+ e^{i\hat{H}_0\tau} d\tau = - \sum_{km} \int_0^\infty g_{km}(\tau) [\hat{Q}_k, [e^{-i\hat{H}_0\tau} \hat{Q}_m^+ e^{i\hat{H}_0\tau}, \cdot]] d\tau \quad (2-19)$$

And (2-18) can be simplified to:

$$\frac{\partial \sigma(t)}{\partial t} = -i\hat{H}_0 \sigma(t) + \hat{R} \sigma(t) \quad (2-20)$$

This is the Master Equation. It shows evolution of the spin density matrix is driven by “coherent” influences denoted by \hat{H}_0 (i.e., which are the same for all ensemble spins) and “incoherent” interactions denoted by \hat{R} (i.e., which are inhomogeneous over the spin ensemble and fluctuate over time). One caveat of (2-20) is it relaxes all states to equal population, which according to Boltzmann distribution, corresponds to infinite high temperature. One approach to correct for finite temperature is to add a phenomenological term σ_{eq} , which is the thermal equilibrium form of the density matrix for the Hamiltonian H_0 , then (2-20) becomes:

$$\frac{\partial \sigma(t)}{\partial t} = -i\hat{H}_0 \sigma(t) + \hat{R}(\sigma(t) - \sigma_{eq}) \quad (2-21)$$

So far the only thing untouched is the exact form of the correlation function defined in (15). If we limit the discussion to the simplest case where small molecules are viewed as rigid spherical objects that undergo an isotropic rotational diffusion, one can show that $g_{km}(\tau)$ is proportional to $e^{-\tau/\tau_c}$, where τ_c is known as the rotational correlation time, which is associated with the viscosity of the solvent, the hydrodynamic radius of the molecule and the temperature.

To facilitate numerical evaluation, spectral density function is defined as:

$$J_{km}(\omega) = \int_0^{\infty} g_{km}(\tau) e^{i\omega\tau} d\tau = \frac{\tau_c}{1 + \omega^2 \tau_c^2} - i \frac{\omega \tau_c^2}{1 + \omega^2 \tau_c^2} \quad (2-22)$$

The real part determines the relaxation rate while the usually much smaller imaginary part produces a shift of the resonance frequencies, which will be neglected in the following discussion. Then the integration in (2-19) can be transformed into a collection of Fourier transforms:

$$\hat{R} = - \sum_{km} J_{km}(\omega) \hat{Q}_k \hat{Q}_m^+ \quad (2-23)$$

Accordingly, specific relaxation rate can be evaluated. After somewhat tedious manipulation, one can show:

$$\langle \hat{\rho}_a | \hat{R} | \hat{\rho}_b \rangle = - \sum_{ijkm} [\hat{Q}_m^+]_{ij} [\hat{P}_k^{(a,b)}]_{ji} J_{km}(\omega_{ij}) \quad (2-24)$$

Where $\hat{P}_k^{(a,b)} = [\hat{\rho}_a, [\hat{\rho}_b^+, \hat{Q}_k]]$, $\omega_{ij} = \omega_i - \omega_j$ and $\omega_{i,j}$ are the *i*th and *j*th eigenvalues of H_0 . Subsequent evaluation of (2-24) is only possible when the exact form of perturbative $H_1(t)$ is known, which stems from different relaxation mechanisms. For small molecules at liquid phase, the most dominant effects are the dipole-dipole interaction (DD) and the chemical shielding anisotropy (CSA), although other mechanisms such as spin rotation (SR) can also be important. Here I only give a brief introduction to the DD and CSA-driven relaxations and the general form of \hat{R} for these two effects are summarized below, readers are redirected to ref [2-4, 40-41] for more thorough discussions.

DD and CSA-driven relaxations are caused by random motion of small molecules and different models can be assumed to approximate such motions. Again discussion is limited to the simplest case where small molecules are viewed as rigid spherical objects that undergo an isotropic tumbling. With this assumption, we can derive the DD-driven relaxation superoperator \hat{R}_{DD} as follows: The dipole-dipole Hamiltonian between two nuclei spins I and S is:

$$\hat{H}_{DD} = -\frac{\mu_0\gamma_I\gamma_S\hbar}{4\pi r^3} \left(3\hat{I} \cdot \frac{\bar{r}}{r^2} \cdot \hat{S} - \hat{I} \cdot \hat{S} \right) = b_{IS} \hat{I} \cdot D \cdot \hat{S}, \text{ where } b_{IS} = -\frac{\mu_0\gamma_I\gamma_S\hbar}{4\pi r^3} \quad (2-25)$$

b_{IS} is often denoted as the dipole-dipole coupling constant, \bar{r} denotes the vector connecting the two spins, γ_I and γ_S are the gyromagnetic ratios for spin I and S , μ_0 is the vacuum permeability and D is the dipolar tensor. Interactions such as the dipole-dipole Hamiltonian in (2-25) are anisotropic bilinear interactions and can be generally expanded as⁴²:

$$\hat{H}_{DD} = \frac{Ax}{\sqrt{6}} \hat{T}_0^{(2)} + \frac{Rh}{2} \left[\hat{T}_{-2}^{(2)} + \hat{T}_2^{(2)} \right] \quad (2-26)$$

Where $T_m^{(2)}$ are the second-rank irreducible spherical tensors (IST).

$Ax = 2D_{zz} - (D_{xx} + D_{yy})$ and $Rh = D_{xx} - D_{yy}$, they are denoted as the axiality and rhombicity of the interaction tensor and $D_{xx,yy,zz}$ are the diagonal values of the tensor in its eigenframe (also known as principle axis frame in which the off-diagonal elements are zero). The rank-2 IST for dipole-dipole interaction is listed in Table 2. The main reason for choosing to work with ISTs is that they have convenient behavior under

rotation operation, namely, rotation converts IST into linear combinations of other IST of the same rank:

$$\hat{\mathcal{D}}(\alpha, \beta, \gamma) \hat{T}_m^{(l)} = \sum_{m'=-l}^l \hat{T}_{m'}^{(l)} \mathcal{D}_{m,m'}^{(l)}(\alpha, \beta, \gamma) \quad (2-27)$$

Where $\hat{\mathcal{D}}(\alpha, \beta, \gamma)$ denotes the rotation defined by a set of Euler angles α, β, γ and $\mathcal{D}_{m,m'}^{(l)}(\alpha, \beta, \gamma)$ is the Wigner function⁵². Accordingly, the time dependence of the dipole-dipole Hamiltonian (2-25) due to stochastic rotational diffusion of the molecule can be expressed as:

$$\hat{H}_{DD}(t) = \hat{\mathcal{D}}(t) \hat{H}_{DD} = \sum_{m=-2}^2 \left[\frac{Ax}{\sqrt{6}} \mathcal{D}_{m,0}^{(2)}(t) + \frac{Rh}{2} \left(\mathcal{D}_{m,-2}^{(2)}(t) + \mathcal{D}_{m,2}^{(2)}(t) \right) \right] \hat{T}_m^{(2)} \quad (2-28)$$

Comparing with (2-14), we get:

$$q_m(t) = \frac{Ax}{\sqrt{6}} \mathcal{D}_{m,0}^{(2)}(t) + \frac{Rh}{2} \left(\mathcal{D}_{m,-2}^{(2)}(t) + \mathcal{D}_{m,2}^{(2)}(t) \right) \quad \text{and} \quad \hat{Q}_m = \hat{T}_m^{(2)}. \quad \text{Accordingly, the}$$

correlation function can be obtained as:

$$g_{km}(\tau) = \langle q_k(0) q_m^*(\tau) \rangle = \dots = \frac{\Delta_A^2}{30} \delta_{km} e^{-\tau/\tau_c}, \Delta_A^2 = Ax^2 + 3Rh^2 \quad (2-29)$$

For point dipole-dipole interaction $Ax = 6 \frac{\gamma_I^2 \gamma_S^2 \hbar^2}{r^3} \frac{\mu_0}{4\pi}$ and $Rh = 0$. Finally the

explicit form of (2-19) for DD relaxation can be written as:

$$\hat{R} = -\frac{\Delta_A^2}{30} \sum_{m=-2}^2 \int_0^\infty e^{-\tau/\tau_c} \hat{T}_m^{(2)} e^{-i\hat{H}_0\tau} \hat{T}_m^{(2)+} e^{i\hat{H}_0\tau} d\tau \quad (2-30)$$

Then (2-24) can be invoked to evaluate matrix elements of \hat{R} , for example, the longitudinal relaxation rate for I_z is:

$$\frac{1}{T_1^{I,DD}} = -\text{Re} \frac{\langle \hat{I}_z | \hat{R} | \hat{I}_z \rangle}{\langle \hat{I}_z | \hat{I}_z \rangle} = \frac{\Delta_A^2 \tau_c}{360} \left(\frac{3}{1 + \omega_I^2 \tau_c^2} + \frac{6}{1 + (\omega_I + \omega_S)^2 \tau_c^2} + \frac{1}{1 + (\omega_I - \omega_S)^2 \tau_c^2} \right) \quad (2-31)$$

One important limiting case is called “extreme narrowing”, where $\tau_c \ll 1/\omega_{I,S}$.

This is always valid for relaxation of small molecules in nonviscous solvent. Then (2-31)

simplifies to:

$$\frac{1}{T_1^{I,DD}} = \frac{\Delta_A^2 \tau_c}{36} \quad (2-32)$$

Since Δ_A is independent of the magnetic field strength (B_0), $T_1^{I,DD}$ in the extreme narrowing limit (2-32) is also independent of B_0 .

Likewise, relaxation rate due to CSA can be derived in a similar way. CSA denotes the anisotropy of the Zeeman interaction between the nuclei and external magnetic field. It originates from the anisotropic electron spin-orbit coupling. Therefore, CSA of proton is small while it is significant for other nuclei such as ^{13}C , ^{15}N and ^{19}F . The CSA interaction Hamiltonian for a single spin I can be written as:

$$\hat{H}_{\text{CSA}} = \gamma_I I \cdot \sigma \cdot B_0 \quad (2-33)$$

Where σ is the shielding tensor and B_0 is assumed to align with the z-axis of the lab frame. The same decomposition to IST can be used to get:

$$\hat{H}_{CSA}(t) = \sum_{m=-2}^2 \left[\frac{Ax}{\sqrt{6}} \mathcal{S}_{m,0}^{(2)}(t) + \frac{Rh}{2} \left(\mathcal{S}_{m,-2}^{(2)}(t) + \mathcal{S}_{m,2}^{(2)}(t) \right) \right] \hat{T}_m^{(2)} \quad (2-34)$$

Where Ax and Rh are defined the same as before but refer to the Zeeman shielding tensor σ and the second-rank ISTs for CSA are listed in Table 2. Following the same procedure from (2-28) to (2-31), we have:

$$\frac{1}{T_1^{I,CSA}} = \frac{\Delta_A^2}{30} \frac{\tau_c}{1 + \tau_c^2 \omega_I^2} = \frac{(\gamma_I B_0 Ax)^2}{30} \frac{\tau_c}{1 + \tau_c^2 \omega_I^2} \quad (2-35)$$

Again in the extreme narrowing limit, we have $\tau_c \omega_I \ll 1$ and (2-35) becomes:

$$\frac{1}{T_1^{I,CSA}} = \frac{(\gamma_I B_0 Ax)^2 \tau_c}{30} \quad (2-36)$$

In contrast to (2-32), (2-36) has a quadratic dependence on B_0 . Therefore, CSA-driven relaxation is dramatically more important with increased field strength. This concludes the brief introduction to the Redfield relaxation theory.

Table 2. Irreducible spherical tensors for spin dipole-dipole interaction (DD) and chemical shielding anisotropy (CSA)

$T_m^{(2)}$	$m=0$	$m=\pm 1$	$m=\pm 2$
DD	$\sqrt{\frac{1}{6}} (3\hat{I}_{iz}\hat{I}_{jz} - \hat{I}_i \cdot \hat{I}_j)$	$\mp \frac{1}{2} (\hat{I}_{i\pm}\hat{I}_{jz} + \hat{I}_{iz}\hat{I}_{j\pm})$	$\frac{1}{2} \hat{I}_{i\pm}\hat{I}_{j\pm}$
CSA	$\sqrt{\frac{2}{3}} \hat{I}_z \hat{B}_0$	$\mp \frac{1}{2} \hat{I}_{\pm} \hat{B}_0$	0

2.2.2 Relaxation property of the singlet and other long-lived states

The central relaxation property of the 2-spin singlet state is that it is immune to the intra-pair dipole-dipole (iDD) relaxation, which is the dominant mechanism for T_1 relaxation on the two spins. Therefore, the singlet state lifetime (often denoted as T_S) can often outlast T_1 by more than an order of magnitude. To see why the singlet state is immune to iDD relaxation, notice in equation (2-30) of the previous section the DD relaxation \hat{R} decomposes into commutation superoperators of the second-rank ISTs, $\hat{T}_m^{(2)}$. On the other hand, the singlet state ($|S\rangle \equiv \frac{1}{\sqrt{2}}|\alpha\beta - \beta\alpha\rangle$) can be written in the Liouville space operator as:

$$|S\rangle\langle S| \equiv \frac{1}{4}\hat{E} - I_1 \cdot I_2 \equiv \frac{1}{4}\hat{E} + \sqrt{3}T_0^{(0)} \quad (2-37)$$

Where \hat{E} is the identity operator that does not evolve, therefore, the singlet state operator is proportional to $T_0^{(0)}$, namely, the rank-0 tensor for two spins, which is spherically symmetric. It is then straightforward to verify that $\hat{T}_m^{(2)}\hat{T}_0^{(0)} = [\hat{T}_m^{(2)}, \hat{T}_0^{(0)}] = 0$. Therefore, the singlet state does not evolve under the iDD relaxation. Likewise, one can easily verify the singlet state population does not evolve under any tensor operators that act symmetrically on the two spins. For instance, it is evident that the intra-pair J-coupling does not evolve the singlet state because $J I_1 \cdot I_2$ is also proportional to $T_0^{(0)}$. Therefore, the only effective mechanisms are for example, the chemical shift difference between the two spins, $\Delta\omega(I_{1z} - I_{2z})$, which induces mixing between the S and T_0 state.

This coherent effect can lead to relaxation because the T_0 state is exposed to all relaxation mechanisms such as the intra-pair DD relaxation. Similarly, if a third spin is J-coupled differently to the two spins, the same mixing between S and T_0 can occur even when the two spins are *chemically equivalent* ($\Delta\omega=0$), therefore, relaxation to the singlet state occurs indirectly through the T_0 state.

The second most important incoherent relaxation effect for such strongly-coupled two spins is CSA. As discussed in the previous section, CSA-driven relaxation can be written in the “spin-field” tensors (second row in Table 2). Therefore, consider only the spin operator; they are essentially rank-1 single spin ISTs. It can be verified that $[T_0^{(0)}, T_m^{(1)}] \neq 0$ and thus the singlet state is not immune to CSA-driven relaxation. It has been shown⁴⁵ however; the singlet state is exposed to the CSA-driven relaxation to a much lesser extent compared with T_1 . Specifically, the singlet state is only exposed to the difference of the chemical shielding tensors of the two spins, $\Delta\sigma = \sigma_1 - \sigma_2$. Therefore, when local magnetic fields are identical for the two spins, the singlet state is immune to CSA-driven relaxation. This property of the singlet state being only affected by “uncorrelated” part of relaxation is also seen in relaxation caused by “out of pair” dipole-dipole coupling⁵³, spin-rotation⁵⁴ and scalar coupling of the second kind⁴⁴. Therefore, the additive relaxation rate from these mechanisms can be dramatically slower for the singlet state than conventional T_1 relaxation.

Having explained the long-lived nature of the 2-spin singlet state, an interesting question would be whether collective long-lived states of more than two spins exist^{47-49, 55-57}. Assuming intra-molecular DD interaction is the dominant source for relaxation, this question amounts to find states which do not evolve under the total DD Hamiltonian, namely, the null-space for \hat{R}_{DD} ⁴⁷. As pointed out by Hogben⁴⁷ et al, because linear combinations or products of pair-wise singlet state are invariant under sum of bilinear dipolar operators in (2-25), one would expect such long-lived states exist. A key insight from the same paper is that long-lived states are mostly likely formed from combination or product of singlets across spins that are interchanged by inversion symmetry. However, this does not preclude the existence of fairly long-lived states that are formed from the singlets across two strongly-coupled spins (e.g., spins with minimum separation) that are not “inversion-related” as long as such spin pair interacts weakly with other spins. Such long-lived states formed from localized singlet state constitute most examples of this thesis and dramatic lifetime extension is often observed when an inversion center exists. People need to be reminded that other relaxation sources such as CSA and coherent mixing with the triplet state is not negligible. In fact, a well-controlled coherent mixing is highly critical to suppress such relaxation while keeping available the access to the long-lived states. This will be discussed in the next few chapters.

3. Accessing long-lived nuclear spin states

As discussed in previous chapters, the singlet state across two *magnetically equivalent* spins has no symmetry-allowed dipole transition to any other states and is therefore extremely long-lived. However, the exact same property makes these states inaccessible. For example, spin population in para-hydrogen is intrinsically long-lived but undetectable with NMR until the symmetry is broken. The most obvious way to make the singlet accessible is by chemical reactions that render the two protons *inequivalent*. If the two spins have a significant chemical shift difference (much larger than the scalar coupling between the two spins) the singlet state is accessible by simple pulse sequences; however, it is exposed to fast relaxation due to coherent mixing with the triplet state. To surmount this challenge, Levitt et al³⁵⁻³⁶ demonstrated two methods to suppress the chemical shift difference when the long-lived nature of the singlet state is desired, and to restore the *inequivalence* for interconversion between the singlet and bulk magnetization, which I will discuss in section 3.1. However, these methods generally require large power dissipation. Warren and coworkers showed that long-lived states could be accessed between equivalent spins using chemical transformations (section 3.2) which avoids the power dissipation problem but has challenges in terms of generality. More recently, systems which are either nearly equivalent (chemical shift difference small compared to the J coupling), which I will discuss in section 3.3, or have multiple pairs of chemically equivalent spins (no chemical shift difference), which I will

discuss in section 3.4, have been explored. As in section 3.2, long-lived states can persist without significant power dissipation, but now they can be accessed by pulse sequences. At this time, the nearly-equivalent and chemically equivalent cases look to be the most promising approaches.

3.1 Accessing the long-lived singlet state between inequivalent spins

For two inequivalent spins ($\Delta\omega \gg J$) in a high field magnet (e.g., 1~7 T), the eigenbasis for the system Hamiltonian (equation (4) in Chapter 1) is close to the Zeeman basis. The singlet state population can be written as:

$$\begin{aligned}
 P_S &= \frac{1}{2} |\alpha\beta - \beta\alpha\rangle \langle \alpha\beta - \beta\alpha| = \frac{1}{2} (|\alpha\beta\rangle \langle \alpha\beta| - |\beta\alpha\rangle \langle \alpha\beta| - |\alpha\beta\rangle \langle \beta\alpha| + |\beta\alpha\rangle \langle \beta\alpha|) \\
 &= -\frac{1}{2} (I_1^+ I_2^- + I_1^- I_2^+) - I_{1z} I_{2z} + \frac{1}{4} E
 \end{aligned} \tag{3-1}$$

This shows the singlet state can be prepared from the two-spin longitudinal order ($I_{1z} I_{2z}$), the zero-quantum coherence ($I_1^+ I_2^- + I_1^- I_2^+$) or combination of the two. Multiple pulse sequences with varied efficiencies have been demonstrated⁵⁸ to achieve this goal; the simplest being a single selective inversion pulse on either of the two spins, which converts the bulk magnetization into a population difference between the $|\alpha\beta\rangle \langle \alpha\beta|$ and $|\beta\alpha\rangle \langle \beta\alpha|$ states (equivalent to $I_{1z} - I_{2z}$). Then either of the following approaches can be invoked to suppress the chemical shift difference and to render the singlet state an eigenstate of the spin system Hamiltonian.

The first approach^{31, 35} is to adiabatically transport the sample from high field to low field (\sim mT). Because the chemical shift difference between the two spins scales linearly with B_0 while the scalar coupling is independent of the field strength, the 2-spin system enters the “strongly-coupled” regime ($\Delta\omega \ll J$) when transported to low field. The eigenbasis sets also transform from the Zeeman basis set (Figure 5(a)) to the “Singlet-Triplet” basis set (Figure 5(b)). Specifically, the adiabatic transport converts the spin population on either $|\alpha\beta\rangle\langle\alpha\beta|$ or $|\beta\alpha\rangle\langle\beta\alpha|$ into the population on the singlet state, which is well-protected from relaxation.

The second approach to suppress the chemical shift difference is to apply a spin-locking field^{32, 36}. The chemical shift difference between the two spins can be artificially removed by implementing a strong radio frequency (rf) field ($>10\Delta\omega$) during the relaxation delay. Then the singlet state becomes long-lived even within the high field magnet.

Final detection of the singlet state signal can be achieved by either transporting the sample back to high field or removing the spin-locking field, both of which recover the *inequivalence* condition and a similar pulse sequence as that used for preparation can be applied to convert the singlet state population back to bulk magnetization.

With these two methods, multiple molecules have been shown to bear such long-lived singlet state. For example, a T_s of 26 min was observed on $^{15}\text{N}_2\text{O}$ when the sample was kept at around 2mT, a T_1 of 2.5 min was measured at the same field strength⁵⁴.

Nevertheless, the fundamental challenges of these two methods pose questions to general application of such long-lived states, especially to imaging purposes. Shuttling patients in and out of the magnet may induce nausea and high power irradiation raises safety concerns over energy deposition. For example, it was estimated⁵⁹ that such an experiment with a 100-second spin-lock pulse can generate heat that is 10,000 times the allowable power deposition limit, specified by the “specific absorption rate” (SAR). Consequently, it was hard to envision application of such methods to HP-MRS.

3.2 Accessing the long-lived singlet state between chemically equivalent spins

A fundamentally different approach was proposed by Warren et al⁶⁰ in 2009. The singlet state between a pair of chemically equivalent spins ($\Delta\omega = 0$) was used to store a long-lived signal. The difference between chemical equivalence and magnetic equivalence is subtle: both require identical chemical shift, usually imposed by the symmetry. However, magnetic equivalence also requires the considered spins to be equally coupled to any external spins, which is satisfied if no other spins exist in the system. In contrast, chemical equivalence permits different J-couplings that connect the considered spins to external spins. Per-deuterated 2,3-¹³C₂-diacetyl (Figure 6) used in Ref[60] is a good example showing two spins that are chemically equivalent but not magnetically equivalent. In this symmetric molecule, the two ¹³C spins are evidently chemically equivalent ($\Delta\omega = 0$) yet, they are coupled differently to either one of the per-

deuterated methyl groups ($J_{CD} \neq J_{CD}'$), which violates the condition for magnetic equivalence.

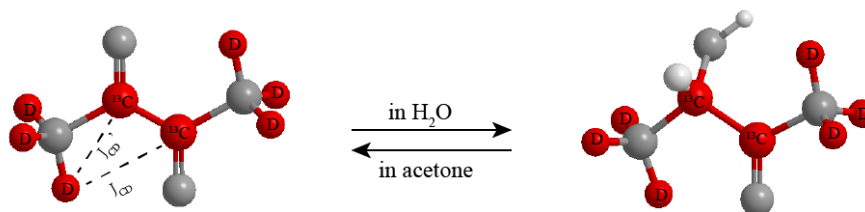


Figure 6. Per-deuterated 2,3- $^{13}\text{C}_2$ -diacetyl. The dehydrated form (left) is stable in acetone and is symmetric but the two ^{13}C spins are coupled differently ($J_{CD} \neq J_{CD}'$) to the same deuterium, therefore they are *chemically equivalent* but not *magnetically equivalent*. The hydrated form (right) is asymmetric and therefore the two ^{13}C spins are *inequivalent*.

Because the two ^{13}C spins are chemically equivalent and their mutual J coupling ($J_{CC} = 45$ Hz) dominates over couplings that connect them to the deuterium ($J_{CD}, J_{CD}' \leq 1$ Hz), the $^{13}\text{C}_2$ -singlet state is intrinsically an eigenstate of the system Hamiltonian regardless of external field strength. Therefore, the singlet state is long-lived in high field without high power irradiation. However, chemical equivalence also poses an obstacle to access the singlet state. This was solved by temporarily breaking the symmetry using chemical transformation. Specifically, hydration of diacetyl in aqueous solution makes the two ^{13}C spins inequivalent (Figure 6, right). Then access to the singlet state is provided by the chemical shift difference. Moving the sample back to acetone dehydrates diacetyl and recovers chemical equivalence. Because a well-controlled

chemical transformation is required for this method, it is difficult to envision its broad application. Nonetheless, the key insight of using “self-sustained” singlet state to store long-lived signal has certainly stimulated development of the later methods.

3.3 Accessing the long-lived singlet state between near equivalent spins

To circumvent the need for high power rf irradiation or shuttling sample in and out of high field, in 2011, Levitt et al⁶¹⁻⁶² demonstrated a pulse sequence (M2S-S2M, Figure 7, denoted as “MSM” later in discussion) that can access the long-lived state between a pair of near equivalent spins ($\Delta\omega \ll J$). The small chemical shift difference cannot induce significant perturbation on the singlet state while it also fails to provide a direct access to such state. However, a rather sophisticated coherence pathway was revealed by the MSM sequence that can drive bulk magnetization into the singlet state population.

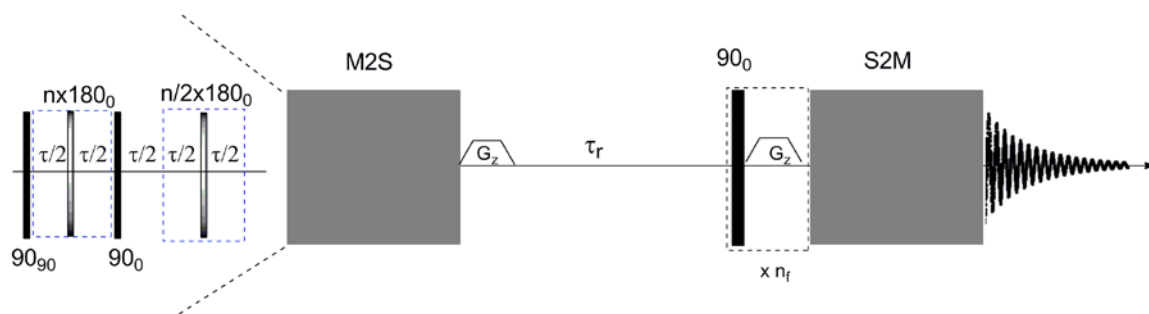


Figure 7. The M2S-S2M sequence. M2S (“magnetization to singlet”) converts bulk magnetization into the singlet state population. The sequence is composed of two blocks of precisely-spaced multiple echo pulse train and two 90° pulses (one as the excitation pulse the other separates the two blocks of 180° s). Phase of the pulses are

specified as subscripts. The first multiple echo sequence contains n 180° s, n is given by equation (41) and the second contains $n/2$ 180° s. Between M2S and S2M is the waiting time for relaxation (τ_r). For experiments conducted at thermal equilibrium, filters are necessary to suppress residual thermal signals that relax on time scale of T_1 . For example, a z-gradient is implemented immediately after the M2S to suppress spurious coherences⁵⁷. Repetitions of 90° - G_z are also desirable to remove the fast-decaying component of the final signal. n_f denotes the number of repetitions. Then S2M (“singlet to magnetization”) converts the singlet state population back to bulk magnetization for detection. S2M is the exact chronological reverse of M2S.

The key is to accumulate the small S - T_0 mixing caused by the chemical shift difference. This is achieved by putting the multiple echo sequence in the MSM in resonance with the coherent mixing. The resonance condition for the mixing effect is concealed in the spin system Hamiltonian (equation (1-1)). The full matrix representation of the Hamiltonian in the ST basis is:

$$\begin{array}{ccccc}
 & |T_{+1}\rangle & |T_0\rangle & |S\rangle & |T_{-1}\rangle \\
 H = \langle T_{+1}| & \frac{1}{2}(\pi J + \Sigma\omega) & 0 & 0 & 0 \\
 \langle T_0| & 0 & \frac{1}{2}\pi J & \frac{1}{2}\Delta\omega & 0 \\
 \langle S| & 0 & \frac{1}{2}\Delta\omega & -\frac{3}{2}\pi J & 0 \\
 \langle T_{-1}| & 0 & 0 & 0 & \frac{1}{2}(\pi J - \Sigma\omega)
 \end{array} \quad (3-2)$$

where $\Sigma\omega$ and $\Delta\omega$ are the sum and difference of the chemical shifts of the two spins. $|T_{+1}\rangle$ and $|T_{-1}\rangle$ are exact eigenstates whereas $|T_0\rangle$ and $|S\rangle$ are interconnected by $\frac{1}{2}\Delta\omega$. This isolated 2-level system composed of $|T_0\rangle$ and $|S\rangle$ is isomorphic to a well-

known 2-level problem, namely, irradiation of a single spin $\frac{1}{2}$ in a strong B_0 field along \hat{z} by a much weaker B_1 field along \hat{x} . The full Hamiltonian in that case is:

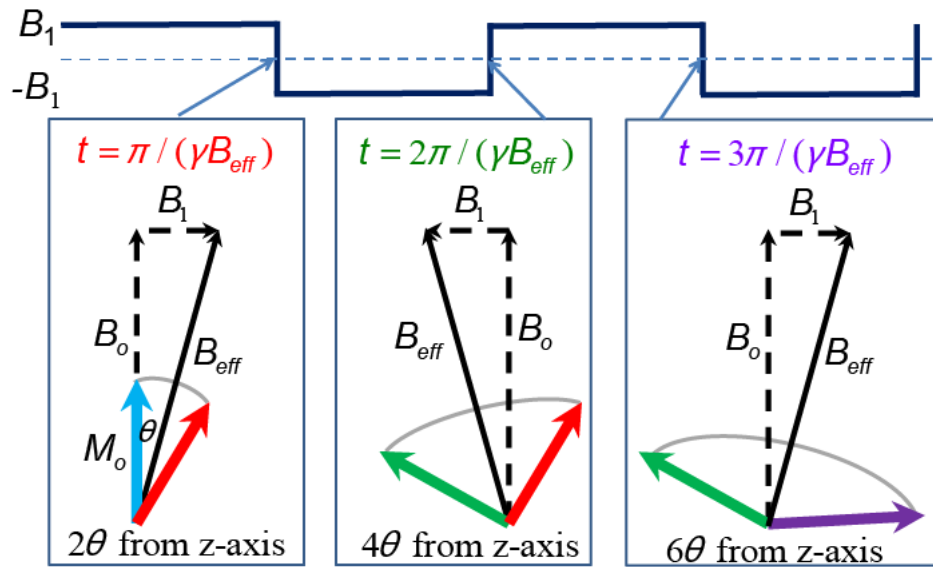
$$H = \begin{array}{c} \begin{array}{cc} |\beta\rangle & |\alpha\rangle \\ \langle\beta| & \left(\begin{array}{cc} \frac{1}{2}\gamma B_0 & \frac{1}{2}\gamma B_1 \\ \frac{1}{2}\gamma B_1 & -\frac{1}{2}\gamma B_0 \end{array} \right) \\ \langle\alpha| & \end{array} \end{array} \quad (3-3)$$

where $|\alpha\rangle$ and $|\beta\rangle$ are the eigenstates of I_z . If B_1 is constant (first panel of Figure 8(a)) the equilibrium magnetization vector M_0 precesses a maximum of $2 \tan^{-1}(B_1 / B_0)$ away from its initial position at time $\tau = \pi / (\gamma B_{eff}) = \pi / (\gamma \sqrt{B_0^2 + B_1^2})$, and further irradiation brings the magnetization back towards its initial value. However, if the phase of B_1 is reversed (from \hat{x} to $-\hat{x}$) whenever the magnetization reaches the maximum excursion (equivalent to resonant, square wave irradiation) the magnetization can be moved arbitrarily far away; the number of full cycles required to generate a complete inversion is $n = \pi / (2 \tan^{-1}(B_1 / B_0))$. Inspections of equations (38) and (39) shows that the homonuclear coupling (J) and chemical shift difference ($\Delta\omega$) in the $S-T_0$ system play the same roles as the B_0 and B_1 fields respectively in the spin-1/2 system. Moreover, in an interaction representation, the sign of the operators associated with the chemical shift difference ($I_{1z} - I_{2z}$) can be reversed by a 180° pulse that resonates with both spins. Thus a train of 180° pulses separated by delays that permit accumulation of state mixing can interconvert S and T_0 (Figure 8(b)). The “resonance condition” which maximizes the effect is then:

$$\tau = 1 / (2\sqrt{J^2 + \Delta\omega^2}) \quad (3-4)$$

and the number of 180° pulses needed to invert the population is:

$$n = \pi / (2 \times \arctan(\Delta\omega / J)) \quad (3-5)$$



(a)

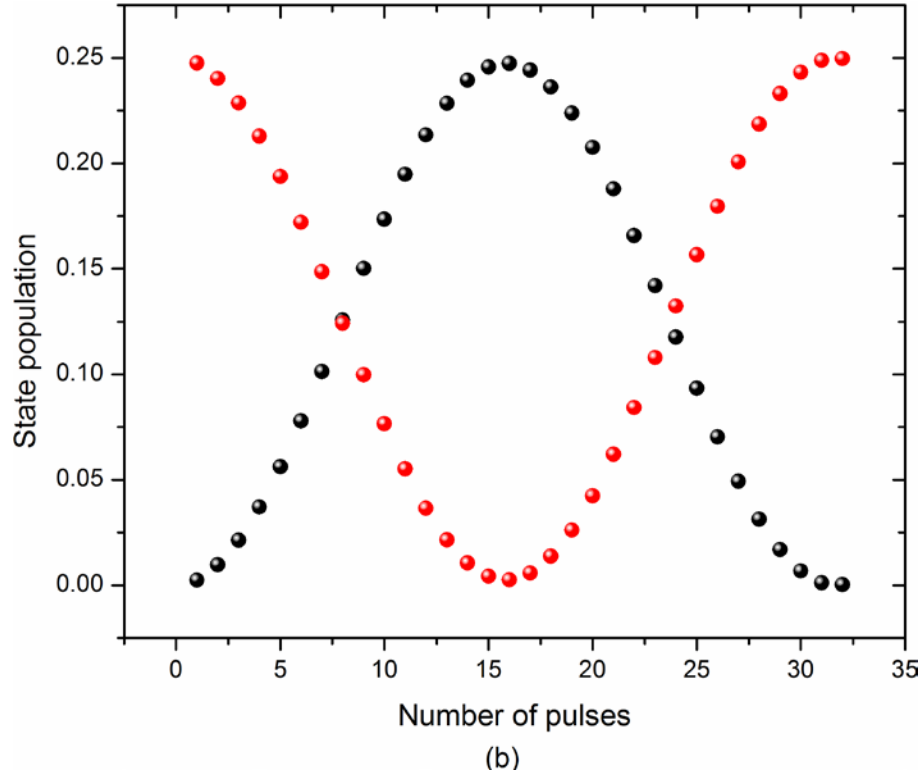


Figure 8. Analogy between (a) population inversion in a single spin $\frac{1}{2}$ two-level system and (b) population inversion in the S- T_0 two-level system. (a) Irradiation of single spin $\frac{1}{2}$ by a continuous square wave pulse with constant field strength B_1 , which is much smaller than the main field B_0 , shows that an arbitrarily small B_1 field can flip spins if the field is modulated. As discussed in text, conversion between the S and T_0 states works in exactly this same way, with the “square wave” replaced by a broadband pi pulses on both spins (b) Population interconversion between S (black) and T_0 (red) states in a near equivalent 2-spin system. The following parameters were assumed: $J = 181.8\text{Hz}$ and $\Delta\omega = 18.1\text{Hz}$. An inter pulse delay of 2.74 ms is calculated according to (40).

Detailed discussion of the sequence of events occur during the MSM sequence can be found in the literature⁶¹⁻⁶² and they are briefly outlined below. The thermal equilibrium magnetization can be represented as

$$\rho_{eq} \propto I_{1z} + I_{2z} = |T_1\rangle\langle T_1| - |T_{-1}\rangle\langle T_{-1}| \quad (3-6)$$

and the first 90°_y (Figure 7) converts it into

$$\rho_1 = I_{1x} + I_{2x} = \frac{\sqrt{2}}{2} (|T_1\rangle\langle T_0| + |T_0\rangle\langle T_1| + |T_{-1}\rangle\langle T_0| + |T_0\rangle\langle T_{-1}|) \quad (3-7)$$

Then the first 180° pulse train exchange S and T_0 , giving rise to

$$\rho_2 = i\frac{\sqrt{2}}{2} (|T_1\rangle\langle S| + |T_{-1}\rangle\langle S| - |S\rangle\langle T_1| - |S\rangle\langle T_{-1}|) \quad (3-8)$$

The subsequent 90°_x induces interconversion within the triplet state manifold and yields the zero-quantum coherence between the S and T_0 states

$$\rho_3 = |T_0\rangle\langle S| + |S\rangle\langle T_0| \quad (3-9)$$

Then a free evolution of $\tau/2$ is necessary to induce a 90° phase rotation of the coherence, leading to the following density matrix:

$$\rho_4 = -i|T_0\rangle\langle S| + i|S\rangle\langle T_0| \quad (3-10)$$

Finally, the second 180° pulse train converts the zero-quantum coherence into the population difference between the S and T_0 states

$$\rho_4 = |S\rangle\langle S| - |T_0\rangle\langle T_0| \quad (3-11)$$

This density matrix can be rewritten as

$$\rho_4 = |S\rangle\langle S| - \frac{1}{3} (|T_1\rangle\langle T_1| + |T_0\rangle\langle T_0| + |T_{-1}\rangle\langle T_{-1}|) + \frac{1}{3} (|T_1\rangle\langle T_1| - 2|T_0\rangle\langle T_0| + |T_{-1}\rangle\langle T_{-1}|) \quad (3-12)$$

Suppose the relaxation of the T_0 population is fast compared with that of the S state. In other words, the triplet states reach equilibrium before the singlet state relaxes.

Then the long-lived signal is proportional to

$$\rho_5 = |S\rangle\langle S| - \frac{1}{3} (|T_1\rangle\langle T_1| + |T_0\rangle\langle T_0| + |T_{-1}\rangle\langle T_{-1}|) \quad (3-13)$$

This can be rewritten as

$$\rho_5 = \frac{2}{3}(|S\rangle\langle S| - |T_0\rangle\langle T_0|) + \frac{1}{3}(|S\rangle\langle S| + |T_0\rangle\langle T_0| - |T_1\rangle\langle T_1| - |T_{-1}\rangle\langle T_{-1}|) \quad (3-14)$$

The first term in (3-14) is $\frac{2}{3}\rho_4$ and can be converted back to $\frac{2}{3}(I_{1x} + I_{2x})$ by the S2M sequence. Therefore, the overall efficiency of the MSM sequence is $2/3=67\%$. Namely, for a pair of near-equivalent spins, 67% of the bulk magnetization can be stored as long-lived population on the singlet state using the MSM sequence.

3.4 Accessing the long-lived states in large symmetric spin system

3.4.1 Accessing the long-lived states in an AA'XX' 4-spin system with the MSM sequence

All methods so far use chemical shift difference as the access to the long-lived singlet state. However, there is an alternative access which is revealed in our study⁵⁷. Consider a symmetric 4-spin system consisting of two distinct pairs of chemically equivalent spins. It is denoted as AA'XX', where A spins are low- γ nuclei such as ¹³C or ¹⁵N and X are usually surrounding protons; or denoted as AA'BB' where A and B are the same isotope (e.g., both protons) but have large chemical shift difference. As discussed in the previous chapter, if AA' are strongly coupled whereas the "between pair" coupling (J_{AX}) is weak, states that have a singlet component on AA' are expected to be long-lived (as shown in the literature⁴⁷, since collective long-lived states exist in such spin system which involve both pairs of spins, we generally refer to them as "long-lived states" without specifying the singlet nature). Because no chemical shift difference exists between A and A' the question arises as whether it is possible to access such long-lived

state without breaking symmetry of the spin system⁶⁰. The answer is concealed in the energy level of the spin system which has been thoroughly discussed by Pople et al⁶³⁻⁶⁵ in the 1950s. The Hamiltonian for any AA'XX'(BB') system is given as:

$$H = \omega_A (S_{1z} + S_{2z}) + \omega_X (I_{3z} + I_{4z}) + 2\pi J_{AX} (S_{1z}I_{3z} + S_{2z}I_{4z}) + 2\pi J_{AX'} (S_{2z}I_{4z} + S_{1z}I_{3z}) + 2\pi J_{AA'} \mathbf{S}_1 \mathbf{S}_2 + 2\pi J_{XX'} \mathbf{I}_3 \mathbf{I}_4 \quad (3-15)$$

where we use S to denote the low γ nucleus (¹⁵N or ¹³C) and I to denote ¹H (or ²H). ω_A and ω_X are the respective Larmor frequencies. As shown by Pople et al, this Hamiltonian can be readily block-diagonalized by choosing symmetry-adapted basis functions⁶³⁻⁶⁶ and making use of the mixing rules⁶³⁻⁶⁵ as reviewed in the following. Being a 4-spin system there are totally 16 states that can be assembled by combining the singlet state (S) and triplet states (T₊₁, T₀, T₋₁) on the AA' spin pair with the singlet and triplet states on the XX' spin pair such that for example the "singlet_A-singlet_X" state ($SS \equiv \frac{1}{2}(\alpha\beta - \beta\alpha)_A (\alpha\beta - \beta\alpha)_X$) results. The table of all 16 states can be found in ref^[65] and they can be generally categorized into "symmetric" and "asymmetric" with respect to the symmetry operation. Concretely, for the ¹⁵N¹⁵N'HH' 4-spin system in 3,6-dichloro-¹⁵N₂-pyridazine (DCP, shown in Figure 10(b)), the symmetry operation would be reflection about the symmetry plane that bisects both the ¹⁵N₂ and ¹H₂ spin pairs. Then the SS state is symmetric whereas the "singlet-triplet (ST₀)", being $\frac{1}{2}(\alpha\beta - \beta\alpha)_A (\alpha\beta + \beta\alpha)_X$, is asymmetric. The mixing rule dictates that there is no mixing between states with different symmetry; therefore there is no off-diagonal

element in the Hamiltonian that connects SS to ST_0 . In addition, mixing only occurs between states that have equal sum of proton projection number (Σm_H) and equal sum of ^{15}N projection number (Σm_N) since states with different Σm_H or Σm_N have an energy separation on the order of the Larmor frequency (MHz), and any off-diagonal J-coupling elements on the order of Hz is quenched.

Accordingly, the Hamiltonian in (3-15) can be divided into sub-matrices confined to a given symmetry containing states that are close in energy. The only two pairs of states that qualify are the SS state coupled to the T_0T_0 (“triplet-triplet”) state and the ST_0 coupled to the T_0S (“triplet-singlet”) states. The two sub-matrices are:

$$\begin{array}{ccc}
 & SS & T_0T_0 \\
 SS & -2\pi(J_{AA} + J_{XX}) & \pi\Delta J_{AX} \\
 T_0T_0 & \pi\Delta J_{AX} & 0
 \end{array} \quad (3-16)$$

$$\begin{array}{ccc}
 & ST_0 & T_0S \\
 ST_0 & -2\pi(J_{AA} - J_{XX}) & \pi\Delta J_{AX} \\
 T_0S & \pi\Delta J_{AX} & 0
 \end{array} \quad (3-17)$$

where $\Delta J_{AX} = J_{AX} - J_{AX'}$.

These two matrices are isomorphic to (3-3) and the $S-T_0$ sub-matrix in (3-2). Then the alternative access to the long-lived states emerges, namely, the difference of the two “between pair” J-couplings ($\Delta J_{AX} = J_{AX} - J_{AX'}$) which plays the same role as $\Delta\omega$ in (3-2). The operator associated with ΔJ_{AX} is $S_z I_z$, the sign of which can be reversed by a selective 180° pulse resonant with either A or X. Thus, the same MSM sequence can

access the long-lived states (SS and ST_0) with adapted resonance conditions as shown below:

$$\tau_{SS} = \frac{1}{2\sqrt{(J_{AA} + J_{XX})^2 + \Delta J_{AX}^2}} \quad (3-18)$$

$$n_{SS} = \pi / (2 \times \arctan(\Delta J_{AX} / (J_{AA} + J_{XX})))$$

$$\tau_{ST} = \frac{1}{2\sqrt{(J_{AA} - J_{XX})^2 + \Delta J_{AX}^2}} \quad (3-19)$$

$$n_{ST} = \pi / (2 \times \arctan(\Delta J_{AX} / (J_{AA} - J_{XX})))$$

Notice the resonance conditions in (3-18) and (3-19) would be equivalent when J_{XX} is zero or negligible relative to J_{AA} , a relatively common situation, as is the case in 2,3- $^{13}\text{C}_2$ -diacetylene (DIAC, Figure 10(a)). However, this is not generally valid. For instance, DCP has $J_{XX} = 9$ Hz and $J_{AA} = -24$ Hz, giving rise to different τ_{SS} and τ_{ST} . Likewise the numbers of π pulses (n_{SS} and n_{ST}) also differ. In the following we assume the common situation where $J_{XX} = 0$ for simplicity. The coherence pathway for a $^{13}\text{C}^{13}\text{CHH}$ 4-spin system during the M2S sequence resonant with ^{13}C is shown below.

The equilibrium magnetization for carbon is proportional to

$$\rho_0 \propto S_{1z} + S_{2z} \cong |T_1T_1\rangle\langle T_1T_1| + |T_1T_0\rangle\langle T_1T_0| + |T_1S\rangle\langle T_1S| + |T_1T_{-1}\rangle\langle T_1T_{-1}| - |T_{-1}T_1\rangle\langle T_{-1}T_1| - |T_{-1}T_0\rangle\langle T_{-1}T_0| - |T_{-1}S\rangle\langle T_{-1}S| - |T_{-1}T_{-1}\rangle\langle T_{-1}T_{-1}| \quad (3-20)$$

The first 90°_Y pulse converts the S_z magnetization into single quantum coherences:

$$\begin{aligned} \rho_1 \cong & \frac{\sqrt{2}}{2} (|T_1T_1\rangle\langle T_0T_1| + |T_0T_1\rangle\langle T_{-1}T_1| + |T_1T_{-1}\rangle\langle T_0T_{-1}| + |T_0T_{-1}\rangle\langle T_{-1}T_{-1}|) \\ & + \frac{\sqrt{2}}{2} (|T_1T_0\rangle\langle T_0T_0| + |T_1S\rangle\langle T_0S| + |T_0T_0\rangle\langle T_{-1}T_0| + |T_0S\rangle\langle T_{-1}S|) + C.C \end{aligned} \quad (3-21)$$

where C.C are the complex conjugates of coherences above. The subsequent multiple echo pulse generate a 180° rotation within the SS/T₀T₀ and ST₀/T₀S two-level systems, giving rise to the following coherences:

$$\begin{aligned} \rho_2 \cong & \frac{\sqrt{2}}{2} (|T_1T_1\rangle\langle T_0T_1| + |T_0T_1\rangle\langle T_{-1}T_1| + |T_1T_{-1}\rangle\langle T_0T_{-1}| + |T_0T_{-1}\rangle\langle T_{-1}T_{-1}|) \\ & + i \frac{\sqrt{2}}{2} (|T_1T_0\rangle\langle SS| + |T_1S\rangle\langle ST_0| + |SS\rangle\langle T_{-1}T_0| + |ST_0\rangle\langle T_{-1}S|) + C.C \end{aligned} \quad (3-22)$$

Notice that coherences that involve states such as T₀T₁ and T₀T₋₁ (the first bracket in equation (3-21)) are unchanged under the multiple echo sequence and therefore they are not converted into the long-lived state population by the end of the M2S. This gives rise to a 50% drop of efficiency compared against the coherence transformation in a near-equivalent 2-spin system during the M2S sequence. The unperturbed coherences are also left out in the subsequent treatment for simplicity.

$$\rho_2 \cong i \frac{\sqrt{2}}{2} (|T_1T_0\rangle\langle SS| + |T_1S\rangle\langle ST_0| + |SS\rangle\langle T_{-1}T_0| + |ST_0\rangle\langle T_{-1}S|) + C.C \quad (3-23)$$

Then the 90°_x exchanges the coherences within the ¹³C₂-triplet state manifold:

$$\rho_3 \cong |T_0T_0\rangle\langle SS| + |T_0S\rangle\langle ST_0| + |SS\rangle\langle T_0T_0| + |ST_0\rangle\langle T_0S| \quad (3-24)$$

A waiting period of $\tau/2 = 1/(4\sqrt{J_{AA}^2 + \Delta J_{AX}^2})$ is used to generate a phase shift of

the coherence within the SS/T₀T₀ and ST₀/T₀S two-level systems before another sequence

of $n/2$ 180° pulses ($n = \pi / (2 \arctan(\Delta J_{AX} / J_{AA}))$), which finally converts the coherence into population difference within the SS/T_0T_0 and ST_0/T_0S two-level systems. Accordingly, the final density matrix after the M2S sequence is:

$$\rho_4 \cong |T_0T_0\rangle\langle T_0T_0| - |SS\rangle\langle SS| + |T_0S\rangle\langle T_0S| - |ST_0\rangle\langle ST_0| \quad (3-25)$$

This parallels (3-11), yet here only 50% of the ^{13}C bulk magnetization is converted into the population difference. Accordingly, the overall efficiency of M2S on an $AA'XX'$ spin system is half of that on an AB (near equivalent 2-spin) system ($66.7\%/2=33.3\%$). However, as will be discussed later, an enormous advantage of such chemically equivalent spin systems is that the so far untapped magnetization of $X(^1\text{H})$ spins can be explored by the MSM sequence that resonates with X spins. Therefore, proton polarization can be transferred both into and out from the long-lived state population, giving rise to a significant signal enhancement compared with polarization on carbon spins.

3.4.2 Accessing the long-lived states in $AA'X_nX_n'$ spin systems ($n \geq 2$) with the MSM sequence

However, a more intriguing question would be whether this approach is generally applicable to even larger spin systems such as $AA'X_nX_n'$ with $n \geq 2$. Specifically, how to characterize the involved states with increasing n ? How do the pulse sequences access the long lived states in larger spin systems? And finally which fraction of the polarization can be stored with increasing n ? To address these questions, we

resort to the same “symmetry-reduction” technique that can readily block-diagonalize the spin-system Hamiltonian. Consider the $^{13}\text{C}^{13}\text{C}'^1\text{H}_2^1\text{H}_2'$ 6-spin system in $^{13}\text{C}_2$ -diphenyl acetylene (DPA, Figure 10(c)). The two carbons ($^{13}\text{C}_2$) and four protons ($^1\text{H}_4$) form D2h symmetry. The other protons are disregarded for they have negligible couplings to the ^{13}C spins. The J-coupling between protons on different rings is negligible, which also simplifies the derivation by synchronizing resonance conditions for multiple 2-level systems. The remaining J-coupling between the two protons on the same ring is denoted as J_{gauche} .

Then carbons and protons can be treated separately to find the symmetry-adapted basis for each species. Such states for a strongly coupled ^{13}C pair are evidently T_{+1} , T_0 and T_{-1} of symmetry A_g and S of B_{1u} . On the other hand, the four protons form 16 states in total. They are five spin-2 states of symmetry A_g , three spin-1 states of symmetry B_{1u} , three spin-1 states of symmetry B_{2u} , another three spin-1 states of symmetry B_{3g} and two spin-0 states of symmetry A_g (listed in Appendix A).

Subsequently, these 4 carbon and 16 proton states are re-combined to ultimately form the disconnected energy subspaces. The same rules applied to the 4-spin system are still valid (mixing can only occur between states with the same symmetry as well as the same total projection numbers $\sum m_H$ and $\sum m_C$). Moreover, as is observed in the AA'XX' 4-spin system, the only interaction that breaks magnetic equivalence of the A spins and therefore connects the two states in the 2-level systems (3-16 and 17) is ΔJ_{AX} .

Therefore, the goal is to find non-zero matrix element for ΔJ_{AX} in this 6-spin system.

Following the spin notation in Figure 10(c), the system Hamiltonian that is associated with C-H couplings can be written as

$$J_{CH}(I_{3z}S_{1z} + I_{4z}S_{1z} + I_{5z}S_{2z} + I_{6z}S_{2z}) + J_{CH}'(I_{3z}S_{2z} + I_{4z}S_{2z} + I_{5z}S_{1z} + I_{6z}S_{1z}) = \frac{1}{2}[\sum J_{CH}((I_{3z} + I_{4z} + I_{5z} + I_{6z})(S_{1z} + S_{2z})) + \Delta J_{CH}((I_{3z} + I_{4z} - I_{5z} - I_{6z})(S_{1z} - S_{2z}))] \quad (3-26)$$

We can write $H_{\Delta J} = \frac{1}{2}\Delta J_{CH}((I_{3z} + I_{4z} - I_{5z} - I_{6z})(S_{1z} - S_{2z}))$ and matrix element for $H_{\Delta J}$ is given by

$$\langle \psi | H_{\Delta J} | \psi' \rangle = \frac{1}{2}\Delta J_{CH} \langle \psi_H | (I_{3z} + I_{4z} - I_{5z} - I_{6z}) | \psi_H' \rangle \langle \psi_C | (S_{1z} - S_{2z}) | \psi_C' \rangle \quad (3-28)$$

Two additional rules can be noted to readily trace down states that are interconnected by ΔJ_{CH} . First, matrix elements of $(S_{1z} - S_{2z})$ vanish unless the carbon spins are pointed in opposite directions, therefore the $^{13}\text{C}_2$ state can only be S or T₀. In addition, the total projection number of the four protons ($\sum m_H$), which decomposes into $m_{12} + m_{34}$ (total projection of spin 1 and 2 and of spin 3 and 4), can only take values of ± 1 (where either m_{12} or m_{34} is ± 1 and the other is zero) or 0 (when $m_{12} = \pm 1$ and $m_{34} = \mp 1$).

Thus, we have found 20 combinations of proton (10 out of total 16 proton states) and carbon states (S and T₀) that satisfy all rules stated above. They form ten isolated 2-level systems (Table 3). The Hamiltonian matrices of two such systems are shown below:

$$\begin{array}{ccc}
A_g & \frac{1}{\sqrt{2}}(T_{-1}T_0 + T_0T_{-1})T_0 & \frac{1}{\sqrt{2}}(T_{-1}T_0 - T_0T_{-1})S \\
\frac{1}{\sqrt{2}}(T_{-1}T_0 + T_0T_{-1})T_0 & \frac{\pi}{2}J_{CC} + \pi J_{gauche} & -\pi\Delta J_{CH} \\
\frac{1}{\sqrt{2}}(T_{-1}T_0 - T_0T_{-1})S & -\pi\Delta J_{CH} & -\frac{3\pi}{2}J_{CC} + \pi J_{gauche}
\end{array} \quad (3-29)$$

$$\begin{array}{ccc}
B_{lu} & \frac{1}{\sqrt{2}}(T_{-1}T_{+1} + T_{+1}T_{-1})S & \frac{1}{\sqrt{2}}(T_{-1}T_{+1} - T_{+1}T_{-1})T \\
\frac{1}{\sqrt{2}}(T_{-1}T_{+1} + T_{+1}T_{-1})S & -\frac{3\pi}{2}J_{CC} + \pi J_{gauche} & -2\pi\Delta J_{CH} \\
\frac{1}{\sqrt{2}}(T_{-1}T_{+1} - T_{+1}T_{-1})T & -2\pi\Delta J_{CH} & \frac{\pi}{2}J_{CC} + \pi J_{gauche}
\end{array} \quad (3-30)$$

Expectedly, (3-29) is essentially identical to (3-16) and (3-17) (they only differ by a multiple of the identity matrix given $J_{xx} = 0$ in (3-16 and 17), also note J_{gauche} has no effect since it identically shifts the two states in (3-29)). Population difference is generated between the two states by the end of M2S and the state $\frac{1}{\sqrt{2}}(T_{-1}T_0 - T_0T_{-1})S$, which has the carbon singlet component, is source of the long-lived signal. According to Table 3, there are totally eight such 2-level systems (16 states) in which all states have $\sum m_H = \pm 1$. They can be accessed by the MSM sequence using the same resonance condition shown in Eqs. (3-18 and 19). Thus, a quarter of the total spin states (16 out of 64) in the 6-spin system are used to store bulk magnetization, the same as in a 4-spin system (4 out of totally 16 states). Therefore, the maximum fraction of carbon magnetization being stored as the long-lived state population is expected to be the same as that in a 4-spin system (33% stored as the difference of singlet population and “average” triplet population). Interestingly, there exists a second type of 2-level sub-space (3-30) in the 6-spin system, where the two states with $\sum m_H = 0$ are interconnected by double the frequency (off-diagonal element is $2 \times \pi\Delta J_{CH}$). These 2-level systems (two such systems in Table 3) are

more clearly revealed with the detected signal from an alternative pulse sequence that will be discussed in the following section.

Extension to 8-spin systems is made through numerical simulation where a $^{13}\text{C}^{13}\text{C}'\text{H}_3\text{H}_3'$ spin configuration is assumed which is readily encountered in real molecules (for example, from two methyl groups). Expectedly, as long as the J_{HH} across the two methyl groups is negligible, the fraction of total carbon magnetization being stored as long-lived signal is the same (33%). Another interesting generalization is to spin systems that contain deuterium, consider for example, per-deuterated-2,3- $^{13}\text{C}_2$ -diacetylene which forms an AA'QQ' 4-spin system. A single spin-1 behaves similarly to a pair of strongly coupled spin-1/2. Therefore, the long-lived states in the AA'QQ' 4-spin system can be readily derived. Assuming zero J-coupling between the two deuterons, similar 2-level systems that contain the long-lived states are listed in Table 4 with deuteron states represented by the letters P, Z, M (Plus, Zero and Minus) which correspond to the deuteron projection number, $m_d = +1, 0, -1$. Similar to the 6-spin system in DPA, the two 2-level systems with $\Sigma m_d = 0$ have an off-diagonal element as $2 \times \pi \Delta J_{CD}$ and therefore evolve at twice the rate of the 2-level systems with $\Sigma m_d = \pm 1$.

Table 3. 2-level systems in $^{13}\text{C}^{13}\text{C}'^1\text{H}_2^1\text{H}_2'$ 6-spin system of DPA.

Γ	$\sum m_H$	2-level systems	
A_g	+1	$\frac{1}{\sqrt{2}}(T_{+1}T_0 + T_0T_{+1})T_0$	$\frac{1}{\sqrt{2}}(T_{+1}T_0 - T_0T_{+1})S$
	0	$\frac{1}{\sqrt{2}}(T_{-1}T_{+1} + T_{+1}T_{-1})T_0$	$\frac{1}{\sqrt{2}}(T_{-1}T_{+1} - T_{+1}T_{-1})S$
	-1	$\frac{1}{\sqrt{2}}(T_{-1}T_0 + T_0T_{-1})T_0$	$\frac{1}{\sqrt{2}}(T_{-1}T_0 - T_0T_{-1})S$
B_{1u}	+1	$\frac{1}{\sqrt{2}}(T_{+1}T_0 - T_0T_{+1})T_0$	$\frac{1}{\sqrt{2}}(T_{+1}T_0 + T_0T_{+1})S$
	0	$\frac{1}{\sqrt{2}}(T_{-1}T_{+1} - T_{+1}T_{-1})T_0$	$\frac{1}{\sqrt{2}}(T_{-1}T_{+1} + T_{+1}T_{-1})S$
	-1	$\frac{1}{\sqrt{2}}(T_{-1}T_0 - T_0T_{-1})T_0$	$\frac{1}{\sqrt{2}}(T_{-1}T_0 + T_0T_{-1})S$
B_{2u}	+1	$\frac{1}{\sqrt{2}}(T_{+1}S + ST_{+1})T_0$	$\frac{1}{\sqrt{2}}(T_{+1}S - ST_{+1})S$
	-1	$\frac{1}{\sqrt{2}}(T_{-1}S + ST_{-1})T_0$	$\frac{1}{\sqrt{2}}(T_{-1}S - ST_{-1})S$
B_{3g}	+1	$\frac{1}{\sqrt{2}}(T_{+1}S - ST_{+1})T_0$	$\frac{1}{\sqrt{2}}(T_{+1}S + ST_{+1})S$
	-1	$\frac{1}{\sqrt{2}}(T_{-1}S - ST_{-1})T_0$	$\frac{1}{\sqrt{2}}(T_{-1}S + ST_{-1})S$

State functions are written as combination of proton and ^{13}C states, e.g., $\frac{1}{\sqrt{2}}(T_{+1}T_0 + T_0T_{+1})T_0$ has $^1\text{H}_4$ in state $\frac{1}{\sqrt{2}}|T_{+1}T_0 + T_0T_{+1}\rangle$ and $^{13}\text{C}_2$ in state $|T_0\rangle$. The irreducible representations (Γ) of each 2-level system as well as their sum of proton projection number ($\sum m_H$) are also provided. Long-lived signal comes from the states with $^{13}\text{C}_2$ spins in the singlet, which are shown in the right column. All eight 2-level systems that have $\sum m_H = \pm 1$ are accessed by the MSM sequence with regular resonance condition.

Table 4. 2-level systems in the AA'QQ' 4-spin system

Γ	$\sum m_D$	2-level systems	
A_g	+1	$\frac{1}{\sqrt{2}}(PZ + ZP)T_0$	$\frac{1}{\sqrt{2}}(PZ - ZP)S$
	0	$\frac{1}{\sqrt{2}}(MP + PM)T_0$	$\frac{1}{\sqrt{2}}(MP - PM)S$
	-1	$\frac{1}{\sqrt{2}}(MZ + ZM)T_0$	$\frac{1}{\sqrt{2}}(MZ - ZM)S$
A_u	+1	$\frac{1}{\sqrt{2}}(PZ + ZP)S$	$\frac{1}{\sqrt{2}}(PZ - ZP)T_0$
	0	$\frac{1}{\sqrt{2}}(MP + PM)S$	$\frac{1}{\sqrt{2}}(MP - PM)T_0$
	-1	$\frac{1}{\sqrt{2}}(MZ + ZM)S$	$\frac{1}{\sqrt{2}}(MZ - ZM)T_0$

Deuteron (Q) states are written in the Zeeman states and ^{13}C (A) spins are in the S-T states. One such spin system is contained in per-deuterated-2,3- $^{13}\text{C}_2$ -diacetylene, which has a C_i symmetry and the state space is divided according to their symmetry property with respect to the inversion center (A_g : symmetric; A_u : antisymmetric).

3.5 SLIC: An alternative sequence to access the long-lived states

3.5.1 Using SLIC to access the singlet state between near-equivalent spins

The most critical drawback of the MSM sequence is still high power dissipation due to the multiple echo sequence, although it is already mitigated compared with the spin-lock approach introduced in section 3.1. The same calculation⁵⁹ shows the MSM sequence with a typical set of parameters can exceed the allowable energy deposition by 20 times, which dampens the enthusiasm for the long-lived states in clinical imaging community. In 2014, Devience et al⁶⁷ introduced a new approach for pumping singlet states in near equivalent spins, which they called spin-lock induced crossing. As opposed to the basic structure of the MSM (multiple echo pulse sequences), the SLIC sequence (Figure 9) uses much weaker CW irradiation (up to 200 Hz versus kHz hard

pulses in MSM) to drive the transition to the singlet state, which drastically decreases power dissipation. This was a significant step forward and we showed later that with adapted parameters SLIC also works with chemically equivalent spin systems⁵⁹.

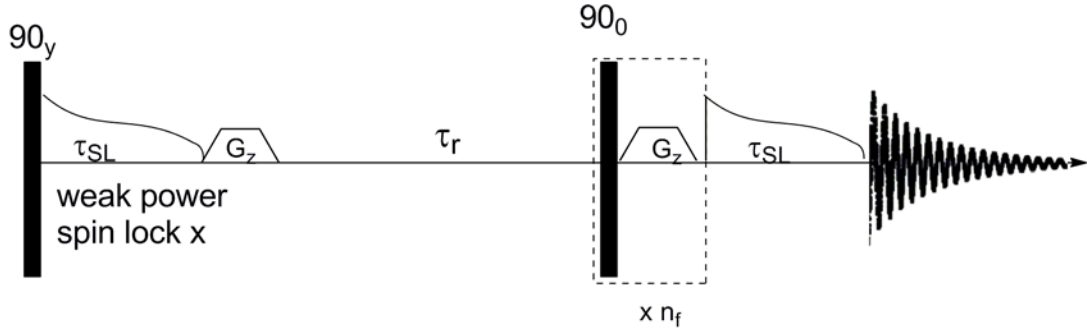


Figure 9. The SLIC sequence. A hard 90° pulse with y-phase, followed by continuous wave (CW) irradiation with x-phase and specified amplitude of ω_1 to match the in-pair J-coupling creating population of the singlet state. For a constant amplitude CW irradiation as introduced in Ref[67], an irradiation period of $\tau_{SL}=1/(\square 2\Delta\gamma)$ creates the maximum singlet state population. The population is then readout after a storage time, τ_r , by another period (τ_{SL}) of CW irradiation with the appropriate amplitude. The phase of the second CW-pulse is not critical but has been implemented with the same phase for simplicity. For singlet state lifetime measurement at thermal equilibrium, we implemented gradient- 90°_x combinations as filter to suppress residual thermal signal decaying by T_1 , which was not used in the original paper (ref[65]). n_f (up to 15) denotes the number of 90°_x - G_z repetition unit it requires to completely destroy the thermal contribution.

To describe the spin dynamics of a near equivalent 2-spin system during the SLIC sequence, the eigenbasis of $I_{1x} + I_{2x}$, denoted as the X basis, is the most convenient basis.

$$\begin{aligned}
 |S\rangle &\equiv \frac{1}{\sqrt{2}}|\alpha\beta - \beta\alpha\rangle, |X_{+1}\rangle \equiv \frac{1}{2}|\alpha\alpha + \alpha\beta + \beta\alpha + \beta\beta\rangle, \\
 |X_0\rangle &\equiv \frac{1}{\sqrt{2}}|\alpha\alpha - \beta\beta\rangle, |X_{-1}\rangle \equiv \frac{1}{2}|\alpha\alpha + \beta\beta - \alpha\beta - \beta\alpha\rangle.
 \end{aligned}
 \tag{3-31}$$

The first 90°_y tips down the bulk magnetization to transverse x polarization.

Expressed in the X basis the density matrix is

$$\rho \cong I_{1x} + I_{2x} \propto \begin{bmatrix} S & X_{+1} & X_0 & X_{-1} \\ S & 0 & 0 & 0 \\ X_{+1} & 0 & 1 & 0 \\ X_0 & 0 & 0 & 0 \\ X_{-1} & 0 & 0 & -1 \end{bmatrix} \quad (3-32)$$

The subsequent CW duration modifies the system Hamiltonian into

$$H = H_0 + H_1 = \begin{matrix} & X_{-1} & X_{+1} & X_0 & S \\ X_{-1} & \frac{\pi J}{2} - \omega_1 & 0 & -\frac{\Sigma\omega}{2\sqrt{2}} & -\frac{\Delta\omega}{2\sqrt{2}} \\ X_{+1} & 0 & \frac{\pi J}{2} + \omega_1 & -\frac{\Sigma\omega}{2\sqrt{2}} & \frac{\Delta\omega}{2\sqrt{2}} \\ X_0 & -\frac{\Sigma\omega}{2\sqrt{2}} & -\frac{\Sigma\omega}{2\sqrt{2}} & \frac{\pi J}{2} & 0 \\ S & -\frac{\Delta\omega}{2\sqrt{2}} & \frac{\Delta\omega}{2\sqrt{2}} & 0 & -\frac{3\pi J}{2} \end{matrix} \quad (3-33)$$

where H_0 is defined in equation (1-1), $\Delta\omega$ and $\Sigma\omega$ are the difference and sum of Larmor frequencies of the two spins. $H_1 = \omega_1(I_{1x} + I_{2x})$ is the Hamiltonian for the irradiation pulse field that resonates at $\frac{\Sigma\omega}{2}$ with phase x and a nutation frequency of ω_1 . It is convenient to assume a rotating frame at the average Larmor frequency of the two spins ($\Sigma\omega = 0$) and to identically shift all diagonal elements by $\frac{-\pi J}{2}$. Then (3-33) is simplified to

$$H = \begin{matrix} & S & X_{+1} & X_0 & X_{-1} \\ S & -2\pi J & \frac{\Delta\omega}{2\sqrt{2}} & 0 & -\frac{\Delta\omega}{2\sqrt{2}} \\ X_{+1} & \frac{\Delta\omega}{2\sqrt{2}} & \omega_1 & 0 & 0 \\ X_0 & 0 & 0 & 0 & 0 \\ X_{-1} & -\frac{\Delta\omega}{2\sqrt{2}} & 0 & 0 & -\omega_1 \end{matrix} \quad (3-34)$$

The fundamental mechanism of the SLIC sequence is now revealed by (3-34). A RF field with amplitude $\omega_1 = 2\pi J$ equalizes energy of the states S and X_{-1} , allowing the much smaller off-diagonal element, $-\frac{\Delta\omega}{2\sqrt{2}}$ to induce polarization oscillation between the two states with a period of $\frac{2\sqrt{2}\pi}{\Delta\omega}$ or $\frac{\sqrt{2}}{\Delta\nu}$ ($\Delta\nu = \Delta\omega/2\pi$). The exact inversion of the polarization occurs at half of that period ($\tau_{SL} = 1/(\sqrt{2}\Delta\nu)$, Figure 9) and the population of X_{-1} is quantitatively transferred to S . The density matrix considering only the S and X_{-1} states, under the SLIC irradiation develops as

$$\rho(t) = e^{-iHt} \rho e^{iHt} \approx \begin{array}{cc} & \begin{array}{c} S \\ X_{-1} \end{array} \\ \begin{array}{c} S \\ X_{-1} \end{array} & \begin{array}{cc} & X_{-1} \\ -\frac{1}{2} + \frac{1}{2} \cos(\pi\Delta\nu t) & -\frac{i}{2} \sin(\pi\Delta\nu t) \\ \frac{i}{2} \sin(\pi\Delta\nu t) & -\frac{1}{2} - \frac{1}{2} \cos(\pi\Delta\nu t) \end{array} \end{array} \quad (3-35)$$

The following properties of SLIC are also noteworthy: First, if the CW field is implemented 180° out of phase ($\omega_1 = -2\pi J$), the singlet state would be put to resonance with X_{+1} and the same amount of population would still be induced by the end of the same irradiation period. Second, unlike the M2S sequence which equally populates S and T_0 states (equation (3-11)), SLIC populates the two states unequally, it can be readily shown⁶⁷ by numerical simulation that the same amount of S population is generated by the first half of SLIC as compared to M2S while T_0 is only half as populated as S . Nevertheless, this does not diminish the ultimate long-lived signal (compare 1st and 3rd rows of Table 5) which arises from the difference between the singlet state population and the “averaged” triplet state population (equation (3-13)).

3.5.2 Using SLIC to access the long-lived states in chemically equivalent spin systems

Similarly, we showed later⁵⁹ that SLIC can also induce long-lived state population in chemically equivalent spin systems using the “between-pair” J-coupling difference (ΔJ_{AX}) as the driving force. Again, we use the $^{13}\text{C}^{13}\text{CHH}$ 4-spin system in DIAC (Figure 10(a)) as an example. To facilitate the derivation, again we use the X basis for the irradiated spin (^{13}C) and the S-T basis for ^1H . The relevant Hamiltonian submatrices that contain states SS and ST_0 are

$$\begin{array}{ccccc}
 & SS & X_{+1}T_0 & X_0T_0 & X_{-1}T_0 \\
 SS & -2\pi(J_{CC} + J_{HH}) & \frac{\pi\Delta J_{CH}}{\sqrt{2}} & 0 & -\frac{\pi\Delta J_{CH}}{\sqrt{2}} \\
 X_{+1}T_0 & \frac{\pi\Delta J_{CH}}{\sqrt{2}} & \omega_1 & 0 & 0 \\
 X_0T_0 & 0 & 0 & 0 & 0 \\
 X_{-1}T_0 & -\frac{\pi\Delta J_{CH}}{\sqrt{2}} & 0 & 0 & -\omega_1
 \end{array} \quad (3-36)$$

and

$$\begin{array}{ccccc}
 & ST_0 & X_{+1}S & X_0S & X_{-1}S \\
 ST_0 & -2\pi J_{CC} & \frac{\pi\Delta J_{CH}}{\sqrt{2}} & 0 & -\frac{\pi\Delta J_{CH}}{\sqrt{2}} \\
 X_{+1}S & \frac{\pi\Delta J_{CH}}{\sqrt{2}} & -2\pi J_{HH} + \omega_1 & 0 & 0 \\
 X_0S & 0 & 0 & -2\pi J_{HH} & 0 \\
 X_{-1}S & -\frac{\pi\Delta J_{CH}}{\sqrt{2}} & 0 & 0 & -2\pi J_{HH} - \omega_1
 \end{array} \quad (3-37)$$

It is evident that (3-36) and (3-37) are isomorphic to (3-34) and the resonance conditions are $\omega_1 = 2\pi(J_{CC} + J_{HH})$ and $\omega_1 = 2\pi(J_{CC} - J_{HH})$, respectively, which are the same if $J_{HH} = 0$. Moreover, the maximum population on SS and ST_0 is induced at the same time ($\tau_{SL} = 1/(\sqrt{2}\Delta J_{CH})$). Similarly, extension can be made to larger spin system

such as the 6-spin system in DPA (Figure 10(c)). The long-lived states are still those with a “singlet” carbon component (e.g., $\frac{1}{\sqrt{2}}S(T_{-1}T_0 - T_0T_{-1})$), listed in the last column of Table 3) and each of them is connected to three carbon “X” states to form a 4-level system.

Two such sub-matrices of the system Hamiltonian are:

$$\begin{array}{ccccc}
 A_g & \frac{1}{\sqrt{2}}X_1(T_{-1}T_0 + T_0T_{-1}) & \frac{1}{\sqrt{2}}X_0(T_{-1}T_0 + T_0T_{-1}) & \frac{1}{\sqrt{2}}X_{-1}(T_{-1}T_0 + T_0T_{-1}) & \frac{1}{\sqrt{2}}S(T_{-1}T_0 - T_0T_{-1}) \\
 \frac{1}{\sqrt{2}}X_1(T_{-1}T_0 + T_0T_{-1}) & \pi J_{gauche} + \omega_1 & -\frac{\pi}{\sqrt{2}}\Sigma J_{CH} & 0 & -\frac{\pi}{\sqrt{2}}\Delta J_{CH} \\
 \frac{1}{\sqrt{2}}X_0(T_{-1}T_0 + T_0T_{-1}) & -\frac{\pi}{\sqrt{2}}\Sigma J_{CH} & \pi J_{gauche} & -\frac{\pi}{\sqrt{2}}\Sigma J_{CH} & 0 \\
 \frac{1}{\sqrt{2}}X_{-1}(T_{-1}T_0 + T_0T_{-1}) & 0 & -\frac{\pi}{\sqrt{2}}\Sigma J_{CH} & \pi J_{gauche} - \omega_1 & \frac{\pi}{\sqrt{2}}\Delta J_{CH} \\
 \frac{1}{\sqrt{2}}S(T_{-1}T_0 - T_0T_{-1}) & -\frac{\pi}{\sqrt{2}}\Delta J_{CH} & 0 & \frac{\pi}{\sqrt{2}}\Delta J_{CH} & -2\pi J_{CC} + \pi J_{gauche}
 \end{array} \tag{3-38}$$

$$\begin{array}{ccccc}
 B_{lu} & \frac{1}{\sqrt{2}}X_1(T_{-1}T_{+1} - T_{+1}T_{-1}) & \frac{1}{\sqrt{2}}X_0(T_{-1}T_{+1} - T_{+1}T_{-1}) & \frac{1}{\sqrt{2}}X_{-1}(T_{-1}T_{+1} - T_{+1}T_{-1}) & \frac{1}{\sqrt{2}}S(T_{-1}T_{+1} + T_{+1}T_{-1}) \\
 \frac{1}{\sqrt{2}}X_1(T_{-1}T_{+1} - T_{+1}T_{-1}) & \pi J_{gauche} + \omega_1 & 0 & 0 & -\sqrt{2}\pi\Delta J_{CH} \\
 \frac{1}{\sqrt{2}}X_0(T_{-1}T_{+1} - T_{+1}T_{-1}) & 0 & \pi J_{gauche} & 0 & 0 \\
 \frac{1}{\sqrt{2}}X_{-1}(T_{-1}T_{+1} - T_{+1}T_{-1}) & 0 & 0 & \pi J_{gauche} - \omega_1 & \sqrt{2}\pi\Delta J_{CH} \\
 \frac{1}{\sqrt{2}}S(T_{-1}T_{+1} + T_{+1}T_{-1}) & -\sqrt{2}\pi\Delta J_{CH} & 0 & \sqrt{2}\pi\Delta J_{CH} & -2\pi J_{CC} + \pi J_{gauche}
 \end{array} \tag{3-39}$$

In (3-38) states $\frac{1}{\sqrt{2}}X_{-1}(T_{-1}T_0 + T_0T_{-1})$ and $\frac{1}{\sqrt{2}}S(T_{-1}T_0 - T_0T_{-1})$ are connected by $\frac{\pi}{\sqrt{2}}\Delta J_{CH}$ while $\frac{1}{\sqrt{2}}X_{-1}(T_{-1}T_{+1} - T_{+1}T_{-1})$ and $\frac{1}{\sqrt{2}}S(T_{-1}T_{+1} + T_{+1}T_{-1})$ in (3-39) are connected by $\sqrt{2}\pi\Delta J_{CH}$. Therefore, when $\omega_1 = 2\pi J_{CC}$, the polarization oscillation in (3-39) is twice as fast as that in (3-38), which echoes the observation in (3-29 and 30). Then, for any given τ_{SL} , population induced on the carbon singlet is a combined effect of both resonance conditions, which can be approximated as:

$$\rho(\tau_{SL}) \propto 8 \times \left(-\frac{1}{2} + \frac{1}{2} \cos(\sqrt{2}\pi\Delta J \tau_{SL}) \right) + 2 \times \left(-\frac{1}{2} + \frac{1}{2} \cos(2\sqrt{2}\pi\Delta J \tau_{SL}) \right) \quad (3-40)$$

The factors of 8 and 2 come from the fact that eight long-lived states are connected by $\frac{\pi}{\sqrt{2}}\Delta J_{CH}$ and two are connected by $\sqrt{2}\pi\Delta J_{CH}$. This “double frequency” oscillation is readily distinguished from the single sinusoidal oscillation (3-40) observed in a near-equivalent spin pair and an AA'XX' 4-spin system. This is verified in Figure 11, where the carbon singlet state population after cw irradiation with varied duration is simulated and also measured experimentally.

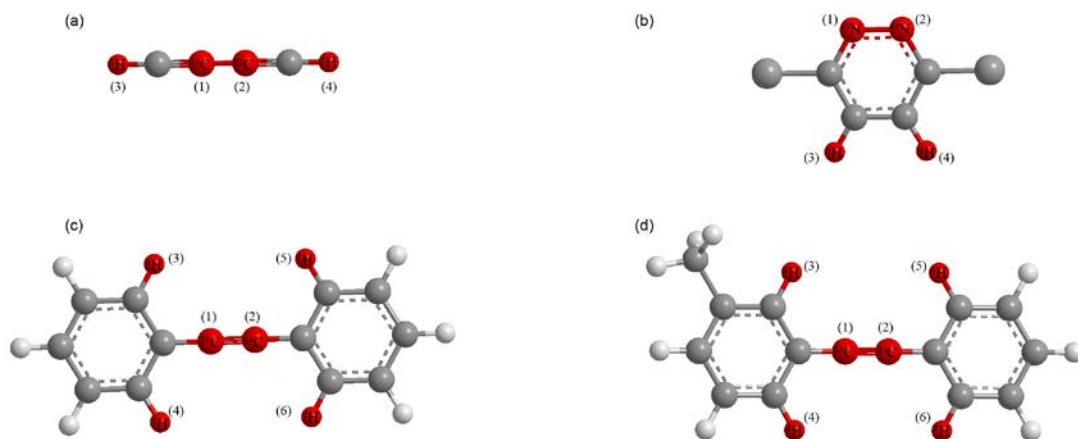


Figure 10. Spin systems discussed in chapters 3 and 4. (a) 2,3- $^{13}\text{C}_2$ -diacetylene (DIAC) contains a $\text{CC}'\text{HH}'$ 4-spin system ($\text{D}_{\infty\text{h}}$ point group). (b) 3,6-dichloro- $^{15}\text{N}_2$ -pyridazine (DCP) contains a $^{15}\text{N}^{15}\text{N}'\text{HH}'$ 4-spin system ($\text{C}_{2\text{v}}$ point group). (c) $^{13}\text{C}_2$ -diphenyl acetylene (DPA) contains a $^{13}\text{C}^{13}\text{C}'\text{H}_2\text{H}_2'$ 6-spin system ($\text{D}_{2\text{h}}$ pointgroup), the remaining protons are not considered for they have minimum couplings to the central $^{13}\text{C}_2$ spin pair. (d) $^{13}\text{C}_2$ -meta methyl diphenyl acetylene (mDPA) also has a $^{13}\text{C}^{13}\text{C}'\text{H}_2\text{H}_2'$ 6-spin system, however, a significant chemical shift difference between the two ^{13}C spins ($\Delta\omega = 0.56$ ppm) breaks the symmetry of the spin system.

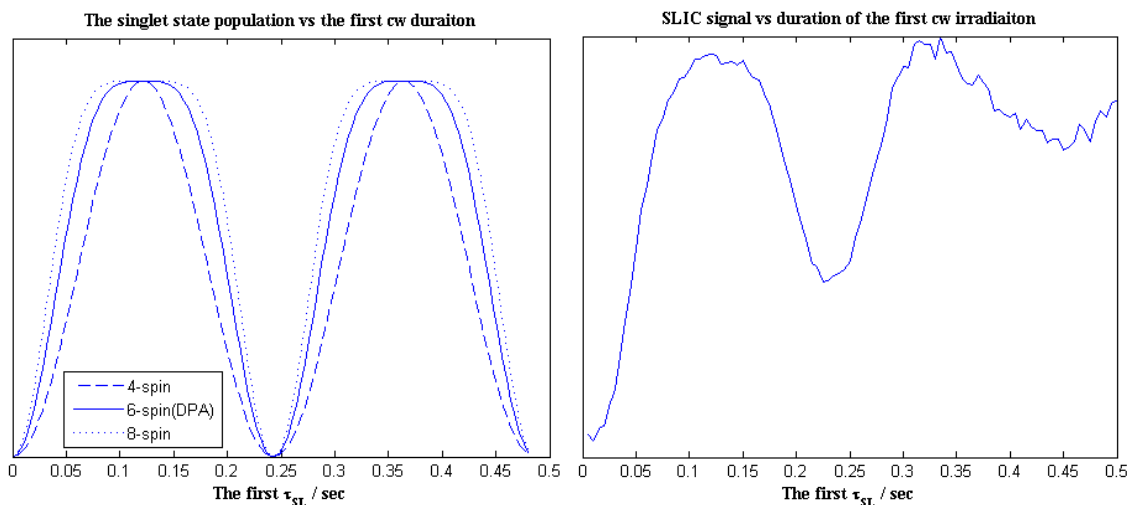


Figure 11. (left) Simulated singlet state population after the first cw irradiation in SLIC with varied duration (τ_{SL}). $^{13}\text{C}_2$ -singlet state population in DPA (6-spin, $J_{CC} = 181.8$ Hz and $\Delta J_{CH} = 5.82$ Hz), in a pseudo 4-spin and a pseudo 8-spin system with the same J-couplings are simulated. The singlet state population in the 4-spin system has a single-frequency sinusoidal dependence on τ_{SL} while both 6-spin and 8-spin systems have multi-frequency sinusoidal dependence on τ_{SL} , indicated by the “flattened” profile. (right) Experimental evaluation of SLIC signal measured with DPA. The first τ_{SL} varies but the second is fixed. The first period of oscillation has flattened profile that agrees with the simulation. Field inhomogeneities and T_2 relaxation quickly damp out the oscillation in experiment while these factors are not included in the simulation.

3.5.3 Composite and adiabatic SLIC sequence to compensate for field inhomogeneities

Although the SLIC sequence with simple “square-wave” irradiation pulses has largely reduced the power deposition, its practical application faces another severe challenge. Because the resonance condition requires the nutation frequency ω_1 to exactly match the scalar coupling (J_{CC}), SLIC sequence is very sensitive to field inhomogeneity and RF pulse off-resonance effect. Conventional approach to enhance robustness against these effects is to use composite pulse⁶⁸⁻⁶⁹ or adiabatic shaped pulse⁷⁰⁻⁷². However,

existing shapes and solutions fail completely in this problem. For example, the conventional composite pulse $90_x 180_y 90_x$ normally generates population inversion which is less sensitive to RF or static inhomogeneity than the inversion from a simple 180_x pulse. However, as Figure 12 (d-f) shows, this approach fails completely for the SLIC sequence. The reason is that in the conventional two-level problem, the irradiating field creates an off-diagonal term with phase dictated by the pulse phase, and the diagonal term is the offset from exact resonance; but for SLIC, the irradiating field produces a diagonal term in the relevant basis, and the off-diagonal term is either the coupling or chemical shift difference between the two spins. Furthermore, phase shifting the RF changes the system drastically: Consider the effective Hamiltonian in (3-36), a 180° phase shift couples SS to $X_{+1}T_0$ instead of $X_{-1}T_0$, and a 90° phase shift couples $X_{+1}T_0$, X_0T_0 and $X_{-1}T_0$. Thus, adapting shaped or composite pulses to this problem requires some transformations. The coupling ΔJ_{CH} is constant and real, so the simplest solutions start with constant-amplitude pulses of constant phase. First we will consider the composite pulse case, and rewrite the composite pulse $90_x 180_y 90_x$ in an equivalent form, $90_x 90_z 180_x 270_z 90_x$. The simplest is to turn off the irradiation field, in which case the states are separated by $2\pi(J_{CC} + J_{HH})$ and free evolution is equivalent to a $-z$ rotation. Thus, a free evolution of $\pi(J_{CC} + J_{HH})/2$ gives the 90° rotation, and evolution of $3\pi(J_{CC} + J_{HH})/2$ gives a 270° rotation. The sequence 90_x (free evolution, $\pi(J_{CC} + J_{HH})/2$) 180_x (free evolution, $3\pi(J_{CC} + J_{HH})/2$) 90_x , shown in Figure 12(g-i), generates improvement. The

B_1 -amplitude resonance condition is now 10 Hz wide at FWHM (full width at half maximum, Figure 3h), roughly doubled from 5 Hz for the basic SLIC, and the bottom of the resonance appears much flatter. The RF-offset resonance condition is now 84 Hz wide (Fig. 3i), an improvement of 35% over basic SLIC. This sequence works well because the total needed phase shift is small.

Next, we focus our attention on the implementation of adiabatic SLIC pulses for the singlet-triplet interconversion. An intuitive approach to adiabatic pulses is to switch into the frequency-modulated rotating frame introduced in Ref. [73]. That paper designs the modulated inversion pulse, with constant amplitude and a tangent frequency sweep $\Omega(t)$. This pulse gives an identical trajectory on resonance to the sech-amplitude, tanh-frequency swept adiabatic pulses commonly used in imaging⁷³⁻⁷⁵ and demonstrated with ultrafast lasers⁷⁶⁻⁷⁷. As described above, the intuitive approach for the Hamiltonian in (3-36) is to consider ω_1 and $2\pi(J_{CC} + J_{HH})$ terms as z-terms and the ΔJ_{CH} terms as x-terms, as opposed to the classical perspective used in Ref. [73] where B_1 amplitudes correspond to x-terms and frequency offsets correspond to z-terms. We obtain for an adiabatic SLIC pulse:

$$\begin{aligned} \omega_1(t) &= \omega_c - A \cos \gamma \tan(t A \sin \gamma) \\ -\pi / (2A \sin \gamma) &< t < \pi / (2A \sin \gamma), \end{aligned} \tag{3-41}$$

where γ is an adjustable parameter ($\gamma=\pi/2$ recovers the conventional unmodulated pulse) The classical “frequency modulation” is now performed by changing the

amplitude of irradiation. Additionally, the center of the pulse has amplitude of $\omega_c = 2\pi(J_{CC} + J_{HH})$ as opposed to zero-frequency offset on resonance. (Note that as defined in (3-41) $\omega_1 = \omega_c$ at $t=0$. When implemented experimentally the time for the shape hence runs from $-t_d$ to t_d where $t_d < \pi / (2A \sin \gamma)$ and needs to be chosen based on performance of the pulse. Here $t_d = 0.25$ s was chosen)

Figure 12(j-l) displays the effects of this type of pulse, simulated for $A=10.6$ Hz and $\gamma=0.455$. The sensitivity to B_1 inhomogeneity is drastically reduced as demonstrated by the much broader B_1 -amplitude resonance condition of Figure 12(k). For the chosen parameters the FWHM is increased by a factor 6 to 30 Hz as compared to the basic SLIC experiment. Also, the FWHM for the frequency offset is more than doubled to 140 Hz as compared to 62 Hz for the basic SLIC pulse making the adiabatic much less sensitive to off-resonance effects as well. □

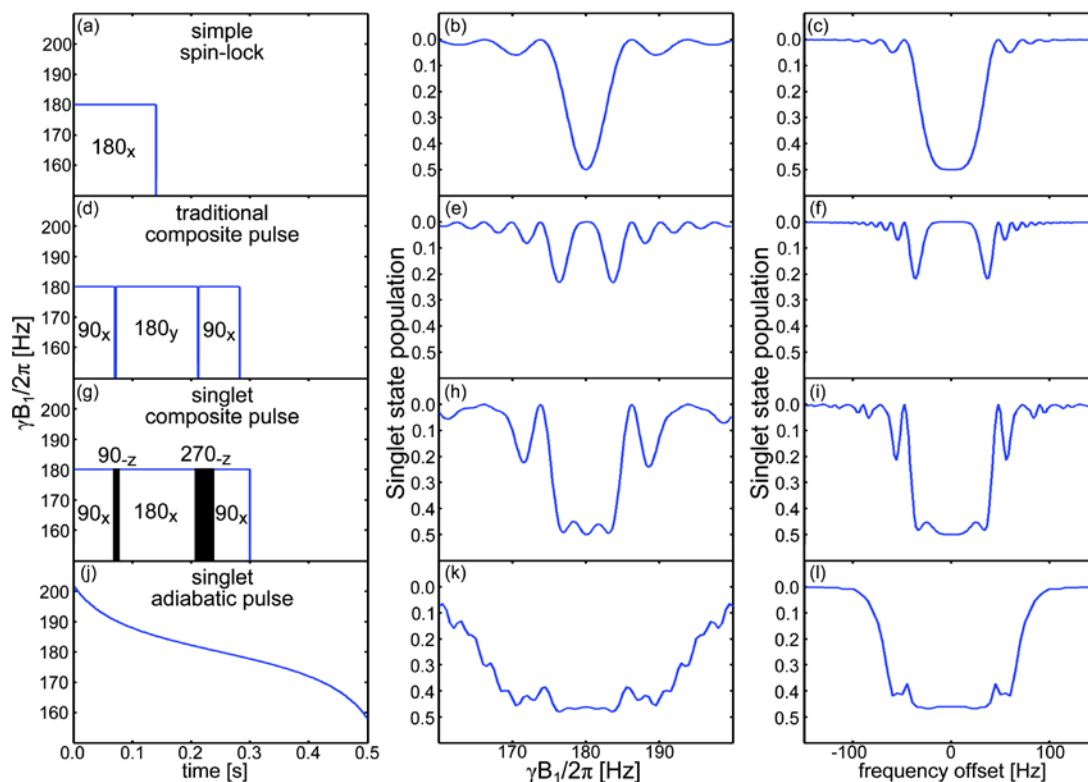


Figure 12. From Ref. [59], simulations of several SLIC pulse shapes examining their B_1 amplitude sensitivity and frequency offset sensitivity. (Top row a-c) shows the behavior for the simple spin-lock with 5Hz bandwidth in the B_1 amplitude and 62 Hz bandwidth in the RF-offset. The traditional composite pulse (second row d-f) completely fails to produce the singlet state whereas singlet composite pulse (third row g-i) improves both the B_1 -amplitude resonance condition bandwidth (10Hz) as well as the RF-offset resonance bandwidth (84Hz),. Further improvement is provided by the singlet adiabatic pulse (bottom row j-l), yielding a B_1 -resonance bandwidth of 30Hz and RF-offset bandwidth of 140Hz (For details of the simulations see next chapter).

3.6 Polarization transfer from $X(^1\text{H})$ spins to the long-lived states

As discussed in the previous section, the overall efficiency of driving $A(^{13}\text{C})$ spin polarization into the long-lived states with an $AA'X_{(n)}X_{(n)'}'$ spin system is only half of that with an AB spin system. This is essentially because only half of the $X(^1\text{H})$ states (S and T_0 for M2S, S and X_{-1} for SLIC) participate in the transitions which are perturbed by

either sequence. However, for chemically equivalent spin systems such as $^{13}\text{C}^{13}\text{C}'\text{HH}'$, another opportunity arises. Proton magnetization can be transferred into the long-lived carbon singlet state by applying the first half of either sequence on proton⁷⁸. Consider for example, the M2S sequence, a coherence pathway similar to that detailed in (3-20 to 3-25) can guide the same fraction of proton magnetization (33% of total proton magnetization) into the long-lived states SS and ST₀. At thermal equilibrium, this gives rise to 4 times ($\gamma_H / \gamma_{^{13}\text{C}} \approx 4$, the ratio of gyromagnetic ratios of proton versus carbon) larger long-lived state population than the same fraction of carbon magnetization can produce. A more intriguing possibility is to apply the complete sequence on proton, namely proton preparation and proton detection. Then proton magnetization can obtain an even more dramatic lifetime extension than carbon through being stored as long-lived state population⁷⁸. Because this sequence only uses proton pulses, it can be readily applied to standard clinical scanners that are not equipped with heteronuclear detection. More importantly, the SNR improvement of proton detection over $^{13}\text{C}/^{15}\text{N}$ detection is dramatic. Concretely, Tables 5 and 6 compare numerical calculations of the relative SNR for a variety of different spin architectures and pulse sequences intended to access long-lived states, assumed to have constant molar concentration. The couplings reflect the structure of DPA ($J_{AA}=181.8$ Hz, $J_{XX}=0$, $\Delta J_{AX}=5.82$ Hz), with the number of couplings reduced or enlarged for the 4- or 8-spin cases respectively. The first table assumes thermal polarization and coil-dominated noise⁷⁹⁻⁸⁰ ($SNR \propto \gamma_{prep} \gamma_{det}^{7/4} B_0^{7/4}$), as would be

appropriate in an NMR spectrometer used for detecting and screening such states. The “¹H only” pulse sequences imply proton preparation-proton detection; the signal in the second and fourth rows would be 1/4 as large for carbon preparation-proton detection. Table 6 assumes constant fractional hyperpolarization (e.g. 10% for proton or 10% for carbon) and body-dominated noise⁷⁹⁻⁸⁰ ($SNR \propto \gamma_{det}$), as would be appropriate in a high-field MR imager with a hyperpolarizer; as the gyromagnetic ratio of the initial magnetization does not enter into the calculation, the “¹H only” pulse sequences in rows two and four would give the same signal for proton preparation-proton detection or for carbon preparation-proton detection. In all cases, the signal in long-lived states is “filtered” by artificially adding a sequence of 90° pulses and crusher gradients (Figure 7 and 9); thus it is assumed that only states that are singlet in carbon produce significantly extended lifetimes, and other states relax quickly back to equilibrium.

The trends in Tables 5 and 6 are straightforward to understand. We begin with the carbon-only sequences. Expectedly, in the AA'XX' spin system, the maximum signal from either carbon MSM or carbon SLIC is half the signal from the AB spin system. As shown earlier, for MSM or SLIC with the optimal timing, half of the sixteen proton states in AA'X₂X₂' also participate in the sequence, and numerical calculations verify that this trend continues with AA'X₃X₃'.

The proton-only sequences have substantial gains from the higher gyromagnetic ratio (which is more important under the assumptions of Table 5 than Table 6) and by the assumption of constant molar concentration (so $AA'X_3X_3'$ has three times the starting magnetization of $AA'XX'$). For $AA'XX'$, MSM outperforms SLIC because MSM populates two long lived states (SS and ST_0 , where as usual the first letter signifies the carbon component) whereas SLIC starting from protons populates SS and T_0S . The second state is assumed to equilibrate rapidly with T_1S and $T_{-1}S$, reducing the observable population differences. The net effect is a reduction in long-lived state production by one-third. It is interesting to note that as n increases in the $AA'X_{(n)}X_{(n)}'$, the overall efficiency of the proton sequences rises somewhat for MSM and falls somewhat for SLIC, although it stayed constant for the carbon sequences. In fact, increasing n decreases the fraction of states which can participate in the proton sequences, but the decrease is slower than linear for MSM (and thus overcome by the magnetization, which is proportional to n) and faster than linear for SLIC. We should note that the differences between A and X nucleus detection would be even more dramatic for ^{15}N ($\gamma_H / \gamma_{^{15}\text{N}} \approx 10$) instead of ^{13}C ; the numbers in the second and fourth rows of Table 5 would then be multiplied by 12.4, the numbers in the first and third rows of Table 6 would be multiplied by 2.5.

Table 5. SNR comparison between “proton-only” and “carbon-only” pulse sequences assuming thermal polarization and coil-dominated noise

	AB	AA'XX'	AA'X ₂ X ₂ '	AA'X ₃ X ₃ '
MSM (¹³ C only)	1	0.5	0.5	0.5
MSM (¹ H only)	----	22	23	35
SLIC (¹³ C only)	1	0.5	0.5	0.5
SLIC (¹ H only)	----	16	14	10

Table 6. SNR comparison between “proton-only” and “carbon-only” pulse sequences assuming constant fractional hyperpolarization and body-dominated noise

	AB	AA'XX'	AA'X ₂ X ₂ '	AA'X ₃ X ₃ '
MSM (¹³ C only)	1	0.5	0.5	0.5
MSM (¹ H only)	----	2.0	2.1	3.1
SLIC (¹³ C only)	1	0.5	0.5	0.5
SLIC (¹ H only)	----	1.4	1.1	0.9

It's worth noting that discussions throughout this thesis focus on AA'X_(n)X_{(n)'} heteronuclear spin systems. However, as mentioned earlier, long-lived states in homonuclear spin systems such as AA'B_(n)B_{(n)'} can also be accessed with the same pulse sequence techniques as long as the pulse (the 180° pulses in MSM or the cw irradiation in SLIC) can be selectively put in resonance with either A or B spins. For example, the

SLIC sequence is intrinsically “frequency-selective” due to its high sensitivity to field inhomogeneity and pulse off-resonance effect and its selectivity can be further tuned with pulse-shaping techniques. As aside, an approach very closely related to the SLIC sequence, named “Level Anti-Crossing (LAC)” was proposed by Spiess et al⁸¹⁻⁸³ to access the singlet state in such homonuclear chemically equivalent spin system. Interestingly, with homonuclear spin systems where J_{AB} is comparable to $\omega_A - \omega_B$, the “secular approximation” about J_{AB} cannot be assumed and the complete J-coupling Hamiltonian ($J_{AB}(I_A \cdot I_B)$) must be used. Consequently, more states are connected by ΔJ_{AB} . Indeed, the LAC sequence access long-lived states such as ST_{-1} and ST_{+1} rather than ST_0 or SS states in the AA'BB' spin system.

To summarize, in this chapter, we have introduced multiple methods to store bulk magnetization as long-lived state population in various spin systems. The adiabatic SLIC sequence is particularly promising for HP-MRS application given its robustness against field inhomogeneity and low power deposition. On the other hand, the difference between the near equivalent 2-spin system and the chemically equivalent multi-spin system has been thoroughly discussed. Although larger fraction of magnetization can be stored as long-lived polarization in the former spin system, the latter has largely overcome this disadvantage by using proton magnetization for signal preparation and detection. An important result is presented in chapter 4 and 5 showing the generality of this polarization transfer technique. The proton preparation-proton

detection strategy is still effective even when symmetry of the spin system is broken by a considerable chemical shift difference between the AA' spins. This is demonstrated with meta-methyl-DPA (Figure 10(d)). Chapter 4 focuses on numerical simulations for predicting relaxation lifetime and optimizing pulse sequence for efficient polarization interconversion. Chapter 5 presents all experiments conducted on molecules that support such long-lived states.

4. Spin dynamics simulation with SPINACH

This chapter discusses the application of the SPINACH simulation package⁸⁴ to the study of long-lived nuclear spin states. Developed by Kuprov et al⁸⁴ SPINACH is a fast open-source spin dynamics simulation library written in MatLab that supports NMR, EPR, DNP, MAS PHIP, optimal control and other forms of magnetic resonance spectroscopy. It is universally acknowledged that a brute force Liouville space simulation for a general spin system with more than 20 spins is not practically feasible because the conventional algorithms scale exponentially with the system size. The primary objective of the SPINACH package is to generate accurate low-dimensional matrix representations for Liouville space operators and state vectors for large spin systems⁸⁴ so that most liquid-state NMR experiments (with relaxation, chemical kinetics and symmetry) can be simulated for 40+ spins with relative ease. Therefore, SPINACH is well-suited for our work to predict relaxation lifetimes of the long-lived state (section 4.1) and to optimize pulse sequence conditions for maximum polarization interconversion efficiency (section 4.2).

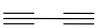

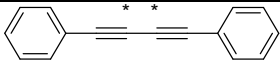
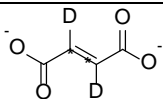
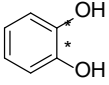
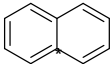
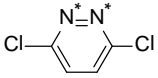
4.1 Relaxation lifetime prediction with SPINACH

As discussed in Chapter 2, the two predominant relaxation mechanisms for small molecules in non-viscous liquid are intra-molecular dipole-dipole (DD) and chemical shift anisotropy (CSA)-driven relaxation. Other mechanisms such as spin-rotation, inter-molecular DD can also be critical in some cases yet, they are difficult to simulate without

a rigorous molecular dynamics (MD) treatment. The current version of SPINACH includes intra-molecular DD and CSA-driven relaxation; relaxation via J-coupling to quadrupolar nuclei; and relaxation due to cross-correlations between these mechanisms. To calculate individual relaxation rates, properties such as the geometry, the chemical shielding tensors and the J-coupling networks of spin systems are predicted with quantum mechanics method provided by Gaussian09 simulation package⁸⁵. Specifically, Density Functional Theory (DFT) are used to optimize the geometries with the B3LYP⁸⁶ functional combined with 6-311++g** basis set. Based on the optimized structure, chemical shielding tensors and J-couplings are calculated with the “SPINSPIN” and “GIAO” key words⁸⁷⁻⁹⁰. With these inputs, relaxation lifetimes of molecules are predicted under the assumption of rigid molecules that undergo isotropic diffusion (therefore, an isotropic rotational correlation time is assumed and can be calibrated against the measured T_1 if it is available), which is admittedly oversimplified for many molecules, e.g., molecules that go through anisotropic rotational diffusion and molecules that have fast internal structure vibration and rotation. These features are being added to SPINACH package. However, Table 7 only includes structures that are relatively rigid and a universal correlation time of 100 ps is assumed. Therefore prediction is based on a single structure optimized at the lowest energy and the included relaxation mechanisms are intramolecular DD, CSA and cross-correlation thereof. The goal is to compare the incoherent relaxation rates for longitudinal magnetization ($R_1 = T_1^{-1}$) versus the long-

lived state population (R_s). They are extracted as matrix elements from the relaxation superoperator (\hat{R}). Notably, R_s does not correspond to the measured long-lived state lifetime reported in chapter 5 since no relaxation due to coherent evolution is considered. Examples of such simulation that takes into account both the incoherent and coherent relaxation during the pulse sequence is shown in Table 8.

Table 7. Comparison of simulated T_1 relaxation rate and the incoherent relaxation rate for the singlet state across either two ^{13}C or two ^{15}N spins in rigid structures.

	Structure	Spin system	R_1 (s^{-1}) at 8.45 T	R_1/R_s at 8.45 T	R_1 (s^{-1}) at 1 T	R_1/R_s at 1 T
Diacetylene		CC'HH'	0.31	58	0.08	15
Diphenyl-acetylene		CC'H ₂ H ₂ '	0.33	107	0.13	44
Diphenyl-diacetylene		CC'H ₂ H ₂ '	0.16	348	0.06	119
Deuterated fumarate		CC'DD'	0.32	70	0.20	45
Catechol		CC'HH'	0.15	11	0.08	10
Naphthalene		CC'H ₂ H ₂ '	0.31	20	0.11	7
Dichloro-pyridazine		NN'HH'	0.29	34	0.006	35

The $^{13}\text{C}_2$ or $^{15}\text{N}_2$ spin pairs are labeled with asterisk. B3LYP/6-311++G** functional/basis combination is used to optimize the geometries. Single point energy calculation is

conducted with the same functional/basis combination and with the “GIAO” and “SPINSPIN” keywords. Then the calculated CSA tensor and molecular structure are used in SPINACH to predict the relaxation caused by CSA and intra molecular DD interaction. The rotational correlation time for all molecules is assumed to be 100 ps.

Notably, the first four molecules in Table 7 (from diacetylene to fumarate) all exhibit an evident decrease of the R_1/R_s ratio going from 8.45 T to 1T. As discussed in chapter 2, the intra molecular DD relaxation is assumed field independent in the extreme narrowing regime while the CSA-driven relaxation has a quadratic dependence on B_0 . Therefore, it can be inferred that the singlet state on these molecules is largely protected from CSA-driven relaxation while the longitudinal magnetization is not, giving rise to the clear field dependence of the R_1/R_s ratio. In particular, acetylenic carbons (in the first three molecules) with linear sp hybridization results in identical CSA tensors on the two carbons when they are related by inversion symmetry, which diminish any CSA contribution to the singlet state relaxation, leading to extraordinary lifetime extensions compared with T_1 . Similar effect is observed for singlet states across an inversion center⁴⁷, such as that in deuterated fumarate. To the contrary, the R_1/R_s ratio for the rest molecules have no such strong field dependence, indicating uncorrelated CSA tensors on the two spins which leads to notable CSA-driven relaxation on the singlet state. Moreover, for catechol and naphthalene, the singlet state relaxation due to the DD interaction from surround protons (those that are only two bonds away) is also significant, leading to only a moderate lifetime extension in both field strengths.

To compare with the experimental measurements, simulations that include both coherent evolution and incoherent relaxation during the used pulse sequence are imperative. They are shown in Table 8 for DPA (Figure 10(c)) and meta-methyl DPA (mDPA, Figure 10(d)) together with the measured T_1 and T_s at two varied field strengths with the MSM sequence. The meta-methyl group induces a 0.56 ppm (=51 Hz at 8.45 T and 99 Hz at 16.44 T) chemical shift difference between the two ^{13}C spins. Such a big $\Delta\omega$ (compared with a J_{CC} of 182 Hz) makes a spin-locking field during the relaxation delay imperative at 16.44 T and optional at 8.45 T to make the singlet state on mDPA long-lived. In contrast, coherent mixing induced by ΔJ_{CH} (= 5 Hz) is trivial therefore a proton decoupling pulse makes negligible difference in the singlet lifetime (compare row 1 and 2 in the DPA measurements). For all simulations in Table 8, a correlation time of 25 ps is assumed for both DPA and mDPA to match the measured T_1 and the agreement between the measured and simulated T_s is acceptable.

Table 8. Summary of measured and simulated T_1 and singlet relaxation time (T_s) at varied field strengths for DPA and mDPA.

Sample	Field strength B_0 / T	Theoretical T_1 / s	Theoretical T_s /s	Experimental T_1 /s	Experimental T_s /s
$^{13}\text{C}_2$ - mDPA	8.45	12.1	145 ± 1.5	$12.0 \pm 0.2,$	144.8 ± 1.0
	8.45 with spin locking	---	257 ± 1.5	---	225.9 ± 5.4
	16.44 with spin locking	4.6	246.5 ± 0.2	4.3	213 ± 1
$^{13}\text{C}_2$ - DPA	8.45	12.2	274.7 ± 6.1	$13.9 \pm 0.2,$	288.4 ± 3.7
	8.45 with ^1H decoupling	---	274.7 ± 6.1	---	267.1 ± 5.4
	16.44	4.6	252.0 ± 5.0	4.9	244.7 ± 1.4

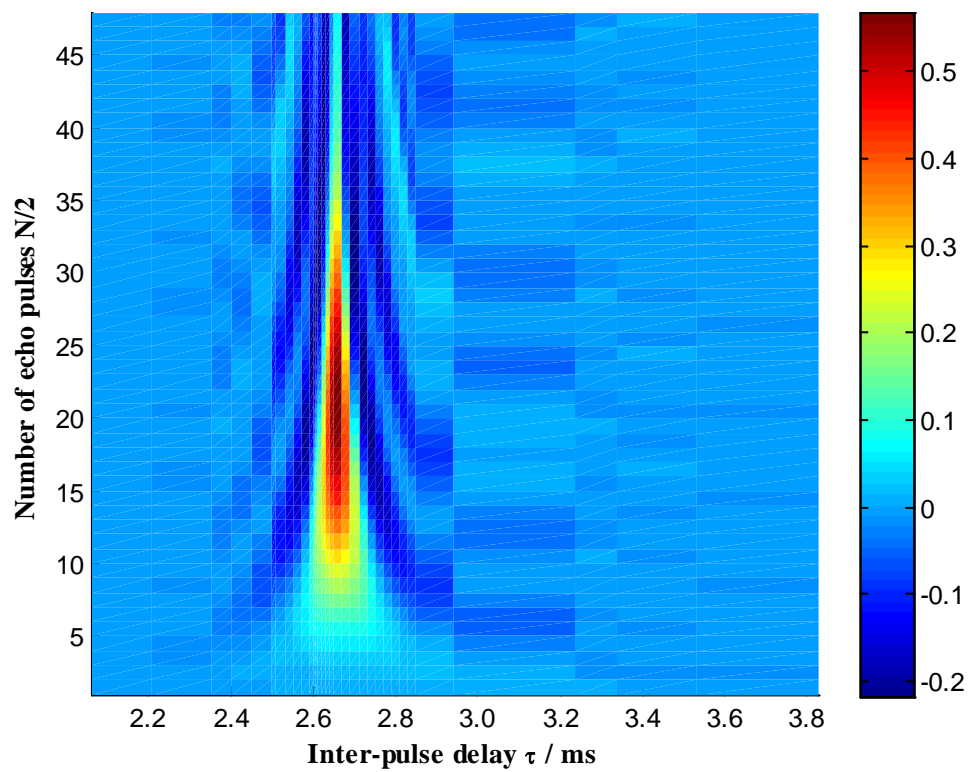
4.2 Numerical optimization of adiabatic SLIC pulse using SPINACH

4.2.1 Resonance conditions of proton-only M2S and SLIC sequences for mDPA

As discussed in the previous section, a considerable chemical shift difference ($\Delta\omega = 0.56$ ppm, 50 Hz at 8.45 T, ten times larger than $\Delta J_{CH} \approx 5$ Hz, yet smaller than $J_{CC}=182$ Hz) between the two carbons breaks symmetry of mDPA (Figure 10(d)). If all protons are neglected then a near-equivalent 2-spin system is recovered. Therefore, the resonance condition shown by Taylor and Levitt⁶² can be applied to interconvert carbon magnetization and the singlet state polarization. Nonetheless, we show here that the strategy discussed in section 3.6, namely using ΔJ_{CH} to interconvert proton polarization and the long-lived state population can still be achieved.

To find the correct condition we resort to numerical optimization with SPINACH because the same symmetry reduction technique used in section 3.6 cannot be applied. Figure 13(a) shows such an optimization to the M2S sequence where all pulses are implemented on proton. Population difference between the $^{13}\text{C}_2$ S and T_0 states is evaluated against number of 180° pulses ($n/2$) and inter-pulse delay (τ). The maximum conversion occurs around $\frac{n}{2} = \pi / (4 \times \arctan(\Delta J_{CH} / J_{CC}))$ and $\tau = 1 / (2\sqrt{J_{CC}^2 + \Delta\omega^2})$. Similarly, we can also find the adjusted resonance condition for the SLIC sequence to transfer polarization from proton to $^{13}\text{C}_2$ -singlet state. As shown in Figure 13(b), maximum conversion occurs at $\omega_1 \approx 2\pi \times 188.7$ Hz, which is slightly larger than J_{CC} , and continuous wave (cw) duration $\tau \approx 98$ ms, which is slightly shorter than the cw duration for DPA ($d_{SL} = 1 / (\sqrt{2}\Delta J_{CH}) \approx 140$ ms) but is still much longer than that for the near-equivalent resonance condition ($d_{SL} = 1 / (\sqrt{2}\Delta\omega) \approx 14$ ms). Experimental demonstration of the corresponding resonance conditions are shown in chapter 5.

(a) Population difference between S and T_0 after $M2S(^1H)$



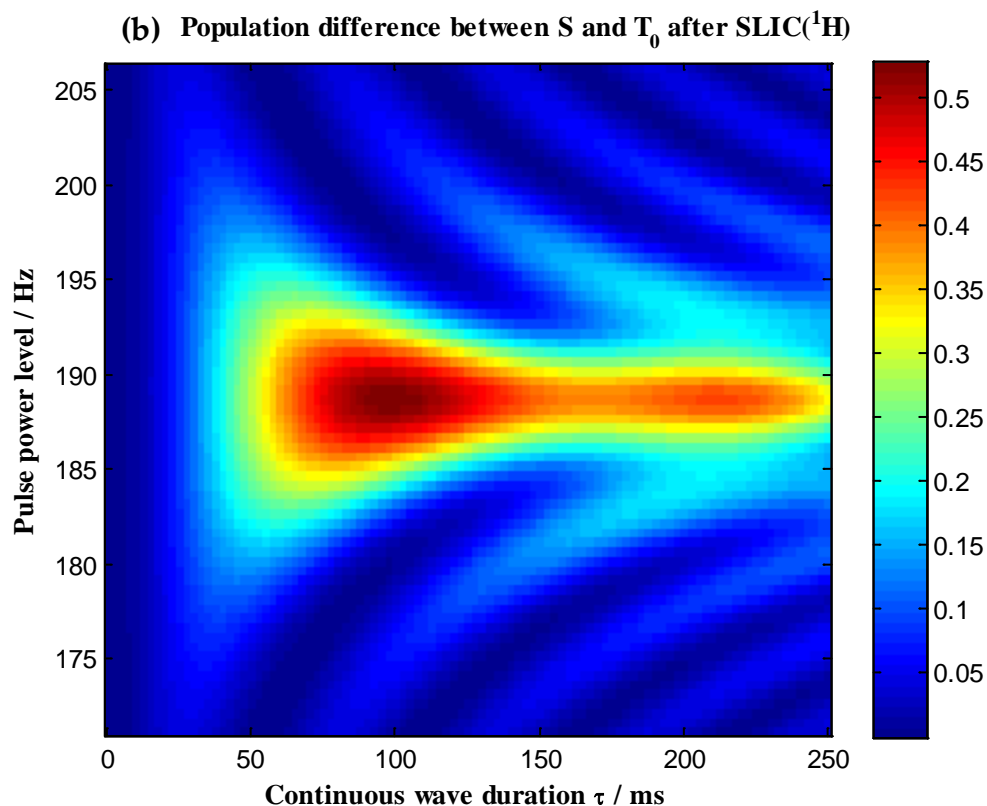


Figure 13. (a) Population difference between the $^{13}\text{C}_2\text{-S}$ and T_0 states in mDPA after the M2S(^1H) sequence with various number (N) of 180° pulses and inter-pulse delay (τ). The vertical axis is the number ($N/2$) of 180° pulses in the second multiple echo sequence block in M2S. (b) Population difference between the $^{13}\text{C}_2\text{-S}$ and T_0 states in mDPA after the first half of the SLIC(^1H) sequence with different irradiation power (in units of Hz) and duration (τ).

4.2.2 Optimization of adiabatic shape for SLIC sequence with SPINACH

The adiabatic shape pulse proposed in section 3.5 can be improved by machine learning algorithm known in magnetic resonance society as optimal control theory⁹¹⁻⁹³ if all parameters (J-couplings, chemical shifts and resonance offsets of pulses) are given. Figure 14 shows such an example of waveform optimization for adiabatic SLIC. The goal is to optimize the pulse shape for accessing the singlet state with carbon magnetization

in mDPA. The adiabatic cw pulse designed for DPA (3-41) with shortened duration (from 500 ms to 70 ms) is used as the initial input, considering the much faster conversion induced by $\Delta\omega(=51$ Hz at 8.45 T) in mDPA than $\Delta J_{CH}(=5$ Hz) in DPA. Then SPINACH invokes the gradient ascent pulse engineering (GRAPE)⁹² algorithm to optimize the waveform with the target function being the population difference between the carbon S and T_0 states. The irradiation power is bounded between 162 and 202 Hz (centered around $J_{CC}(=182$ Hz)) so that any excursion outside this range is penalized. The optimization stops when the maximum cycle is reached or further improvement is below a certain threshold. As shown in Figure 14(b), the improvement over the original adiabatic shape with respect to the bandwidth against RF offset is moderate. The optimization can certainly continue with exploration of larger parameter space yet it is worth noting that optimal control is only effective when the complete Hamiltonian of the spin system is known. For example, waveform generated by the same procedure optimized against the $^{13}\text{C}^{13}\text{C}'$ 2-spin system in mDPA is likely to fail when evaluated against the $^{13}\text{C}^{13}\text{C}'\text{H}_2\text{H}_2'$ 6-spin system. Because most spin systems in this thesis are fairly strongly-coupled and approximations are always made to their Hamiltonian; the application of such procedure might be of limited use.

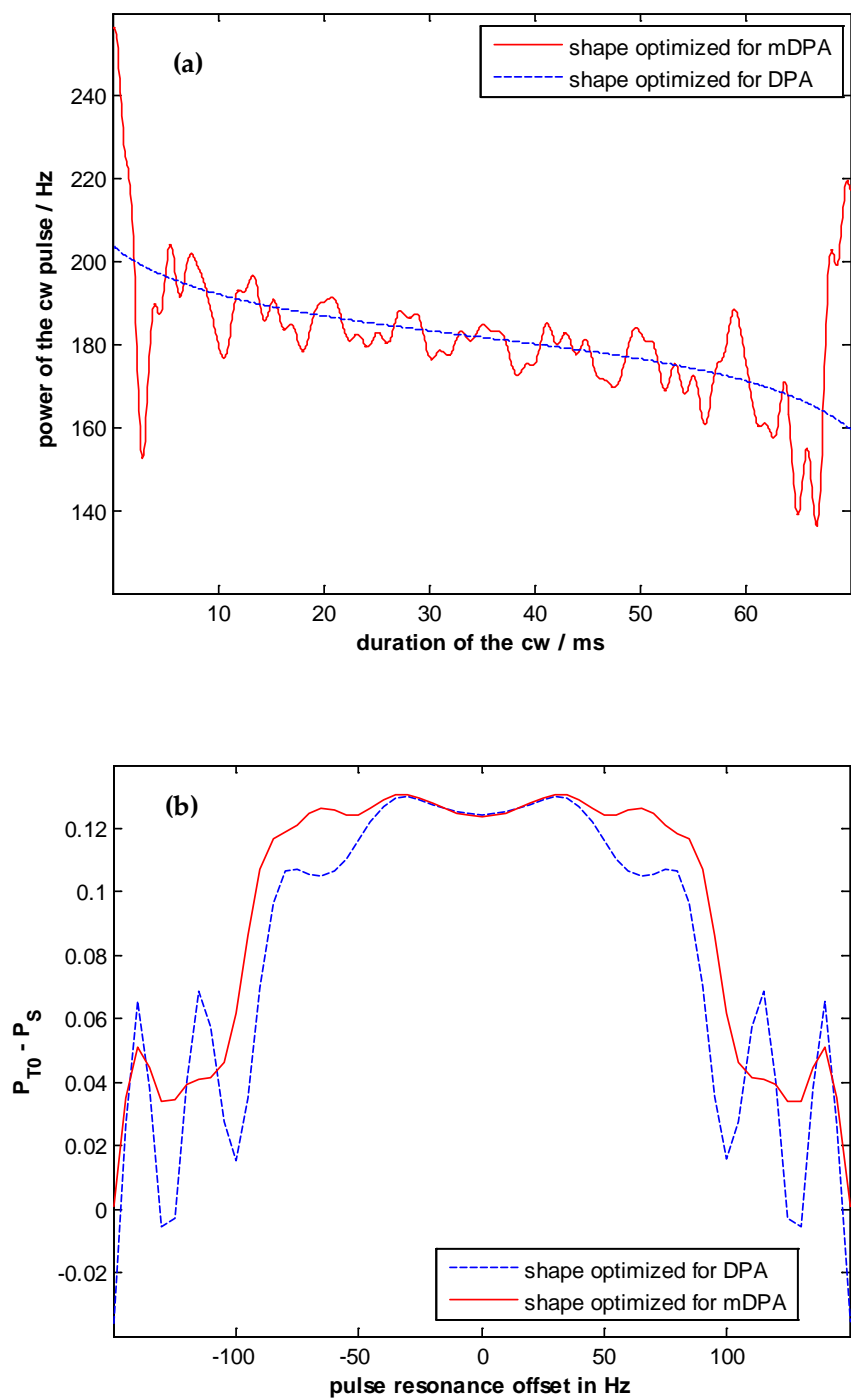


Figure 14. Adiabatic waveforms for the SLIC sequence with mDPA. (a) Shapes of the adiabatic pulses. The initial shape (dashed blue) is the adiabatic pulse designed for

DPA (section 3.5.3) but with shortened duration (70ms). The optimized shape (red) has the same duration but high frequency modulations based on the initial shape. (b) Performance of the two shapes against RF off-resonance effect; moderate improvement is provided by the shape generated from the GRAPE algorithm.

5. Experimental demonstration of long-lived nuclear spin states

This chapter summarizes all experiments on the long-lived nuclear spin states. Each subsequent section covers one particular spin system and generalization to other biological relevant molecules is discussed in the last section.

5.1 $^{13}\text{C}_2$ -diethyl oxalate (DEO)

In $^{13}\text{C}_2$ -diethyl oxalate (DEO, Figure 15(a)), there is an $\text{AA}'\text{X}_2\text{X}_2'$ 6-spin system including the two ^{13}C spins and four methylene protons (methyl protons are neglected for they have trivial coupling to the ^{13}C spins). Recall the coherence pathways detailed in chapter 3. Specifically equations (3-21) and (3-22) describe how the CPMG part (90° excitation pulse followed by a train of 180° pulses, all pulses are on carbon) of the M2S sequence can convert coherences of states such as T_0T_0 to coherences that involve SS state while the same sequence has no effect on coherences of states such as T_0T_1 . This effect is observed experimentally in Figure 16⁵⁷, where peaks corresponding to coherences of the former type are suppressed or inverted by the pulse sequence with right resonance condition while peaks corresponding to coherences of the latter are not perturbed at all. The consistent results from experiment and simulation verify that an inter-pulse delay of 4.92 ms induces the most efficient exchange between the carbon singlet and triplet manifolds and a complete inversion occurs with 45 180° pulses, which corresponds in the simulation to $J_{\text{CC}} = 101.6$ Hz and $\Delta J_{\text{CH}} = 3.4$ Hz.

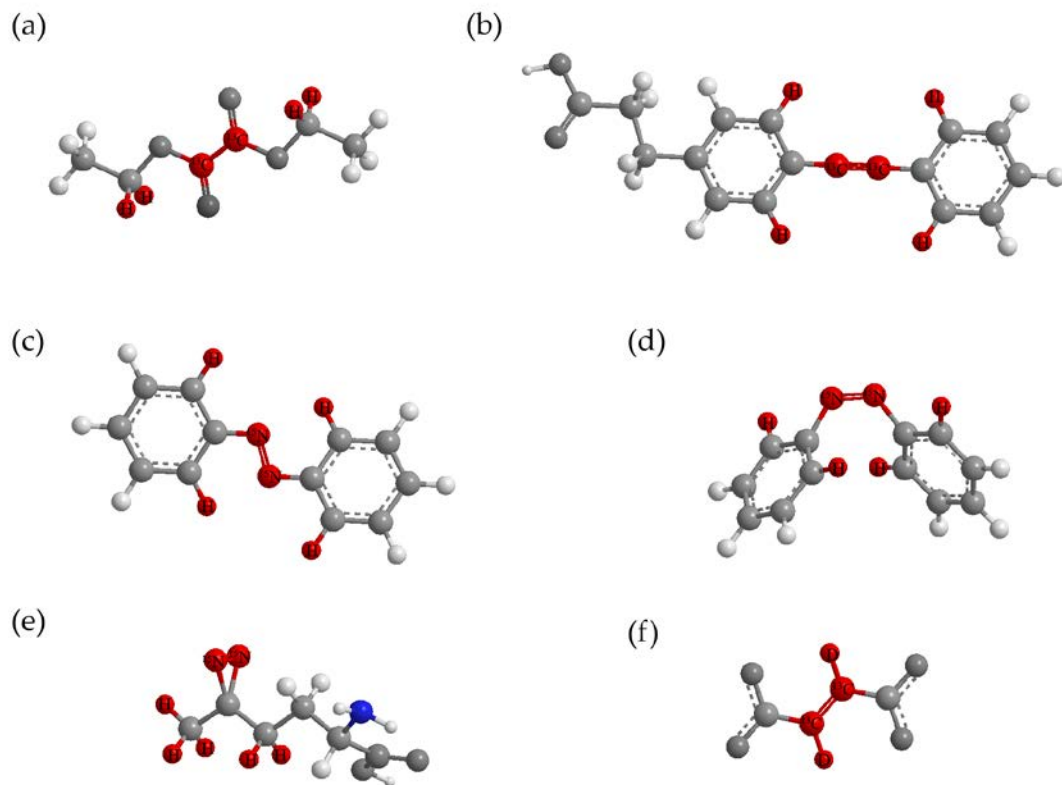


Figure 15. Molecules discussed in chapter 5 that can sustain a long-lived nuclear spin state. (a) $^{13}\text{C}_2$ -diethyl oxalate (DEO). (b) $^{13}\text{C}_2$ -3-(4-(phenylethynyl)phenyl)propanoic acid. (c) $^{15}\text{N}_2$ -azobenzene (trans) (d) $^{15}\text{N}_2$ -azobenzene (cis). (e) $^{15}\text{N}_2$ -photo-methione. (f) $^{13}\text{C}_2$ -D₂-fumarate.

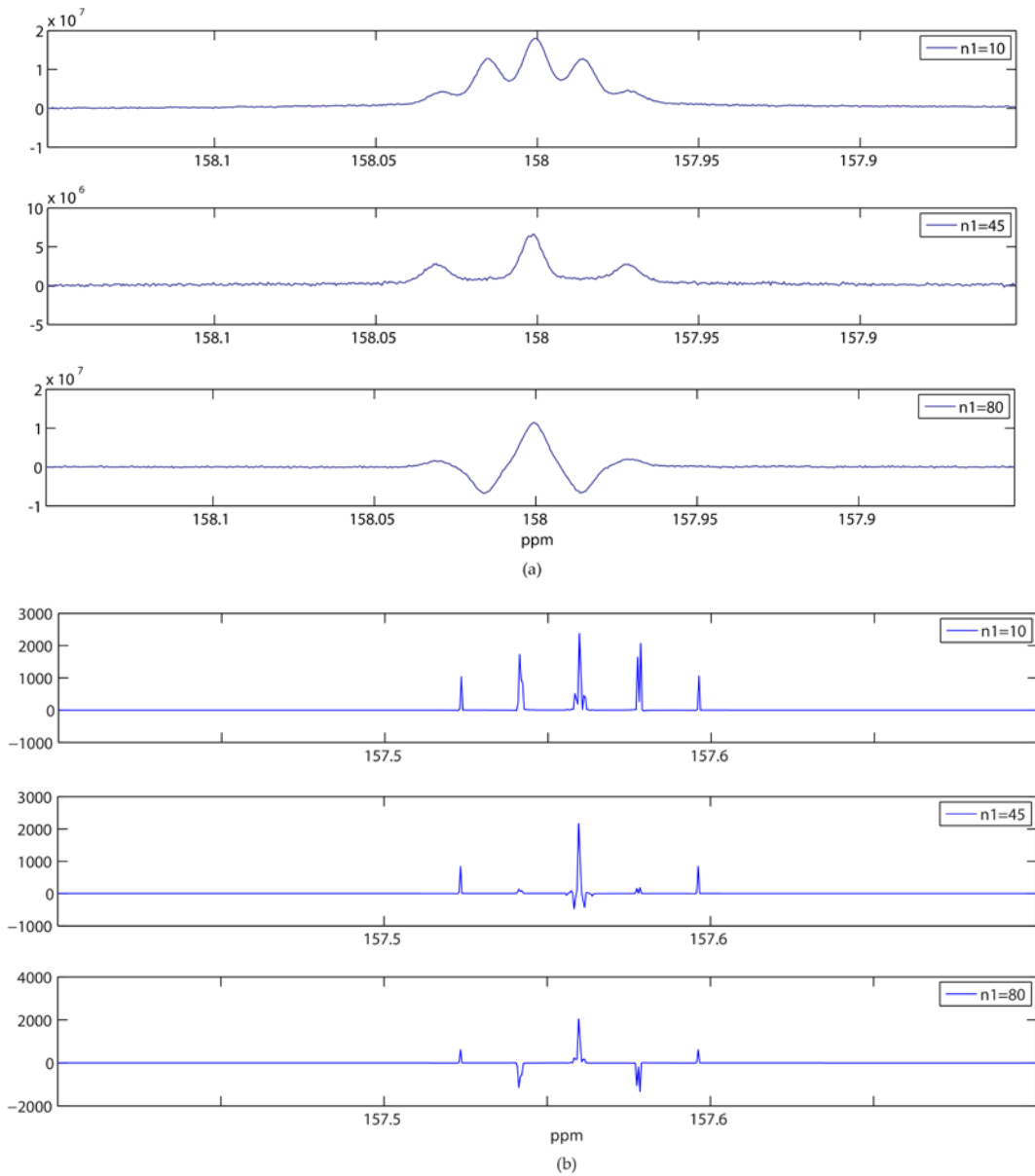
Subsequent measurements of the carbon singlet lifetime using a complete MSM sequence with varied relaxation delay (τ_r in Figure 7) are shown in Figure 17. The first measurement was conducted with thermal polarized sample dissolved in DMSO-d₆ at a concentration of 2 M (Figure 17(a)). Accordingly, a G_z -(90°- G_z)₂ pulse-gradient combination was used as a filter in between M2S and S2M (see Figure 7) to suppress any residual thermal contribution to the final detected signal. The best single exponential fit produced a time constant T_s of around 50.6 s (Figure 17(a)).

The second measurement was conducted with a series of hyperpolarized samples. Each sample contained 4 μL DEO, 1 μL DMSO-d6 and 15 mM Finland radical. Hyperpolarization was achieved using a Hypersense hyperpolarizer (Oxford Instruments Molecular Biotools Ltd). The polarization time constant was 1600 s. After 1 hr of polarization the dissolution of the sample was performed with 3 mL of DMSO at 140 $^{\circ}\text{C}$, resulting in a solution of 0.8 mM hyperpolarized DEO. 50 μL of the hyperpolarized DEO (40nmol DEO) were placed inside a lab-built solenoid coil. In a separate experiment, the liquid state polarization of the hyperpolarized DEO, 40 s after dissolution, was measured to be 3,300 times greater than thermal polarization. The 40 s delay between dissolution and acquisition allowed time for transferring the sample from the Hypersense to the scanner, placing the hyperpolarized DEO inside the coil, and beginning the scan. For each sample, a single scan with fixed τ_r is used to measure the signal strength right after the MSM sequence. The signal strength was expressed by the following formula:

$$S_{\text{Hyperpolarized,singlet}} / S_{\text{Thermal}} = 3300 \times \frac{\sin(5^{\circ})}{\sin(90^{\circ})} \times \frac{S(\text{MSM})}{S(5^{\circ} - \text{acquire})} \quad (5-1)$$

where $S(\text{MSM})$ was the signal after the MSM pulse sequence, and $S(5^{\circ} - \text{acquire})$ was the signal from a 5° -acquire pulse sequence that was performed immediately (100 ms) before the MSM sequence. The singlet state lifetime was then measured by repeating this procedure with multiple samples and varied τ_r . A least-square fit to $\ln(S_{\text{Hyperpolarized,singlet}} /$

S_{Thermal}) as a function of waiting time τ_r was chosen to retrieve the time constant T_s , which is around 41.4 s (Figure 17(b)).



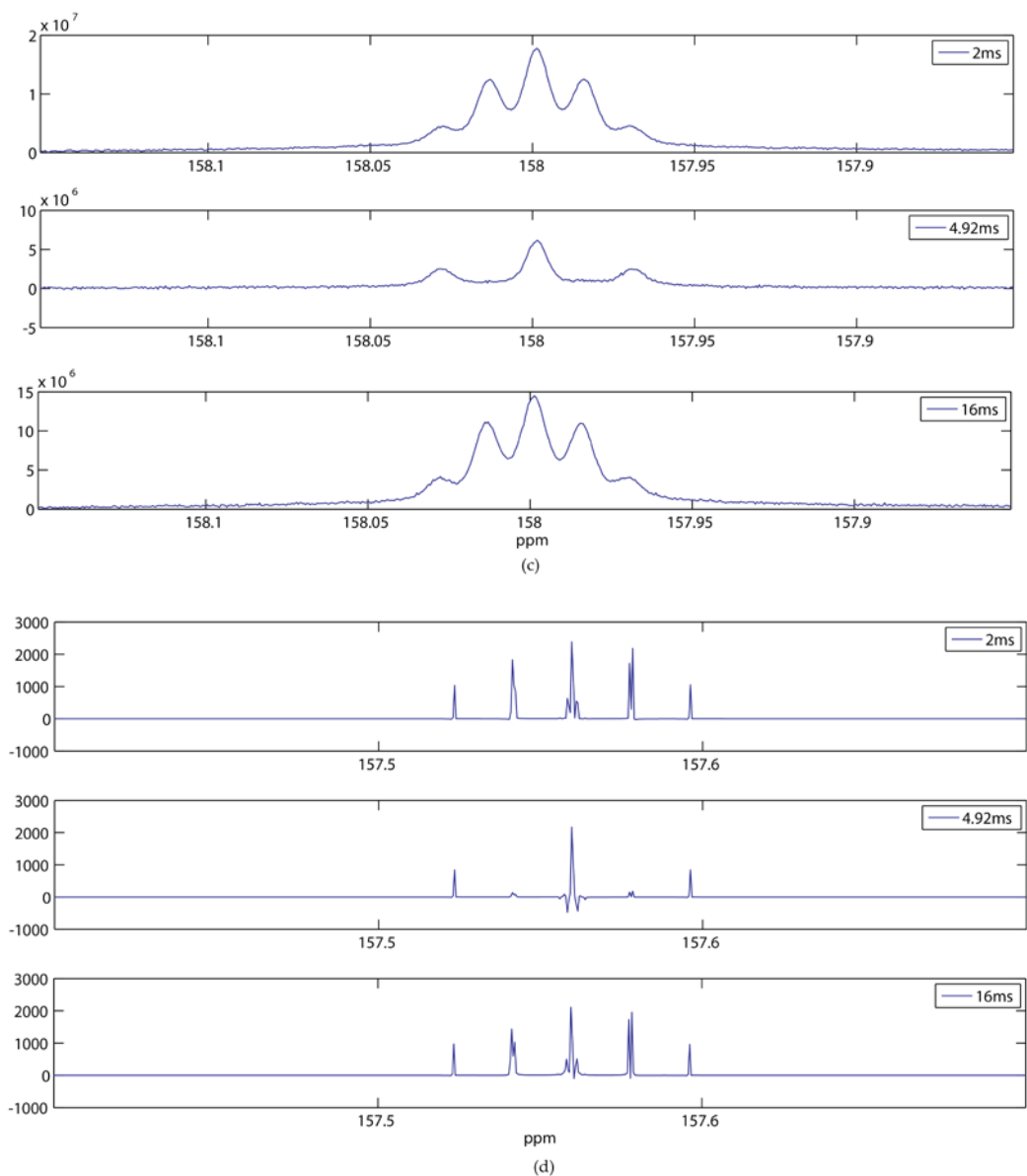


Figure 16. Single scan ^{13}C spectra of DEO from experiments (a,c) and simulations (b,d) after the CPMG part of the M2S sequence. (a-b) perturbation in ^{13}C spectra after the CPMG sequence with the same inter pulse delay 4.92 ms and various number of echo pulses (n_1); maximum conversion in the singlet-triplet subspace occurs after 45 echo pulses, middle row of (b), which is the spectrum after a perfect conversion from carbon triplet to singlet. (c-d) perturbation in ^{13}C spectra after the CPMG sequence with 45 echo pulses and various inter pulse delays ($\tau = 2, 4.92$ or 16 ms). Minimum perturbation can be observed with 2 or 16 ms inter pulse delay.

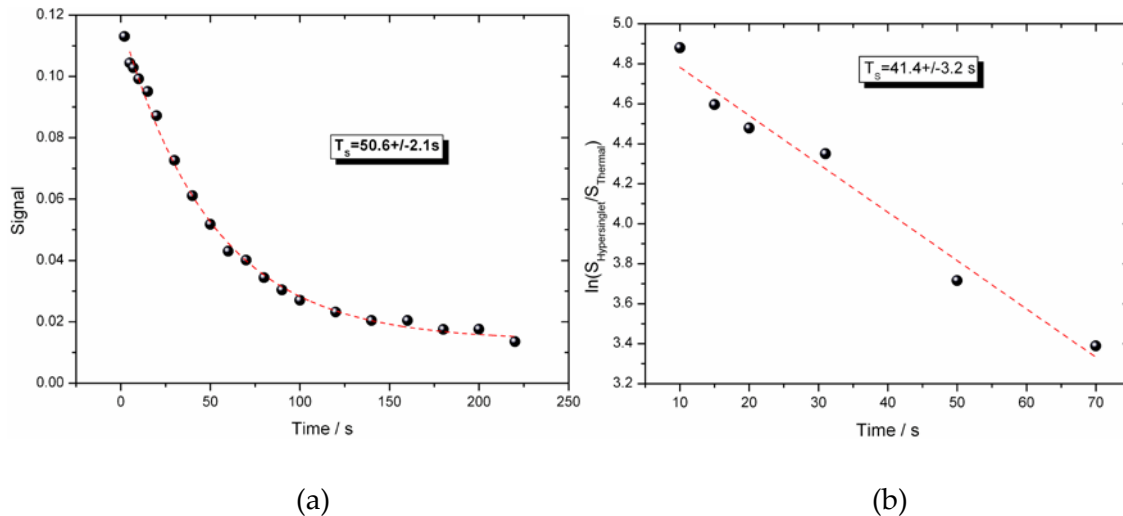


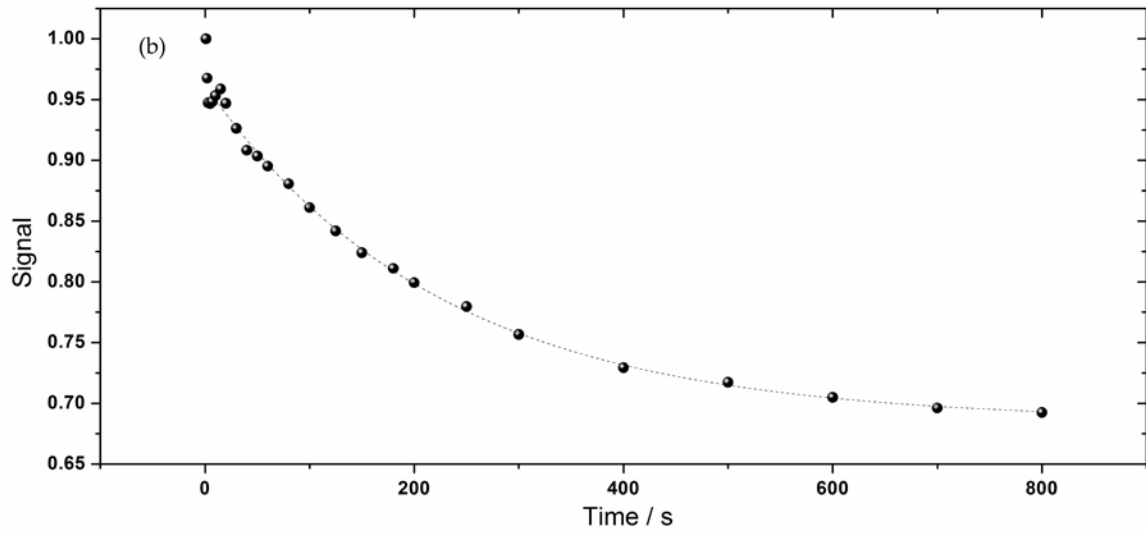
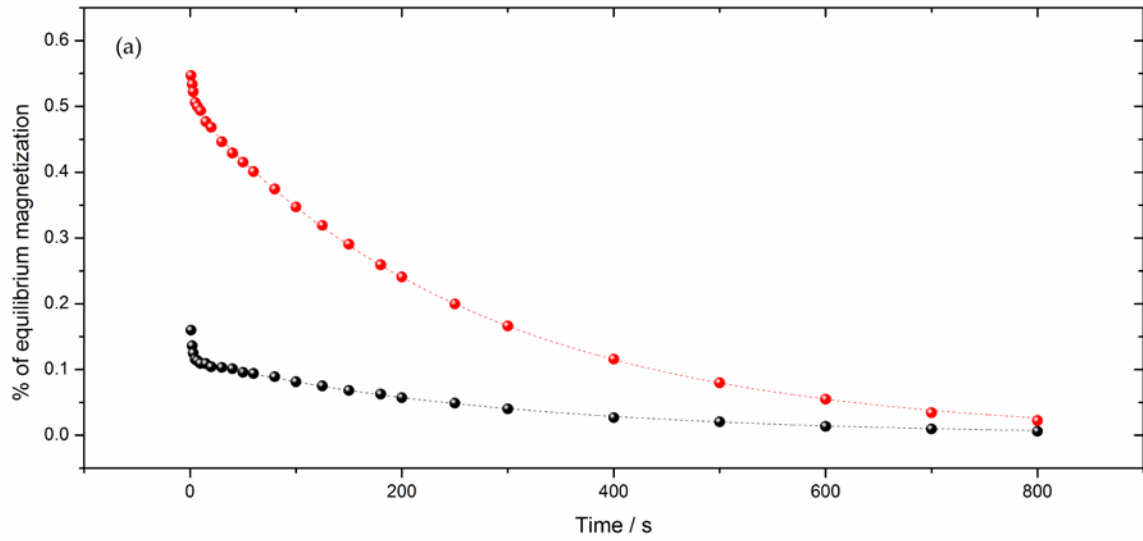
Figure 17. (a) DEO ^{13}C -singlet state signals from the MSM sequence at thermal condition (b) natural logarithm of DNP-hyperpolarized DEO ^{13}C signal from the MSM sequence, all decay as a function of the waiting time τ_r between M2S and S2M sequence. Signal intensity is normalized against the full thermal polarized magnetization in both cases and all estimations include a 95% confidence interval. In (a), T_1 of ^{13}C in DEO is measured to be $22.2 \pm 0.6 \text{ s}$ in a Bruker 360 MHz magnet dissolved with DMSO- d_6 . The singlet signal decays with a lifetime T_s of $50.6 \pm 2.1 \text{ s}$. (b) Hyperpolarized singlet signal is acquired in a 7T (300MHz) Bruker MRI scanner and plotted on a semi-log scale. A T_s of $41.4 \pm 3.2 \text{ s}$ is obtained compared with a T_1 of $23 \pm 0.6 \text{ s}$.

Although the measured T_s was only 2 times longer than T_1 in both cases, the long-lived nature of the carbon singlet state in DEO is indisputable. The residual relaxation on the singlet largely arises from the uncorrelated CSA tensors on the two carbons. This is supported by measurements conducted later at different field strengths (e.g., 16.4 T and 1T), which showed a strong field dependence of T_s .

5.2 $^{13}\text{C}_2$ -diphenyl acetylene (DPA)

In contrast, the two ^{13}C spins in DPA have highly correlated CSA due to the collinear configuration and the same sp hybridization of the electron orbital. This diminishes the CSA-driven relaxation on the singlet state while such relaxation is still effective for ^{13}C T_1 relaxation. The measured J-coupling parameters are $J_{\text{CC}} = 181.8$ Hz and $\Delta J_{\text{CH}} = 6.1$ Hz, giving rise to the desired MSM sequence parameters being $n = 48$ and inter-pulse delay $\tau = 1.365$ ms. As shown in Table 8 and Figure 18, T_s has a much weaker field dependence compared to T_1 , which decreases from 14 s to 5 s with increasing field from 8.45 to 16.44 T. Interconversion between the long-lived state population and proton polarization were fully demonstrated in this study⁷⁸ with thermal polarization. For example, an M2S (^1H)-S2M(^{13}C) (red) results in a nearly 4-fold signal enhancement compared with an MSM (^{13}C only) (black) measurement (Figure 18(a)) yet the fitted T_s is consistent (≈ 288 s) at 8.45 T. Two measurements are also made with proton detection. Figure 18(b) shows an M2S(^{13}C)-S2M(^1H) measurement at 16.44 T; the fitted T_s is around 223 s. Note the signal is normalized to unity due to the fact that the long-lived signal that originated from carbon magnetization only amounts to a tiny fraction of proton magnetization. Nonetheless, as discussed in section 3.6, for constant fractional hyperpolarization, this might be very applicable. The last shown measurement (Figure 18(c)) is an MSM(^1H only) experiment at 16.44 T, which produced a T_s of 261 s, which

amounts to a 69-fold extension compared with proton T_1 (3.8 s) at the same field strength.



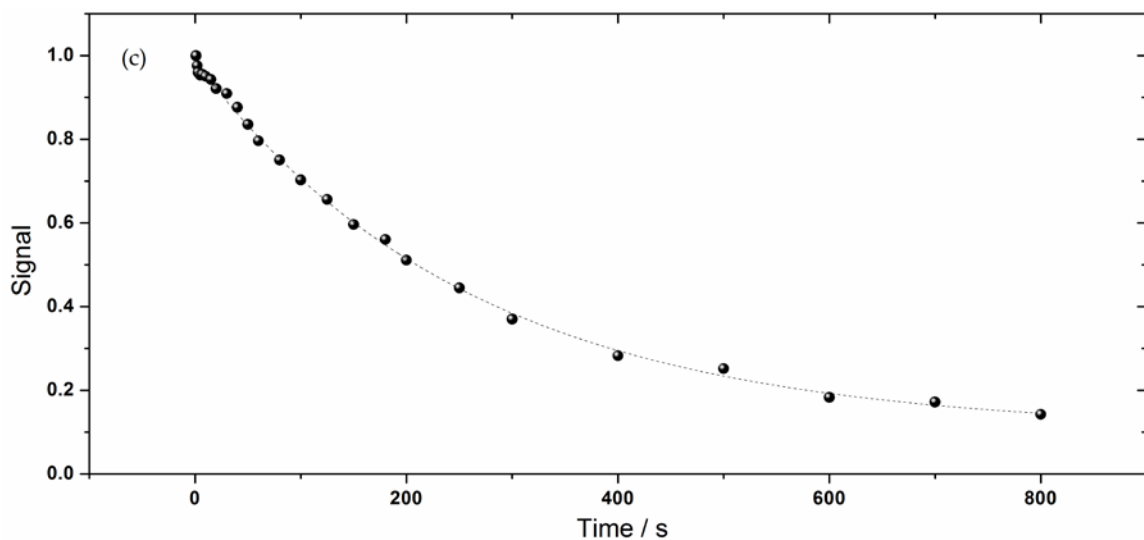


Figure 18. $^{13}\text{C}_2$ -singlet state relaxation lifetime (T_s) measured at 8.45 T (a) and 16.44 T (b-c). (a) A T_s of 288.4 ± 3.7 s is observed (black). This is compared to a singlet state relaxation measurement where the M2S part of the MSM sequence has been applied at the ^1H resonance frequency instead of the ^{13}C resonance frequency (red) resulting in an enhancement of the acquired signal close to 4. For the singlet state relaxation using the ^1H polarization a T_s of 282.7 ± 3.8 s is observed. The small discrepancy in the relaxation times is likely due to subtle differences in the contributions of thermal signal in the two measurements. (b) M2S applied on the ^{13}C channel and S2M applied on the ^1H channel. A T_s of 223 ± 9 s is observed. (c) M2S and S2M applied on the ^1H channel such that the ^{13}C channel remains entirely unused. A T_s of 261 ± 7 s is observed.

Similar signal enhancement due to polarization transfer from proton was observed⁵⁹ by putting the first half of the SLIC sequence on the proton channel. Moreover, the effects of shaped pulse were also revealed in the same study⁵⁹. Shown in Figure 19 are three such measurements on DPA (SLIC with proton preparation and carbon detection) with simple cw pulse, composite cw pulse and adiabatic cw pulse, respectively (discussed in section 3.5.3). The adiabatic shaped SLIC largely compensates

for signal loss due to field inhomogeneity and gives rise to a signal enhancement of 163% compared with the simple SLIC signal.

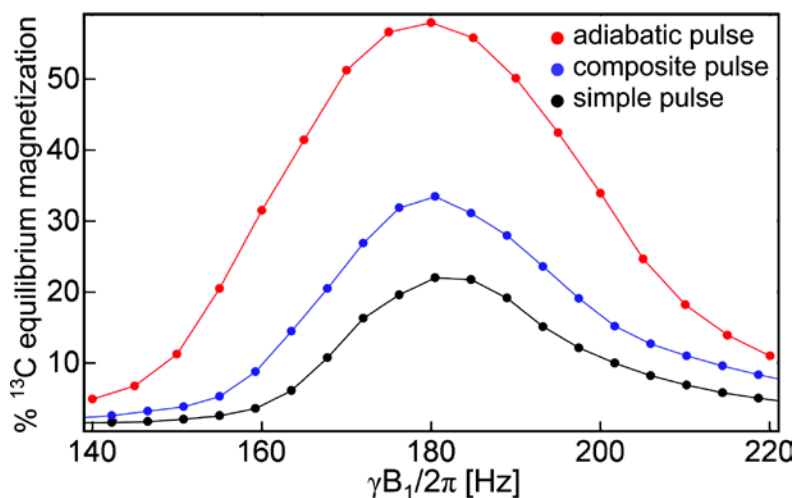
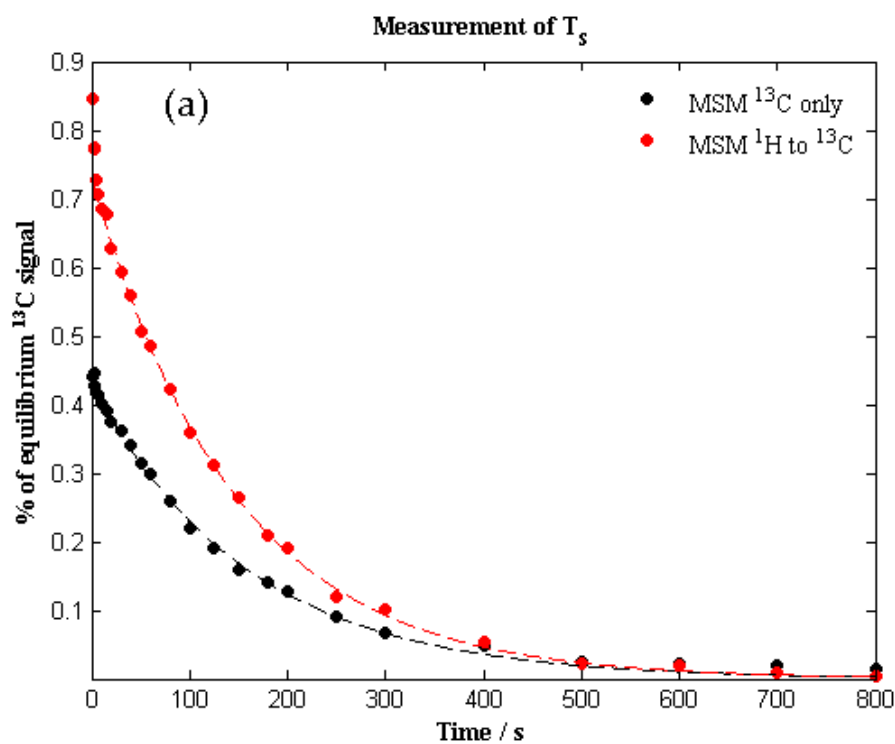


Figure 19. Experimental evaluation of SLIC signal strength against B_1 field inhomogeneity. B_1 has been varied from 140 to 220 Hz. The composite pulse provides a 54% signal enhancement compared with simple cw irradiation whereas the adiabatic pulse gives a signal enhancement of 163% (The solid lines simply connect the points for better visualization).

5.3 $^{13}\text{C}_2$ -meta methyl diphenyl acetylene (mDPA)

Likewise, the same set of measurements was made to mDPA, but with numerically optimized parameters as discussed in section 4.2.1. Figure 20 shows such measurements using the MSM and SLIC sequence, respectively at 8.45 T. As shown in both MSM and SLIC measurements, the signal enhancement from proton polarization transfer is smaller (at most twice as large as the carbon-only experiments) compared with that observed with DPA. It arises from the fact that for mDPA the carbon-only sequences convert all ^{13}C magnetization into the long-lived state population whereas for DPA, only 50% is converted; this has been thoroughly discussed in chapter 3. Moreover,

the measured T_s ($\approx 130 - 140$ s) is significantly shorter than that of DPA at the same field strength due to the large coherent mixing induced by the chemical shift difference ($\Delta\omega = 50.6$ Hz). A much longer T_s (226 s, Table 8) is recovered if a spin-locking field is implemented during the relaxation delay (τ_r). Finally, a proton-only experiment (Figure 20(c)) can extend the proton signal lifetime from 3.5 s (T_1) to 108.1 s (T_s).



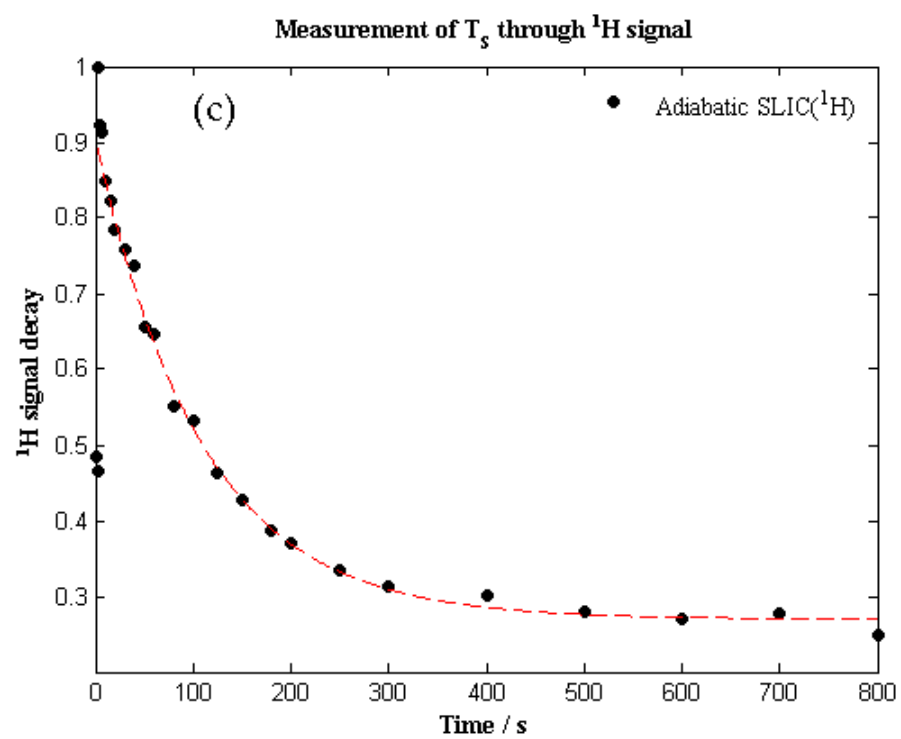
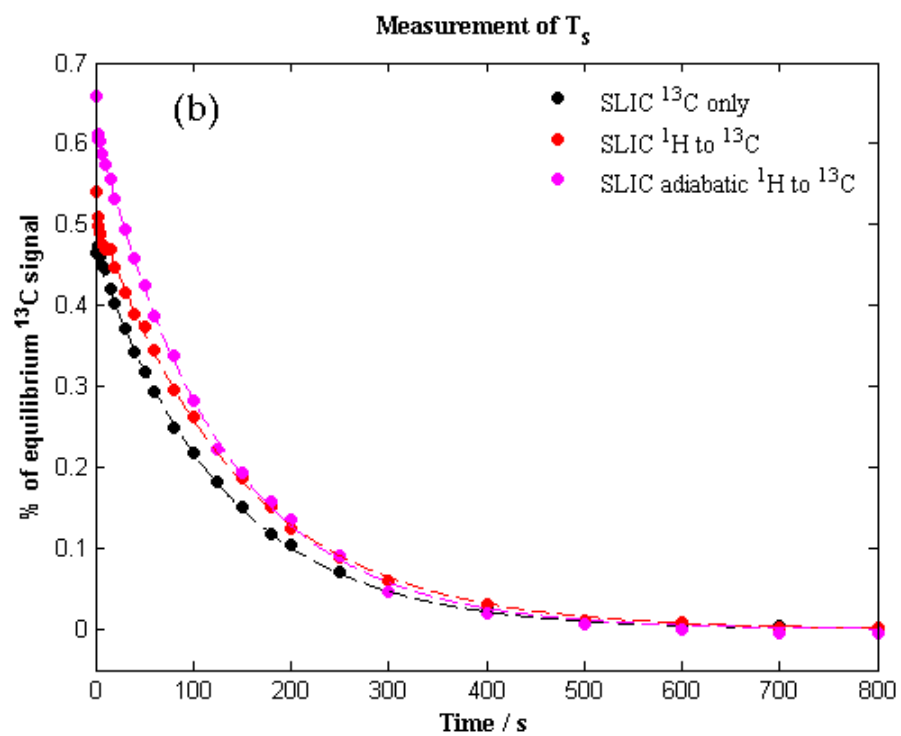


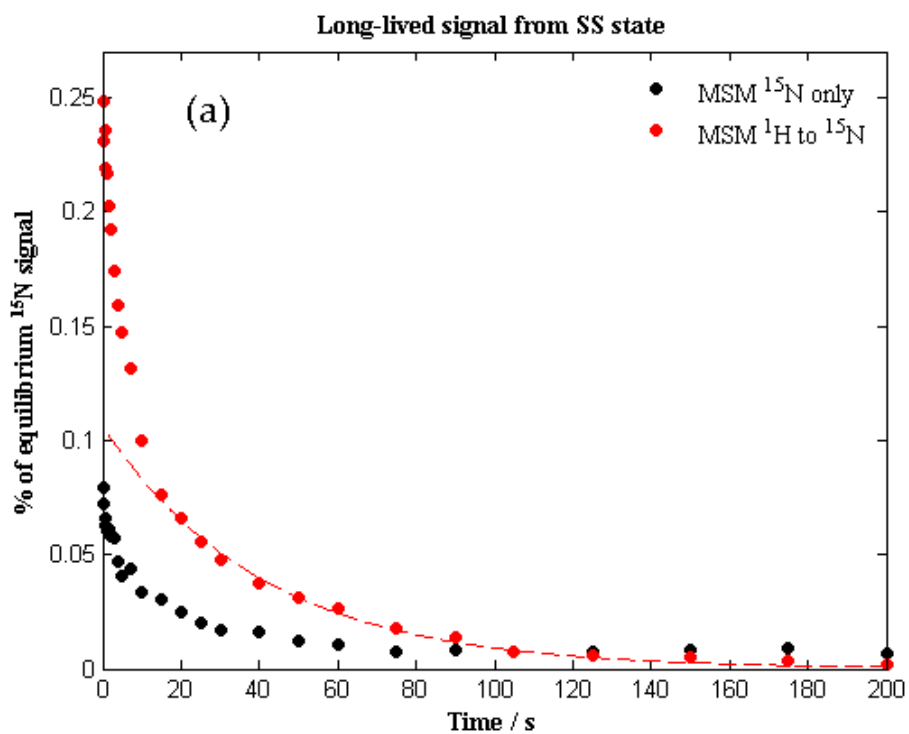
Figure 20. (a) The singlet state lifetime (T_s) measurements from a MSM (^{13}C only, black, $T_s = 146.8 \pm 3.0$ s) and a M2S(^1H)-S2M(^{13}C) (polarization transfer from proton, red, $T_s = 145.5 \pm 2.2$ s), in both measurements, the maximum signal is normalized against a ^{13}C 90° -acquire. (b) The singlet state lifetime (T_s) measurements from a complete SLIC sequence (^{13}C only, black, $T_s = 130.9 \pm 2.4$ s), a complete SLIC (^1H to ^{13}C , polarization transfer from proton, red, $T_s = 128.2 \pm 1.2$ s) and a SLIC sequence with adiabatic proton pulse for polarization transfer (magenta, $T_s = 126.3 \pm 1.7$ s). In all measurements, the maximum signal is normalized against a ^{13}C 90° -acquire. (c) The singlet state lifetime measurement on proton through a proton-only adiabatic SLIC sequence. $T_s = 108.1 \pm 4.0$ s.

5.4 $^{15}\text{N}_2$ -dichloro pyridazine (DCP)

In DCP (Figure 10(b)) there is a $^{15}\text{N}^{15}\text{N}'\text{H}\text{H}'$ 4-spin system with $J_{\text{NN}} = -24$ Hz, $J_{\text{HH}} = 9$ Hz and $\Delta J_{\text{NH}} = 0.54$ Hz. Accordingly, the resonance conditions to access the SS (3-18) and ST_0 (3-19) states are different. For the SS state, the inter-pulse delay (τ) is 33.3 ms and it requires 44 (n) 180° pulses in the first multiple echo sequence of M2S whereas for the ST_0 state, $\tau = 15.2$ ms and $n = 96$. Nevertheless, the total length of the M2S sequence for these two conditions is comparable (around 2.2 s). This long duration gives rise to significant relaxation before the transfer completes. As shown before when M2S is implemented on the proton channel, the sequence transfers proton polarization into the long-lived states. As a result, it generates more than 3 fold signal enhancement compared with a MSM measurement with only ^{15}N pulses (Figure 21). Note that a tenfold increase is expected based on the ratio of gyromagnetic ratios of ^1H and ^{15}N , which is not achieved due to the faster T_2 relaxation of proton compared with ^{15}N . More importantly, the measured lifetime constant T_s is almost indistinguishable for the SS (36.7 s) and ST_0

(37.9 s) states, indicating the long-lived states are largely localized on the singlet across the two ^{15}N spins and very little affected by specific proton states.

The disadvantage of SLIC compared with M2S is also manifested in this molecule. The small “between-pair” J-coupling difference (0.54 Hz) dictates an extremely narrow bandwidth with respect to B_1 inhomogeneity and RF off-resonance. Even a long period of adiabatic cw irradiation (consider the constant amplitude cw irradiation already takes $1/(\pi 2\Delta J_{\text{NH}}) = 1.3$ s) can hardly improve the situation. Consequently, parallel measurements with SLIC did not succeed.



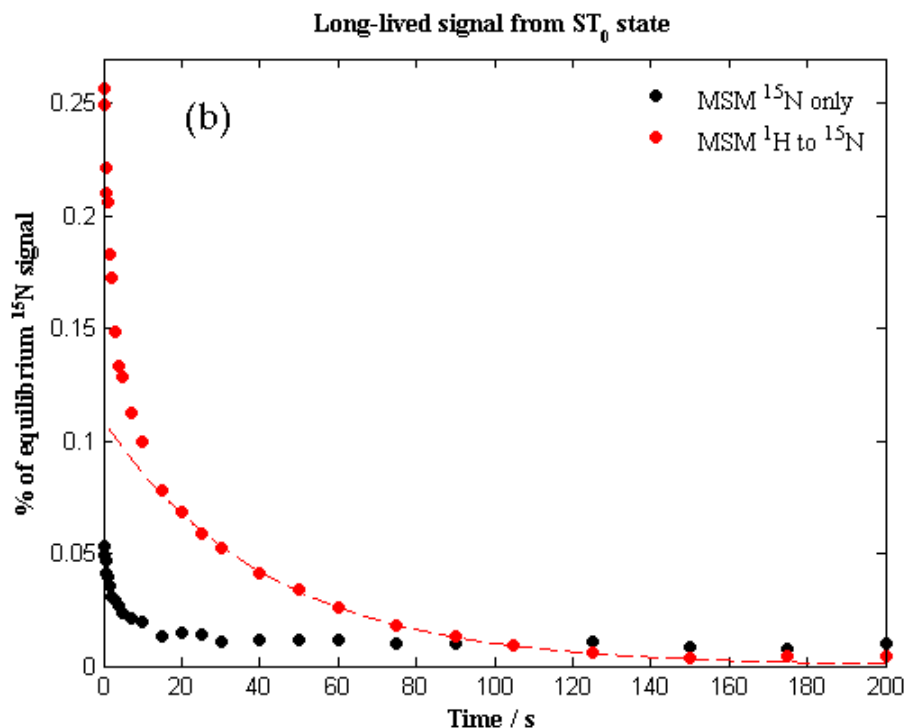


Figure 21. The singlet state relaxation (T_s) measurements on DCP through the MSM sequence. To obtain this data the MSM sequence is run with variable delay τ_r between M2S and S2M giving the Time-axis. The fitted T_s values are obtained from the MSM (^1H to ^{15}N , red curve) sequence. Relaxation decays from MSM (^{15}N only) sequences are shown but measurement of T_s is not taken due to large uncertainties of the fitting. (a) The MSM sequence accesses the $SS-T_0T_0$ 2-level system using an inter-pulse delay τ of 33.3 ms, $T_s = 36.7 \pm 1.8$ s while T_1 is measured to be 15.2 s. (b) The MSM sequence accesses the ST_0-T_0S 2-level system with an inter-pulse delay τ of 15.1 ms, $T_s = 37.9 \pm 1.1$ s.

5.5 $^{15}\text{N}_2$ -azobenzene

Azobenzene has *trans* (Figure 15(c)) and *cis* (Figure 15(d)) isomers and their interconversion is stimulated by UV light irradiation (*trans* to *cis* by 340 nm light, *cis* to *trans* by 450 nm light). Because the *trans* isomer is 10-12 kcal/mol more stable than the *cis*, the *cis* to *trans* conversion can also be accomplished by dark-adapting the solution to restore the equilibrium where the *trans* is the dominant isomer (>99.99%)⁹⁴. The photo-

isomerization of azobenzene has been widely applied to generate large configuration change of biomolecules by incorporating azobenzene or its derivatives into the structure⁹⁴⁻⁹⁹. ¹⁵N₂-azobenzene and its derivatives are also potential bearers for a long-lived ¹⁵N₂-singlet state. For example, Figure 22 shows the measured lifetime (around 50 ~ 60 s at 8.45 T) for the long-lived state in *trans* azobenzene, which is 10 times longer than the T₁ of ¹⁵N and 20 times longer than the T₁ of proton at the same field strength. Notably, the enhancement from proton polarization transfer (Figure 22(a)) is more evident than that obtained with DCP due to the shorter duration of the sequence, which arises from a more favorable set of J-coupling parameters (J_{NN} = -15.5 Hz and ΔJ_{NH} = 2.7 Hz). It would be interesting to also measure the long-lived state lifetime for *cis* azobenzene. According to simulation results, the *cis* configuration induces large difference between the CSA of the two ¹⁵N spins and therefore, a much shorter T_s is expected.

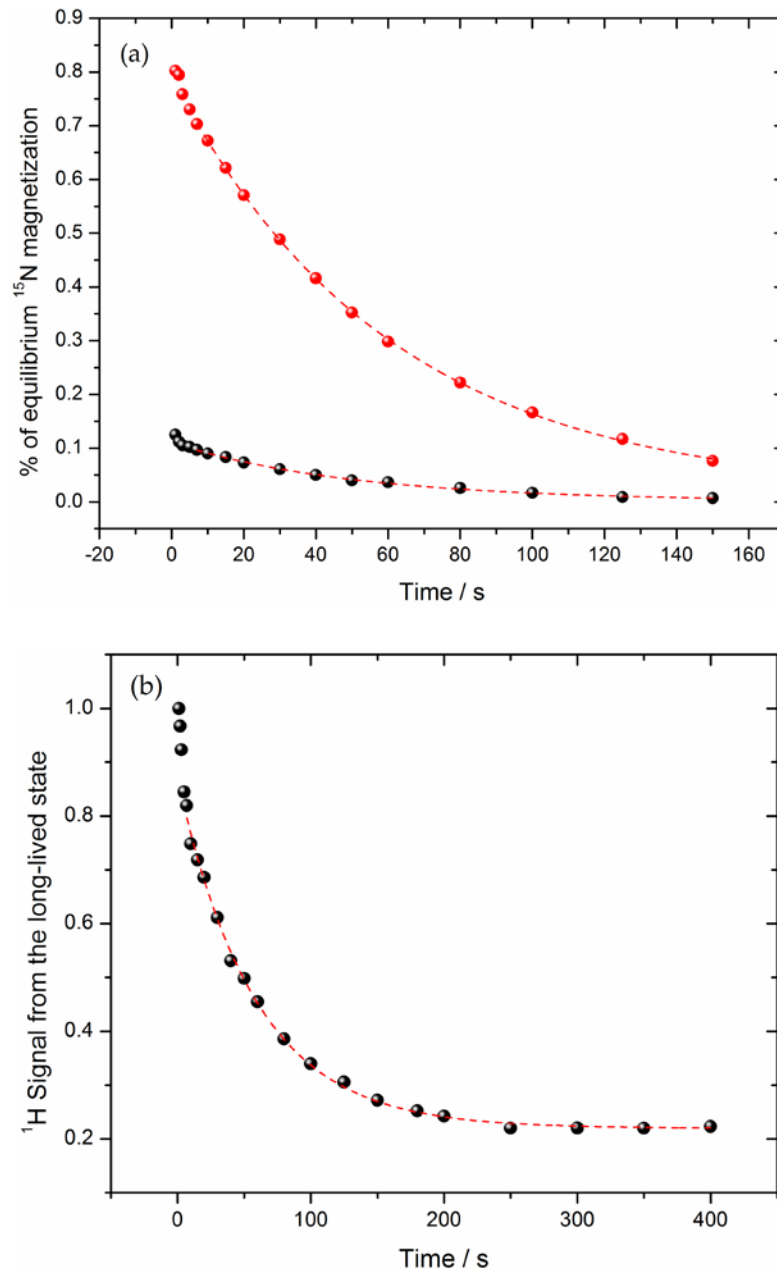


Figure 22. Long-lived signal of $^{15}\text{N}_2$ -azobenzene (trans) measured with the SLIC sequence. Both measurements are taken at 8.45 T. (a) SLIC (^{15}N -only, black) and (^1H preparation ^{15}N detection, red). The measured relaxation lifetimes are $T_s = 54 \pm 2$ s (^{15}N -only) and $T_s = 61 \pm 1$ s (^1H preparation ^{15}N detection). T_1 of ^{15}N is 6 s at the same field strength. Proton polarization transfer results in an 8-fold signal enhancement. (b) SLIC (^1H -only), the measured lifetime $T_s = 58 \pm 2$ s and T_1 of proton is 3 s.

5.6 Molecular tag and structure motif that can be generalized

A crucial question would be how to generalize the structures discussed above so that more biomolecules; being endogenous or their modified derivatives can support such long-lived hyperpolarization. For example, fumarate is an important molecule in the tricarboxylic acid cycle (TCA) and has been hyperpolarized to detect cell necrosis¹⁰⁰⁻¹⁰¹. In those studies, the carbonyl carbons are enriched ^{13}C spins. In contrast, we propose to label the two central carbons and deuterated the attached protons (Figure 15(f)). Then the formed $^{13}\text{C}^{13}\text{C}'\text{DD}'$ 4-spin system is expected to support a long-lived state. Derivatives of DPA are also promising agents to support long-lived states. For example, $^{13}\text{C}_2$ -3-(4-(phenylethynyl)phenyl)propanoic acid (Figure 15(b)) is reported as one potential fatty acid receptor agonist¹⁰²⁻¹⁰⁴. Another interesting structure is $^{15}\text{N}_2$ -diazirine. Diazirine and its derivatives are widely used as photo-affinity agents¹⁰⁵⁻¹⁰⁶; upon UV irradiation, nitrogen breaks off from the “three-member” ring, leaving the carbon as a carbene center. Due to its small size, diazirine is extremely adaptable and is expected to cause little perturbation to properties of the original molecule. The magnetic equivalence between the two ^{15}N spins can be broken by either a small chemical shift difference induced by a remote chiral center or by their different couplings to nearby protons. For example, $^{15}\text{N}_2$ -photo-met (Figure 15(e)) is a derivative of methionine and the chiral center of the α -amino acid induces a chemical shift difference of 0.17 ppm.

The examples above are by no means inclusive since this field is evolving rapidly and new insights into the nature of long-lived states can usually bring into attention the previously unrealized possibility. For example, the fact that quadrupole nuclei such as deuterium can provide access to the long-lived states has extended the range of molecules to those that have two strongly-coupled ^{13}C or ^{15}N spins with directly attached protons. Moreover, for ultimate imaging purpose the field strength (1~3 T) is much lower than that for conventional NMR (e.g., 8.45 T), which can diminish the chemical shift differences between two inequivalent spins and make them suitable to bear a long-lived singlet. Furthermore, relaxation is also reduced in lower field, giving rise to longer relaxation lifetimes. Therefore, it is expected that in near future multiple classes of molecules will emerge as qualified candidates to support long-lived hyperpolarization.

6. Conclusion and future direction

Hyperpolarized magnetic resonance spectroscopy (HP-MRS) is a powerful technique enabling *real-time* monitoring of metabolites at concentration levels not accessible by standard MRI techniques. Its broad application is hindered, however, by the short signal lifetime (T_1) of most hyperpolarized molecules. The long-lived nuclear spin states offer a critical solution to this fundamental challenge. Multiple molecules have been shown to bear such long-lived state that can have lifetime well beyond the T_1 limit. In this thesis, we have discussed the nature of such long-lived states, residual relaxation on those states and possible ways to further suppress such relaxation. The primary focus of this thesis has been to develop methods to induce such long-lived signal for clinical imaging purpose. We have realized a subtle difference between *chemical equivalence* and *magnetic equivalence* can give access to the long-lived states in chemically equivalent or near-equivalent spin systems. We have demonstrated such long-lived signal with multiple pulse sequence techniques and more importantly, we have shown such states can store both heteronuclear (^{13}C , ^{15}N , etc.) and proton magnetization for extended lifetime, which will largely facilitate its application to clinical imaging.

Future research will focus on implementation of this technique in lower field (e.g., from a few tens of mT to 1T) where relaxation is further suppressed while signal strength of hyperpolarization remains comparable to that in high field magnet. On the

other hand, it has been demonstrated that long-lived signal from for example, the singlet state between a pair of ^{13}C spins can be detected with natural abundance (1%) ^{13}C sample combined with high field (16.44 T) magnet and cryogen probe¹⁰⁷. This enables immediate screening of different classes of molecules without resorting to expensive and time-consuming synthesis of isotope-enriched compounds. Therefore, a range of biologically relevant molecules that can sustain long-lived hyperpolarization are expected in the near future. Lastly, interests in the long-lived hyperpolarization originates from para-hydrogen are renewed given the spin population in para-hydrogen can now be converted to detectable magnetization in a well-controlled manner using the techniques developed here. Considering its lower cost and relatively easy implementation, PHIP may emerge as a crucial alternative to DNP for clinical imaging in the near future.

Appendix

Spin states formed to describe the X_2X_2' and the AA' subsystems in DPA. Listed are also the associated irreducible representations in the D_{2h} point group.

Symmetry	^1H States
A_g (spin 2)	$T_{-1}T_{-1}, (T_{-1}T_0 + T_0T_{-1})/\sqrt{2}, (T_{-1}T_{+1} + T_{+1}T_{-1} + 2T_0T_0)/\sqrt{6},$ $(T_1T_0 + T_0T_1)/\sqrt{2}, T_1T_1$
B_{1u} (spin 1)	$(T_{-1}T_0 - T_0T_{-1})/\sqrt{2}, (T_{-1}T_{+1} - T_{+1}T_{-1})/\sqrt{2}, (T_1T_0 - T_0T_1)/\sqrt{2}$
B_{2u} (spin 1)	$(T_{-1}S + ST_{-1})/\sqrt{2}, (T_0S + ST_0)/\sqrt{2}, (T_1S + ST_1)/\sqrt{2}$
B_{3g} (spin 1)	$(T_{-1}S - ST_{-1})/\sqrt{2}, (T_0S - ST_0)/\sqrt{2}, (T_1S - ST_1)/\sqrt{2}$
A_g (spin 0)	$(T_{-1}T_{+1} + T_{+1}T_{-1} - T_0T_0)/\sqrt{3}, SS$
Symmetry	^{13}C States
B_{1u} (spin 0)	S
A_g (spin 1)	T_{+1}, T_0, T_{-1}

References

1. Abragam, A.; Proctor, W., Spin Temperature. *Physical Review* **1958**, *109* (5), 1441-1458.
2. Abragam, A., *The Principles of Nuclear Magnetism*. Oxford, Clarendon Press.: 1961.
3. Slichter, C. P., *Principles of Magnetic Resonance*. Springer-Verlag: Berlin ; New York, 1989.
4. Ernst, R. R.; Bodenhausen, G.; Wokaun, A., *Principles of Nuclear Magnetic Resonance in One and Two Dimensions*. Clarendon Press; Oxford University Press: Oxford [Oxfordshire]; New York, 1987.
5. Hoekstra, O. S.; Juweid, M. E., *Positron Emission Tomography*. Humana Press: New York, 2011.
6. Carver, T.; Slichter, C., Polarization of Nuclear Spins in Metals. *Physical Review* **1953**, *92* (1), 212-213.
7. Overhauser, A., Polarization of Nuclei in Metals. *Physical Review* **1953**, *92* (2), 411-415.
8. Abragam, A., Overhauser Effect in Nonmetals. *Physical Review* **1955**, *98* (6), 1729-1735.
9. Abragam, A.; Goldman, M., Principles of Dynamic Nuclear Polarisation. *Rep. Prog. Phys.* **1978**, *41*, 395-467.
10. Hall, D. A.; Maus, D. C.; Gerfen, G. J.; Inati, S. J.; Becerra, L. R.; Dahlquist, F. W.; Griffin, R. G., Polarization-Enhanced Nmr Spectroscopy of Biomolecules in Frozen Solution. *Science* **1997**, *276* (5314), 930-932.
11. Ardenkjaer-Larsen, J. H.; Fridlund, B.; Gram, A.; Hansson, G.; Hansson, L.; Lerche, M. H.; Servin, R.; Thaning, M.; Golman, K., Increase in Signal-to-Noise Ratio of > 10,000 Times in Liquid-State Nmr. *Proceedings of the National Academy of Sciences of the United States of America* **2003**, *100* (18), 10158-10163.
12. Brindle, K. M.; Bohndiek, S. E.; Gallagher, F. A.; Kettunen, M. I., Tumor Imaging Using Hyperpolarized (13)C Magnetic Resonance. *Magnetic Resonance in Medicine* **2011**, *66* (2), 505-519.

13. Kurhanewicz, J.; Vigneron, D. B.; Brindle, K.; Chekmenev, E. Y.; Comment, A.; Cunningham, C. H.; DeBerardinis, R. J.; Green, G. G.; Leach, M. O.; Rajan, S. S.; Rizi, R. R.; Ross, B. D.; Warren, W. S.; Malloy, C. R., Analysis of Cancer Metabolism by Imaging Hyperpolarized Nuclei: Prospects for Translation to Clinical Research. *Neoplasia* **2011**, *13* (2), 81-97.
14. Nelson, S. J.; Kurhanewicz, J.; Vigneron, D. B.; Larson, P. E. Z.; Harzstark, A. L.; Ferrone, M.; van Criekinge, M.; Chang, J. W.; Bok, R.; Park, I.; Reed, G.; Carvajal, L.; Small, E. J.; Munster, P.; Weinberg, V. K.; Ardenkjaer-Larsen, J. H.; Chen, A. P.; Hurd, R. E.; Odegaardstuen, L.-I.; Robb, F. J.; Tropp, J.; Murray, J. A., Metabolic Imaging of Patients with Prostate Cancer Using Hyperpolarized [1-13c]Pyruvate. *Science Translational Medicine* **2013**, *5* (198), 198ra108.
15. Warburg, O.; Wind, F.; Negelein, E., Metabolism of Tumors in the Body. *Klin Wochenschr* **1926**, *5* ((19)), 829-832.
16. Gatenby, R. A.; Gillies, R. J., Why Do Cancers Have High Aerobic Glycolysis? *Nat. Rev. Cancer* **2004**, *4* (11), 891-899.
17. Natterer, J.; Bargon, J., Parahydrogen Induced Polarization. *Prog. Nucl. Magn. Reson. Spectrosc.* **1997**, *31*, 293-315.
18. Canet, D.; Aroulanda, C.; Mutzenhardt, P.; Aime, S.; Gobetto, R.; Reineri, F., Para-Hydrogen Enrichment and Hyperpolarization. *Concepts Magn. Reson. Part A* **2006**, *28A* (5), 321-330.
19. Bowers, C. R.; Weitekamp, D. P., Transformation of Symmetrization Order to Nuclear-Spin Magnetization by Chemical-Reaction and Nuclear-Magnetic-Resonance. *Phys. Rev. Lett.* **1986**, *57* (21), 2645-2648.
20. Pravica, M. G.; Weitekamp, D. P., Net Nmr Alignment by Adiabatic Transport of Para-Hydrogen Addition-Products to High Magnetic-Field. *Chem. Phys. Lett.* **1988**, *145* (4), 255-258.
21. Adams, R. W.; Aguilar, J. A.; Atkinson, K. D.; Cowley, M. J.; Elliott, P. I. P.; Duckett, S. B.; Green, G. G. R.; Khazal, I. G.; Lopez-Serrano, J.; Williamson, D. C., Reversible Interactions with Para-Hydrogen Enhance Nmr Sensitivity by Polarization Transfer. *Science* **2009**, *323* (5922), 1708-1711.
22. Adams, R. W.; Duckett, S. B.; Green, R. A.; Williamson, D. C.; Green, G. G. R., A Theoretical Basis for Spontaneous Polarization Transfer in Non-Hydrogenative Parahydrogen-Induced Polarization. *Journal of Chemical Physics* **2009**, *131* (19).

23. Green, R. A.; Adams, R. W.; Duckett, S. B.; Mewis, R. E.; Williamson, D. C.; Green, G. G., The Theory and Practice of Hyperpolarization in Magnetic Resonance Using Parahydrogen. *Prog Nucl Magn Reson Spectrosc* **2012**, *67*, 1-48.
24. Hovener, J. B.; Schwaderlapp, N.; Lickert, T.; Duckett, S. B.; Mewis, R. E.; Highton, L. A.; Kenny, S. M.; Green, G. G.; Leibfritz, D.; Korvink, J. G.; Hennig, J.; von Elverfeldt, D., A Hyperpolarized Equilibrium for Magnetic Resonance. *Nature communications* **2013**, *4*, 2946.
25. Bouchiat, M. A.; Carver, T. R.; Varnum, C. M., Nuclear Polarization in He-3 Gas Induced by Optical Pumping and Dipolar Exchange. *Physical Review Letters* **1960**, *5* (8), 373-375.
26. Colegrove, F. D.; Schearer, L. D.; Walters, G. K., Polarization of He3 Gas by Optical Pumping. *Physical Review* **1963**, *132* (6), 2561-&.
27. Kauczor, H. U.; Surkau, R.; Roberts, T., Mri Using Hyperpolarized Noble Gases. *Eur. Radiol.* **1998**, *8* (5), 820-827.
28. Moller, H. E.; Chen, X. J.; Saam, B.; Hagspiel, K. D.; Johnson, G. A.; Altes, T. A.; de Lange, E. E.; Kauczor, H. U., Mri of the Lungs Using Hyperpolarized Noble Gases. *Magnetic Resonance in Medicine* **2002**, *47* (6), 1029-1051.
29. Driehuys, B.; Moller, H. E.; Cleveland, Z. I.; Pollaro, J.; Hedlund, L. W., Pulmonary Perfusion and Xenon Gas Exchange in Rats: Mr Imaging with Intravenous Injection of Hyperpolarized (129)Xe. *Radiology* **2009**, *252* (2), 386-393.
30. Virgincar, R. S.; Cleveland, Z. I.; Kaushik, S. S.; Freeman, M. S.; Nouls, J.; Cofer, G. P.; Martinez-Jimenez, S.; He, M.; Kraft, M.; Wolber, J.; McAdams, H. P.; Driehuys, B., Quantitative Analysis of Hyperpolarized 129xe Ventilation Imaging in Healthy Volunteers and Subjects with Chronic Obstructive Pulmonary Disease. *Nmr in Biomedicine* **2013**, *26* (4), 424-435.
31. Carravetta, M.; Levitt, M. H., Theory of Long-Lived Nuclear Spin States in Solution Nuclear Magnetic Resonance. I. Singlet States in Low Magnetic Field. *The Journal of chemical physics* **2005**, *122* (21), 214505.
32. Pileio, G.; Levitt, M. H., Theory of Long-Lived Nuclear Spin States in Solution Nuclear Magnetic Resonance. Ii. Singlet Spin Locking. *The Journal of chemical physics* **2009**, *130* (21), 214501.

33. Pileio, G., Spin Dynamics. <http://spindynamics.org> **2013**, Module III (Lecture V-VIII).
34. Levitt, M. H., *Spin Dynamics: Basics of Nuclear Magnetic Resonance*. John Wiley & Sons Ltd: Chichester, West Sussex, England, 2008.
35. Carravetta, M.; Johannessen, O. G.; Levitt, M. H., Beyond the T-1 Limit: Singlet Nuclear Spin States in Low Magnetic Fields. *Phys. Rev. Lett.* **2004**, 92 (15), 153003.
36. Carravetta, M.; Levitt, M. H., Long-Lived Nuclear Spin States in High-Field Solution Nmr. *J. Am. Chem. Soc.* **2004**, 126 (20), 6228-6229.
37. Bloembergen, N.; Purcell, E. M.; Pound, R. V., Relaxation Effects in Nuclear Magnetic Resonance Absorption. *Physical Review* **1948**, 73 (7), 679-712.
38. Redfield, A. G., On the Theory of Relaxation Processes. *Ibm Journal of Research and Development* **1957**, 1 (1), 19-31.
39. Solomon, I., Relaxation Processes in a System of 2 Spins. *Physical Review* **1955**, 99 (2), 559-565.
40. Goldman, M., Formal Theory of Spin-Lattice Relaxation. *Journal of Magnetic Resonance* **2001**, 149 (2), 160-187.
41. Kowalewski, J.; Maler, L., *Nuclear Spin Relaxation in Liquids : Theory, Experiments, and Applications*. Taylor & Francis: Independence, KY, USA, 2006.
42. Kuprov, I., Spin Dynamics. <http://spindynamics.org> **2013**, Module III (Lecture I,II,III).
43. Pileio, G., Singlet State Relaxation Via Intermolecular Dipolar Coupling. *J. Chem. Phys.* **2011**, 134 (21).
44. Pileio, G., Singlet State Relaxation Via Scalar Coupling of the Second Kind. *J. Chem. Phys.* **2011**, 135 (17).
45. Pileio, G.; Hill-Cousins, J. T.; Mitchell, S.; Kuprov, I.; Brown, L. J.; Brown, R. C. D.; Levitt, M. H., Long-Lived Nuclear Singlet Order in near-Equivalent C-13 Spin Pairs. *J. Am. Chem. Soc.* **2012**, 134 (42), 17494-17497.
46. Pileio, G., Relaxation Theory of Nuclear Singlet States in Two Spin-1/2 Systems. *Prog. Nucl. Magn. Reson. Spectrosc.* **2010**, 56 (3), 217-231.

47. Hogben, H. J.; Hore, P. J.; Kuprov, I., Multiple Decoherence-Free States in Multi-Spin Systems. *Journal of Magnetic Resonance* **2011**, *211* (2), 217-220.
48. Pileio, G.; Levitt, M. H., J-Stabilization of Singlet States in the Solution Nmr of Multiple-Spin Systems. *Journal of Magnetic Resonance* **2007**, *187* (1), 141-145.
49. Vinogradov, E.; Grant, A. K., Long-Lived States in Solution Nmr: Selection Rules for Intramolecular Dipolar Relaxation in Low Magnetic Fields. *Journal of Magnetic Resonance* **2007**, *188*, 176-182.
50. Kuprov, I., Diagonalization-Free Implementation of Spin Relaxation Theory for Large Spin Systems. *Journal of Magnetic Resonance* **2011**, *209* (1), 31-38.
51. Jeener, J., Superoperators in Magnetic-Resonance. *Advances in Magnetic Resonance* **1982**, *10*, 1-51.
52. Varshalovich, D. A., *Quantum Theory of Angular Momentum : Irreducible Tensors, Spherical Harmonics, Vector Coupling Coefficients, 3nj Symbols*. World Scientific Pub.: Singapore ; Teaneck, NJ, 1988.
53. Tayler, M. C. D.; Marie, S.; Ganesan, A.; Levitt, M. H., Determination of Molecular Torsion Angles Using Nuclear Singlet Relaxation. *J. Am. Chem. Soc.* **2010**, *132* (24), 8225-8227.
54. Pileio, G.; Carravetta, M.; Hughes, E.; Levitt, M. H., The Long-Lived Nuclear Singlet State of ¹⁵N-Nitrous Oxide in Solution. *J Am Chem Soc* **2008**, *130* (38), 12582-3.
55. Grant, A. K.; Vinogradov, E., Long-Lived States in Solution Nmr: Theoretical Examples in Three- and Four-Spin Systems. *Journal of Magnetic Resonance* **2008**, *193* (2), 177-190.
56. Ahuja, P.; Sarkar, R.; Vasos, P. R.; Bodenhausen, G., Long-Lived States in Multiple-Spin Systems. *ChemPhysChem* **2009**, *10* (13), 2217-2220.
57. Feng, Y.; Davis, R. M.; Warren, W. S., Accessing Long-Lived Nuclear Singlet States between Chemically Equivalent Spins without Breaking Symmetry. *Nat Phys* **2012**, *8* (11), 831-837.
58. Levitt, M. H., Singlet and Other States with Extended Lifetimes. In *Emagres*, John Wiley & Sons, Ltd: 2007.

59. Theis, T.; Feng, Y.; Wu, T.; Warren, W. S., Composite and Shaped Pulses for Efficient and Robust Pumping of Disconnected Eigenstates in Magnetic Resonance. *The Journal of chemical physics* **2014**, *140* (1), 014201.
60. Warren, W. S.; Jenista, E.; Branca, R. T.; Chen, X., Increasing Hyperpolarized Spin Lifetimes through True Singlet Eigenstates. *Science* **2009**, *323* (5922), 1711-1714.
61. Pileio, G.; Carravetta, M.; Levitt, M. H., Storage of Nuclear Magnetization as Long-Lived Singlet Order in Low Magnetic Field. *PNAS* **2011**, *107* (40), 17135-17139.
62. Tayler, M. C. D.; Levitt, M. H., Singlet Nuclear Magnetic Resonance of Nearly-Equivalent Spins. *Physical Chemistry Chemical Physics* **2011**, *13* (13), 5556-5560.
63. McConnell, H. M.; McLean, A. D.; Reilly, C. A., Analysis of Spin-Spin Multiplets in Nuclear Magnetic Resonance Spectra. *J. Chem. Phys.* **1955**, *23* (6), 1152-1157.
64. Bernstein, H. J.; Pople, J. A.; Schneider, W. G., The Analysis of Nuclear Magnetic Resonance Spectra .1. Systems of 2 and 3 Nuclei. *Can. J. Chem.-Rev. Can. Chim.* **1957**, *35* (1), 65-81.
65. Pople, J. A.; Schneider, W. G.; Bernstein, H. J., The Analysis of Nuclear Magnetic Resonance Spectra .2. 2 Pairs of 2 Equivalent Nuclei. *Can. J. Chem.-Rev. Can. Chim.* **1957**, *35* (9), 1060-1072.
66. Atkins, P. W., *Molecular Quantum Mechanics*. Oxford University Press: Oxford ; New York, 2011.
67. DeVience, S. J.; Walsworth, R. L.; Rosen, M. S., Preparation of Nuclear Spin Singlet States Using Spin-Lock Induced Crossing. *Phys. Rev. Lett.* **2013**, *111* (17).
68. Levitt, M. H.; Freeman, R., Nmr Population Inversion Using a Composite Pulse. *Journal of Magnetic Resonance (1969)* **1979**, *33* (2), 473-476.
69. Levitt, M. H., Composite Pulses. *Progress in Nuclear Magnetic Resonance Spectroscopy* **1986**, *18* (2), 61-122.
70. Warren, W. S., Effects of Pulse Shaping in Laser Spectroscopy and Nuclear Magnetic Resonance. *Science* **1988**, *242* (4880), 878-84.
71. Warren, W. S.; Silver, M. S., The Art of Pulse Crafting. *Advances in Magnetic Resonance* **1988**, *12*, 248-384.

72. Garwood, M.; DelaBarre, L., The Return of the Frequency Sweep: Designing Adiabatic Pulses for Contemporary Nmr. *J. Magn. Reson.* **2001**, *153* (2), 155-177.
73. Baum, J.; Tycko, R.; Pines, A., Broadband and Adiabatic Inversion of a Two-Level System by Phase-Modulated Pulses. *Physical Review A* **1985**, *32* (6), 3435-3447.
74. Allen, L.; Eberly, J. H., *Optical Resonance and Two-Level Atoms*. Wiley: New York, 1975.
75. Silver, M. S.; Joseph, R. I.; Hoult, D. I., *Physical Review A* **1985**, *31*, 2753.
76. Melinger, J. S.; Gandhi, S. R.; Hariharan, A.; Goswami, D.; Warren, W. S., Adiabatic Population Transfer with Frequency-Swept Laser-Pulses. *J Chem Phys* **1994**, *101* (8), 6439-6454.
77. Davis, J. C.; Fetterman, M. R.; Warren, W. S.; Goswami, D., Propagation of Complex Shaped Ultrafast Pulses in Highly Optically Dense Samples. *J Chem Phys* **2008**, *128* (15), 154312.
78. Feng, Y.; Theis, T.; Liang, X.; Wang, Q.; Zhou, P.; Warren, W. S., Storage of Hydrogen Spin Polarization in Long-Lived ^{13}C Singlet Order and Implications for Hyperpolarized Magnetic Resonance Imaging. *J. Am. Chem. Soc.* **2013**, *135* (26), 9632-9635.
79. Hoult, D. I.; Richards, R. E., The Signal-to-Noise Ratio of the Nuclear Magnetic Resonance Experiment. *Journal of Magnetic Resonance* **1976**, *24*, 71-85.
80. Hoult, D. I., Sensitivity of the Nmr Experiment. *Encyclopedia of Magnetic Resonance* **2007**.
81. Buljubasich, L.; Franzoni, M. B.; Spiess, H. W.; Munnemann, K., Level Anti-Crossings in Parahydrogen Induced Polarization Experiments with Cs-Symmetric Molecules. *Journal of Magnetic Resonance* **2012**, *219*, 33-40.
82. Franzoni, M. B.; Buljubasich, L.; Spiess, H. W.; Munnemann, K., Long-Lived ^1H Singlet Spin States Originating from Para-Hydrogen in Cs-Symmetric Molecules Stored for Minutes in High Magnetic Fields. *J Am Chem Soc* **2012**, *134* (25), 10393-6.
83. Franzoni, M. B.; Graafen, D. M.; Buljubasich, L.; Schreiber, L. M.; Spiess, H. W.; Munnemann, K., Hyperpolarized ^1H Long Lived States Originating from Parahydrogen Accessed by Rf Irradiation. *Physical Chemistry Chemical Physics* **2013**, *15*, 17233-17239.

84. Hogben, H. J.; Krzystyniak, M.; Charnock, G. T. P.; Hore, P. J.; Kuprov, I., Spinach - a Software Library for Simulation of Spin Dynamics in Large Spin Systems. *Journal of Magnetic Resonance* **2011**, 208 (2), 179-194.
85. Frisch, M. J.; Trucks, G. W.; Schlegel, H. B.; Scuseria, G. E.; Robb, M. A.; Cheeseman, J. R.; Scalmani, G.; Barone, V.; Mennucci, B.; Petersson, G. A.; Nakatsuji, H.; Caricato, M.; Li, X.; Hratchian, H. P.; Izmaylov, A. F.; Bloino, J.; Zheng, G.; Sonnenberg, J. L.; Hada, M.; Ehara, M.; Toyota, K.; Fukuda, R.; Hasegawa, J.; Ishida, M.; Nakajima, T.; Honda, Y.; Kitao, O.; Nakai, H.; Vreven, T.; Montgomery, J. A.; Peralta, J. E.; Ogliaro, F.; Bearpark, M.; Heyd, J. J.; Brothers, E.; Kudin, K. N.; Staroverov, V. N.; Kobayashi, R.; Normand, J.; Raghavachari, K.; Rendell, A.; Burant, J. C.; Iyengar, S. S.; Tomasi, J.; Cossi, M.; Rega, N.; Millam, J. M.; Klene, M.; Knox, J. E.; Cross, J. B.; Bakken, V.; Adamo, C.; Jaramillo, J.; Gomperts, R.; Stratmann, R. E.; Yazyev, O.; Austin, A. J.; Cammi, R.; Pomelli, C.; Ochterski, J. W.; Martin, R. L.; Morokuma, K.; Zakrzewski, V. G.; Voth, G. A.; Salvador, P.; Dannenberg, J. J.; Dapprich, S.; Daniels, A. D.; Farkas; Foresman, J. B.; Ortiz, J. V.; Cioslowski, J.; Fox, D. J. *Gaussian 09, Revision A.01*, Wallingford CT, 2009.
86. Parr, R. G., *Density-Functional Theory of Atoms and Molecules*. Clarendon Press; Oxford University Press: Oxford [England]; New York, 1989.
87. Deng, W.; Cheeseman, J. R.; Frisch, M. J., Calculation of Nuclear Spin-Spin Coupling Constants of Molecules with First and Second Row Atoms in Study of Basis Set Dependence. *Journal of Chemical Theory and Computation* **2006**, 2 (4), 1028-1037.
88. Peralta, J. E.; Barone, V.; Contreras, R. H.; Zaccari, D. G.; Snyder, J. P., Through-Bond and through-Space J(Ff) Spin-Spin Coupling in Perdifluoronaphthalenes: Accurate Dft Evaluation of the Four Contributions. *J. Am. Chem. Soc.* **2001**, 123 (37), 9162-9163.
89. Sychrovsky, V.; Grafenstein, J.; Cremer, D., Nuclear Magnetic Resonance Spin-Spin Coupling Constants from Coupled Perturbed Density Functional Theory. *J. Chem. Phys.* **2000**, 113 (9), 3530-3547.
90. Becke, A. D., Density-Functional Thermochemistry .3. The Role of Exact Exchange. *J. Chem. Phys.* **1993**, 98 (7), 5648-5652.
91. Jones, J. A., Quantum Computing with Nmr. *Progress in nuclear magnetic resonance spectroscopy* **2011**, 59 (2), 91-120.
92. Khaneja, N.; Reiss, T.; Kehlet, C.; Schulte-Herbruggen, T.; Glaser, S. J., Optimal Control of Coupled Spin Dynamics: Design of Nmr Pulse Sequences by Gradient Ascent Algorithms. *Journal of magnetic resonance* **2005**, 172 (2), 296-305.

93. Skinner, T. E.; Kobzar, K.; Luy, B.; Bendall, M. R.; Bermel, W.; Khaneja, N.; Glaser, S. J., Optimal Control Design of Constant Amplitude Phase-Modulated Pulses: Application to Calibration-Free Broadband Excitation. *Journal of magnetic resonance* **2006**, *179* (2), 241-9.
94. Beharry, A. A.; Woolley, G. A., Azobenzene Photoswitches for Biomolecules. *Chem. Soc. Rev.* **2011**, *40* (8), 4422-4437.
95. Fortin, D. L.; Banghart, M. R.; Dunn, T. W.; Borges, K.; Wagenaar, D. A.; Gaudry, Q.; Karakossian, M. H.; Otis, T. S.; Kristan, W. B.; Trauner, D.; Kramer, R. H., Photochemical Control of Endogenous Ion Channels and Cellular Excitability. *Nature Methods* **2008**, *5* (4), 331-338.
96. Garcia-Amoros, J.; Diaz-Lobo, M.; Nonell, S.; Velasco, D., Fastest Thermal Isomerization of an Azobenzene for Nanosecond Photoswitching Applications under Physiological Conditions. *Angew. Chem.-Int. Edit.* **2012**, *51* (51), 12820-12823.
97. Mourot, A.; Fehrentz, T.; Le Feuvre, Y.; Smith, C. M.; Herold, C.; Dalkara, D.; Nagy, F.; Trauner, D.; Kramer, R. H., Rapid Optical Control of Nociception with an Ion-Channel Photoswitch. *Nature Methods* **2012**, *9* (4), 396-U114.
98. Velema, W. A.; van der Berg, J. P.; Hansen, M. J.; Szymanski, W.; Driessen, A. J.; Feringa, B. L., Optical Control of Antibacterial Activity. *Nature chemistry* **2013**, *5* (11), 924-8.
99. Yue, L.; Pawlowski, M.; Dellal, S. S.; Xie, A.; Feng, F.; Otis, T. S.; Bruzik, K. S.; Qian, H. H.; Pepperberg, D. R., Robust Photoregulation of Gaba(a) Receptors by Allosteric Modulation with a Propofol Analogue. *Nat. Commun.* **2012**, *3*.
100. Clatworthy, M. R.; Kettunen, M. I.; Hu, D.-E.; Mathews, R. J.; Witney, T. H.; Kennedy, B. W. C.; Bohndiek, S. E.; Gallagher, F. A.; Jarvis, L. B.; Smith, K. G. C.; Brindle, K., Magnetic Resonance Imaging with Hyperpolarized Fumarate Allows Detection of Early Renal Acute Tubular Necrosis. *Proceedings of the National Academy of Sciences of the United States of America* **2012**, *109* (33), 13374-13379.
101. Mignion, L.; Dutta, P.; Martinez, G. V.; Foroutan, P.; Gillies, R. J.; Jordan, B. F., Monitoring Chemotherapeutic Response by Hyperpolarized ¹³C-Fumarate MRS and Diffusion MRI. *Cancer Res* **2014**, *74* (3), 686-94.
102. Lee, C. J.; Liang, X.; Chen, X.; Zeng, D.; Joo, S. H.; Chung, H. S.; Barb, A. W.; Swanson, S. M.; Nicholas, R. A.; Li, Y.; Toone, E. J.; Raetz, C. R.; Zhou, P., Species-

Specific and Inhibitor-Dependent Conformations of Lpxc: Implications for Antibiotic Design. *Chem Biol* **2011**, *18* (1), 38-47.

103. Liang, X.; Lee, C. J.; Chen, X.; Chung, H. S.; Zeng, D.; Raetz, C. R.; Li, Y.; Zhou, P.; Toone, E. J., Syntheses, Structures and Antibiotic Activities of Lpxc Inhibitors Based on the Diacetylene Scaffold. *Bioorg Med Chem* **2011**, *19* (2), 852-60.

104. Christiansen, E.; Due-Hansen, M. E.; Urban, C.; Grundmann, M.; Schmidt, J.; Hansen, S. V.; Hudson, B. D.; Zaibi, M.; Markussen, S. B.; Hagesaether, E.; Milligan, G.; Cawthorne, M. A.; Kostenis, E.; Kassack, M. U.; Ulven, T., Discovery of a Potent and Selective Free Fatty Acid Receptor 1 Agonist with Low Lipophilicity and High Oral Bioavailability. *Journal of medicinal chemistry* **2013**, *56* (3), 982-92.

105. Dubinsky, L.; Krom, B. P.; Meijler, M. M., Diazirine Based Photoaffinity Labeling. *Bioorg. Med. Chem.* **2012**, *20* (2), 554-570.

106. Hashimoto, M.; Hatanaka, Y., Recent Progress in Diazirine-Based Photoaffinity Labeling. *European Journal of Organic Chemistry* **2008**, (15), 2513-2523.

107. Claytor, K.; Theis, T.; Feng, Y.; Warren, W., Measuring Long-Lived ^{13}C State Lifetimes at Natural Abundance. *Journal of Magnetic Resonance* **2014**, *239* (0), 81-86.

Biography

Yesu Feng was born in March, 1986, in Chengdu, China. He graduated with a B.S. (July, 2008) from the department of chemistry at University of Science and Technology of China (USTC) in Hefei, China. He then came to the US and finished a Ph.D thesis (July, 2014) in the department of chemistry at Duke University in North Carolina. Between June and October, 2012, Yesu finished an intern study at Schlumberger-Doll-Research center in Cambridge, Massachusetts where he focused on characterization of oil-shale bitumen using ^{13}C NMR techniques. During his Ph.D career, Yesu received multiple awards from the department and various conferences such as the Kathleen Zielek Fellowship and Isotec student sponsorship by Aldrich Chemistry to the ISMAR conference. He received the Chinese Government Award for Outstanding Self-financed Students Abroad in April, 2013 and was selected as one of the three recipients for the Ernst-Awards in September, 2013. Below are a list of publication he had during his Ph.D career and a list of oral and poster presentation he gave in conferences.

Publications:

Feng, Y., Thies, T., Wu, T., Claytor, K.E. and Warren, W.S.; "Long-lived polarization protected by symmetry", J. Chem. Phys., 2014, submitted.

Feng, Y., Le Doan, T.V. and Pomerantz, A.; "The chemical composition of bitumen in pyrolyzed oil shale: characterization by ^{13}C NMR spectroscopy", Energy & Fuels, 2013, 27, 7314-7323

Feng, Y., Theis, T., Liang, X., Wang, Q., Zhou, P. and Warren, W.S.; "Storage of hydrogen spin polarization in long-lived $^{13}\text{C}_2$ singlet order and implications for hyperpolarized magnetic resonance imaging", *J. Am. Chem. Soc.*, 2013, 135(26), 9632-9635

Feng, Y., Davis, R.M. and Warren, W.S.; "Accessing long-lived nuclear singlet states between chemically equivalent spins without breaking symmetry", *Nature Physics*, 2012, 8(11), 831-837

Theis, T., **Feng, Y. (cofirst author)**, Wu, T., Warren, W.S.; "Composite and shaped pulses for efficient and robust pumping of disconnected eigenstates in magnetic resonance", *J. Chem. Phys.*, 2014, 140, 014201

Claytor, K.E., Theis, T., **Feng, Y.**, Gooden, D. and Warren, W.S.; "Accessing long-lived disconnected eigenstates through spins $> \frac{1}{2}$ ", *J. Am. Chem. Soc.*, 2014, submitted.

Claytor, K.E., Theis, T., **Feng, Y.**, and Warren, W.S.; "Measuring long-lived ^{13}C -singlet lifetimes at natural abundance", *J. Magn. Reson.*, 2014, 239, 81-86

Stokes, A.M., **Feng, Y.**, Mitropoulos, T. and Warren, W.S.; "Enhanced refocusing of fat signal using optimized multipulse echo sequences", *Magn. Reson. Med.*, 2012, 69(4), 1044-1055

Presentations:

Feng, Y., Theis, T., Claytor, K.; "Extending $1\text{H}/^{13}\text{C}$ signal lifetime through $^{13}\text{C}_2$ -singlet state between chemically equivalent spins", Presentation at the 35th FGMR Discussion Meeting, Frauenwörth, Germany, Sept 2013.

Feng, Y., Theis, T., Claytor, K.; "Extending $1\text{H}/^{13}\text{C}$ signal lifetime through $^{13}\text{C}_2$ -singlet state between chemically equivalent spins", Presentation at the 18th ISMAR, Rio de Janeiro, RJ, Brazil, May 2013.

Feng, Y., Warren, W.S.; "Extending the lifetime of hyperpolarized magnetization through isolated singlet states". Presentation at the 52nd annual ENC, Asilomar Conference Center, Pacific Grove, CA, April 2011.

Theis, T., **Feng, Y.**, Davis, R.M., Claytor, K., Warren, W.S.; "Long-lived singlet states for hyperpolarization MRI", Presentation at the 54th annual ENC, Asilomar Conference Center, Pacific Grove, CA, April 2013.

Claytor, K., Theis, T., **Feng, Y.**, Warren, W.S.; "Detecting doubly labeled singlet states with natural abundance samples", Poster session presented at the 54th annual ENC, Asilomar Conference Center, Pacific Grove, CA, April 2013.

Feng, Y., Warren, W.S.; "Experimental Demonstration of Long-lived Singlet States between Chemically Equivalent Spins", Poster session presented at the 53rd annual ENC, Intercontinental Hotel, Miami, FL, April 2012.

Feng, Y., Warren, W.S.; "Extending the Lifetime of Hyperpolarized Magnetization through Isolated Singlet States", Poster session presented at the 52nd annual ENC, Asilomar Conference Center, Pacific Grove, CA, April 2011.

Stokes, A., Mitropoulos, T., **Feng, Y.**, Branca, R.T., Warren, W.S.; "Optimization of interpulse delays in multi-pulse echo sequences to enhance refocusing of fat", Poster session presented at the 52nd annual ENC, Asilomar Conference Center, Pacific Grove, CA, April 2011.

Stokes, A.M., **Feng, Y.**, Jenista, E., Branca, R.T., Warren, W.S.; "Unequal echo spacing improves MRI signals and multiple quantum images", Poster session presented at the 51st annual ENC, Daytona Beach, Florida, April 2010.